GAUGE AND TENSION CONTROL DURING THE ACCELERATION PHASE OF A STECKEL HOT ROLLING MILL

by

Burkhard Heinrich Freyer

Submitted in partial fulfillment of the requirements for the degree
Master of Engineering (Electronic Engineering)
in the
Faculty of Engineering, Built Environment
and Information Technology

UNIVERSITY OF PRETORIA

November 2002

Abstract

Low investment cost and flexibility regarding its products make the Steckel mill an attractive option in steel rolling. A characteristic of this mill is its reversing type of operation, which is its main difference from multi stand mills. A Steckel hot strip rolling mill is considered for controller design purposes in this dissertation.

A nonlinear simulator of this process, modeled in [4], is used for the identification of linear models with a point of linearization during the acceleration phase of the mill. The linear models are identified for different cases simulated with and without gauge meter compensation and controlled tensions as part of the simulator. The system identification is accompanied by a heuristic justification of the data obtained.

A diagonal PID/PI controller as well as diagonal and MIMO H_∞ controllers, based on the linear models, are designed and implemented on the simulator.

From the system identification data for the different linear models it could be seen that gauge meter compensation successfully counteracts the adverse effect of mill stretch and eliminates an oscillatory influence of the tensions on the exit gauge of the strip. The results from simulations of the different controllers in closed loop with the nonlinear plant showed, that the requirements, specified for the controllers, are fulfilled by a diagonal controller and an H_∞ controller scheme designed for a linear model with nonzero transfer functions only on the diagonal. The latter H_∞ controller scheme, which includes gauge meter compensation and an inner loop tension control in the simulator is, among three controller schemes tested, found to be most suited.

Keywords

Steel making, hot strip rolling, Steckel rolling mill, system identification, acceleration phase, tensions, exit gauge, diagonal control, H-infinity control, gauge meter compensation

Opsomming

Lae bestedingskoste en buigbaarheid t.o.v. sy produkte maak die Steckel wals 'n aantreklike opsie onder staalwalsprosesse. 'n Kenmerk van hierdie wals is sy omkeer tipe bedryf, wat die hoof verskil is in vergelyking met walse met meervoudige raamwerke. 'n Steckel warm band wals proses word in hierdie verhandeling beskou met die oog op beheerderontwerp.

'n Nie-lineêre simulator van hierdie proses, soos in [4] gemodelleer, word gebruik vir die identifisering van lineêre modelle met 'n punt van linearisering gedurende die versnellingsfase van die wals. Die lineêre modelle is geïdentifiseer vir verskillende gesimuleerde gevalle, met en sonder diktemeter-kompensering en beheerde bandspannings. Die stelsel-identifikasie word vergesel deur 'n heuristiese motivering van die data wat verkry is.

'n Diagonale PID/PI beheerder sowel as 'n diagonale en 'n MIMO H_∞-beheerder, gebaseer op die lineêre modelle, word ontwerp en op die simulator geïmplementeer.

In die stelsel-identifikasie data kan gesien word dat diktemeter-kompensering die nadelige uitwerking van walsrekking suksesvol teëwerk en die ossillerende invloed van die bandspannings op die uitsetdikte elimineer. Die geslote-lus simulasieresultate met die nie-lineêre gesimuleerde aanleg het gewys, dat 'n diagonale beheerder en 'n H_∞-beheerder, wat ontwerp is vir 'n lineêre model met nie-nul oordragsfunksies slegs op die diagonal, aan die spesifikasies voldoen. Laasgenoemde H_∞-beheerder is onder die drie beheerstelsels, wat getoets is, die meeste geskik.

Sleutelwoorde

staal vervaardiging, warm band wals, Steckel wals, stelsel-identifisering, versnellingsfase, spannings, uitsetdikte, diagonale beheer, H-oneindig-beheer , diktemeter-kompensering

Acknowledgements

During the work on this dissertation Prof. Ian Craig guided me with constructive criticism and positiveness, which helped to focus on the project's essential aspects. I experienced our discussions as stimulating and thank him for this.

The time Prof. Chris Pistorius sacrificed to think through the rolling process and his helpful comments are highly valued. Communication with him was always fruitful.

A significant portion of my thanks I want to express towards Ernst Scholtz for answering numerous questions I had about the simulator. I appreciated that I could use such a detailed program of his.

In the Department of Electrical, Electronic and Computer Engineering there were people such as Prof. Yavin, Prof. Xia, Fernando Camisani and Leon Staphorst who gave me advice and information, I would not easily have found in literature, for which I want to thank them here.

This work will also remind me of the occasions I was given advice by colleagues, Elsa de Klerk, Kobus Oosthuizen, Rademeyer Vermaak, Pieter de Villiers, Paul Rathaba, Jerry Wang and Jacques Steyn.

Many of the personnel of this University, I have asked to help in one or other way, were always prepared to respond positively for which I am so grateful.

My father, brothers and sister supported me everyone in their own personal way during my studies. I am very thankful for this.

In particular I want to thank all friends and people here and in Windhoek that encouraged me and were interested in my work.

CONTENTS

CHAPTER 1

INTRODUCTION

Together with forging, casting, drawing and other processes rolling classifies under primary conventional manufacturing processes. Unlike machining it is a process used to change the shape of material using plastic deformation. This is accomplished by passing the material to be rolled between rollers revolving at the same speed but in opposite directions. Deformation then occurs as a result of compression of the material in the roll gap between the rollers. This compression is caused by actuators, forcing the rollers above and below the roll gap towards each other.

1.1 Background

After 1949 the first generation of Steckel mills were built mainly for industrial countries to roll carbon steel in smaller works where the high investment cost for a mill with continuous finishing train would not have been appropriate, because of the limited demand of the market [1].

At the end of the 1960s some developing countries were equipped with Steckel mills. These mills were designed for a large product mix. For a long period the field of Steckel mill building showed no significant activity until the 1980s when several Steckel mills of the second generation were built. Technological and design improvements made them different from the earlier mills.

Modern Steckel mills can be grouped into two main categories. A production capacity of 150000 to 450000 t/year of exclusively stainless steel, characterizes one group of mills. High flexibility and low investment cost makes the Steckel mills suitable for these steel grades which can either be austenitic, ferritic or martensitic [1]. For the second group production of a wide product mix, regarding strip sizes and grades is typical. Its production program includes stainless steel as well as carbon steel of a wide variety. Non ferrous metals can also be rolled by Steckel mills [2].

Because variations in rolling force are typical for the Steckel rolling process, appropriate control systems are used to ensure that requirements on thickness and profile of the strip are met. Systems used for this purpose are [2].

- Automatic gage control (AGC) : The purpose of this is to counteract the effects that e.g. temperature drop at the strip head and tail can have.
- Roll alignment control (RAC) : RAC is employed to avoid a loss of tracking of the strip which can be caused by temperature differences across the width of the strip.
- Profile, contour and flatness control : Control of these properties of the strip is achieved through a continuously variable camber (CVC) shifting system of the work rolls in contact with the strip as well as work roll bending.

The drives of hot strip mill automation and modernization are e.g. the need for an improved quality and increased productivity [3] with the quality measured in terms of dimensional accuracy, surface finish, flatness and strip's physical properties [4]. Automation projects of modern Steckel hot rolling mills focus on [1].

- material tracking,
- automatic slab and coil storage control,
- re-heating furnace control,
- automatic control of the rolling process with mill sequence control, mill set-up and correction, pass schedule calculation and optimization, automatic crop shear control, automatic gauge control, automatic crown and shape control, finishing temperature control and
- data logging.

Attention will be given to the control of strip thickness and tension in this work using the model of Scholtz [4] of the Steckel hot rolling mill process. Establishing controllers for industrial processes typically have the identification of opportunities and modeling of the process as an initial stage followed by the design of a control system. The general control problem is to obtain a mathematical model from the real plant in the real world, to design a controller in the mathematical world and to finally implement the designed controller in the real world [39]. Within this framework the focus of this dissertation is on the design of the controller, which takes place in the mathematical world.

1.2 Motivation

Rolling mills represent large assets in the steel making industry, which generate significant income. They are therefore of interest when it comes to upgrading. In particular this is the case for Steckel mills considered in this work. As mentioned in section 1.1 the main motivating factors for upgrading are to improve strip quality and increase mill throughput, as profitability is a function of both these factors [6].

Quality can be improved by maintaining a strip thickness control within narrower tolerances. Throughput can be increased by an improvement of tension control. This is so because larger reductions are possible with the application of an increased tension [7], which will be explained in more detail in chapter two.

Although in [5] it is reported that the Steckel mill makes use of tension rather than rolling to reduce the strip thickness, tension just aids the reduction of the strip thickness in the Steckel hot rolling process [4].

The literature often deals with thickness control, but for multi stand rolling mills [8][9]. Tension control for these types of mills is accomplished by loopers as actuators. Not much literature on tension control in Steckel hot rolling mills exists. In many of the literature sources [10][11][12] on rolling mills it is reported on control of the mill output at threading speed. However in [13] the speed up and slow down phases now also become relevant in order to reduce the amount of off-spec product which may be the result of insufficient control during these phases.

With respect to control research on rolling mills the current trend is towards the application of multi-input-multi-output (MIMO) control [8]. Although rolling mills are very complex multivariable systems, the most commonly implemented control systems are multi-loop controllers. The main reason for this is the simple and separate commissioning of the individual controllers. Taking the interaction between the strip thickness and tension into account these controllers are however not ideal. Multivariable control structures are better suited for the group of processes into which the rolling process falls. Several reasons can be quoted to motivate the investigation into a modern advanced MIMO control structure [14].

i) The nonlinearities associated with the actuators need to be considered with the development of a control system for this process.

ii) In general the rolling process is time variant because of thermal and mechanical changes due to wear on the rollers. In addition the dead times in this process vary during the speed up and slow down phases.

iii) A controller is needed which accounts for uncertainties attached to the numerous parameters used to model the process.

iv) Assumptions made to simplify the otherwise complex process, need to be considered in an advanced MIMO controller.

v) Handling of dominant dead times between the stands and thickness sensors make the application of classic controllers difficult.

Above mentioned points can be considered in long term research but are not accounted for in this work. As an initial step in controller design the method used for the control of the Steckel hot rolling process, as investigated in this work, is multi-loop control and H_∞ control. Further research can however be launched with the model developed in [4] as basis.

1.3 Aims and Contributions

Using the model in [4], not only for the identification of a linear time invariant (LTI) model, but also for the design of a multivariable controller, provides more insight into the

process itself. In addition to this the extension of the existing simulator with a control structure is seen as a contribution to knowledge in this field. In particular this work contributes the following.

- In this work controller designs are performed for a reversing mill for an operating point on the speed up ramp, which is different from research found by the author in literature in the field of hot rolling mills.
- Identification of LTI models and investigation of their suitability for controller design purposes.
- An investigation of controlling the plant in which the tensions are already controlled and which has gauge meter compensation incorporated in it.
- Design of a diagonal controller as well as H_∞ controllers for the identified LTI plants.
- A procedure representing an H_∞ controller has been incorporated in the existing simulator in a C++ environment.
- Simulations of the Steckel rolling process for diagonal as well as H_∞ controllers by means of which an evaluation of the controller schemes is possible.

In brief the aims and contributions of this dissertation are diagonal and H_∞ controller design work and application to a non linear simulator which was developed by [4] as a basis for a larger project in which potential benefits of a modern advanced control method to a Steckel hot rolling process are being investigated. This work is thus a continuation of the project in which a rolling process was modeled for control.

1.4 Organization

The process, which becomes the object for controller design in this dissertation, is first described in the following chapter. The description includes a brief overview of where the Steckel type mill fits into the hot rolling process. In succession a closer look will be taken at the Steckel mill itself and in particular the roll gap physics.

In chapter 3 linear models are then identified from step test data produced with the nonlinear simulator. The data will be presented in the form of graphs accompanied by a heuristic justification for the transfer functions of the linear models.

CHAPTER 2

PROCESS DESCRIPTION

2.1 Introduction

The general production route for steel consists of three stages of processing. They are iron making, steel making and making of rolled products [16]. Iron making can be grouped into two main routes, namely the blast furnace route to produce pig iron and the direct reduction route to produce direct reduced iron (DRI). In steel making there are again two routes. They are the basic oxygen furnace route and the electric arc furnace route to produce steel from pig iron, DRI or scrap. In secondary steel making additions are then made to the steel before slabs, billets and blooms are produced from it during continuous casting. This chapter covers a discussion of modeling variables and an outline of the modeling theory, which is given in order to show how some variables are related to the process. In addition the structure of the simulator, reported on in [4], is discussed and an overview of control in rolling mills is given. First however, a description of the hot rolling process follows with the focus on the finishing mill, the Steckel mill.

2.2 Hot Rolling Process Flow

The hot rolling process flow is illustrated in Fig. 2.1. Each step in this process is described below [4].

- Slab reheat furnace: For slabs coming from continuous casting this is the first stage in the hot rolling process. In this furnace the slabs are reheated and kept at a temperature of between approximately 1100 to 1250 °C. When proceeding to the rougher the slabs leave the furnace at a preset temperature calculated by the setup program. The value of the measured temperature is then used to calculate the settings of the rougher.
- Primary descaler: This stage starts with descaling the slabs by means of high pressure water jets. Without descaling surface defects can be caused in the roughing mill when scale is rolled into the slabs' surface.
- Secondary descaler 1: The function of the secondary descaler is to remove secondary scale and improve the smoothness of the slab surface before it is rolled in the rougher.
- Vertical edger: The edger reduces the slab in width to prevent excessive material spread through plastic deformation such that it leaves this stage with a dog-bone shape cross section [15].
- Horizontal roughing mill: The roughing mill consists of a vertical edger forming an assembly with the reversing horizontal stand [1]. Its purpose is to reduce the slab to an intermediate thickness of 22 to 32 mm.

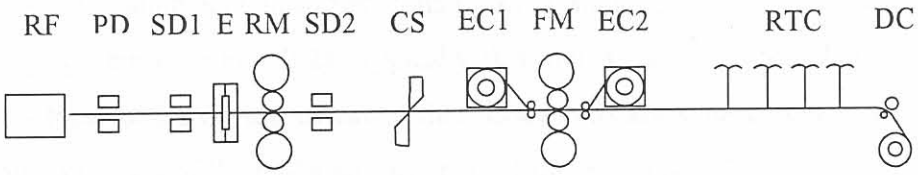

RF	Reheat furnace	CS	Crop shear
PD	Primary descaler	EC1	Entry coiler
SD1	Secondary descaler 1	FM	Finishing mill
E	Edger	EC2	Exit coiler
RM	Roughing mill	RTC	Run out table cooling
SD2	Secondary descaler 2	DC	Down coiler

Figure 2.1: Hot rolling process

- Secondary hydraulic descaler 2: Secondary descaling can be used after roughing before the plate enters the final rolling. Secondary descaling is also done with high pressure water jets.

- Crop shear: Head and tail ends can have defects caused during roughing. In order to have them removed before the plate enters the finishing, the ends are cropped.
- Entry coiler: The entry coiler is situated in a furnace to maintain the temperature level needed during rolling. It is part of the finishing mill. After every pass the entry coiler changes to exit coiler and vice versa.
- Finishing mill: This is where the Steckel mill is used to reduce the strip to its desired thickness in a reversing action whilst maintaining the strip profile and shape.
- Exit coiler: The description for the entry coiler also applies to the exit coiler.
- Run-out table cooling: As soon as the strip is at its specified gauge, it is cooled such that the materials micro structure is fixed and therefore also its mechanical properties.
- Down coiler: After completion of all steps in the rolling process the strip is coiled ready for packaging or for secondary manufacturing processes.

2.3 The Steckel Finishing Mill

2.3.1 Design

The Steckel finishing mill basically consists of a stand carrying rollers and a hydraulic positioning system (see Fig. 2.2). Typically this mill is built as a four high type, meaning that it has four rollers on top of each other. Load cells are situated below the rollers. The coilers on both sides of the mill also form part of the finishing mill.

The model from [4], utilized in this work, is based on the model derived in [17] in so far as it is described as a system consisting of continuous mass elastic beams held in position by discrete elements (see Fig.2.3). Bearings and roll chocks have been lumped and termed as discrete elements. They are approximated by discrete lumped masses and springs indicated as Ms and Ks respectively in Fig. 2.3. In the model, work rolls and back up rolls have been described as continuous mass beams subjected to elastic bending. Bending of the work rolls is diminished by the use of back up rolls. The top and bottom back up roll bearings are supported by means of hydraulic actuators and load cells respectively. The rolling force is transmitted through the roll necks to the actuators at the top and load cells at the bottom of the mill and is absorbed by the mill frame as elastic stretch. Hydraulic jacks are

mounted between the bearings of the top and bottom work rolls on the drive, and on the operator side of the mill indicated as springs K_{JL} and K_{JR} in Fig.2.3. Their function is to counteract bending moments on the work rolls caused by the separating force of the strip. It is the function of the hydraulic actuators to move the backup rolls such that the roll gap is kept constant.

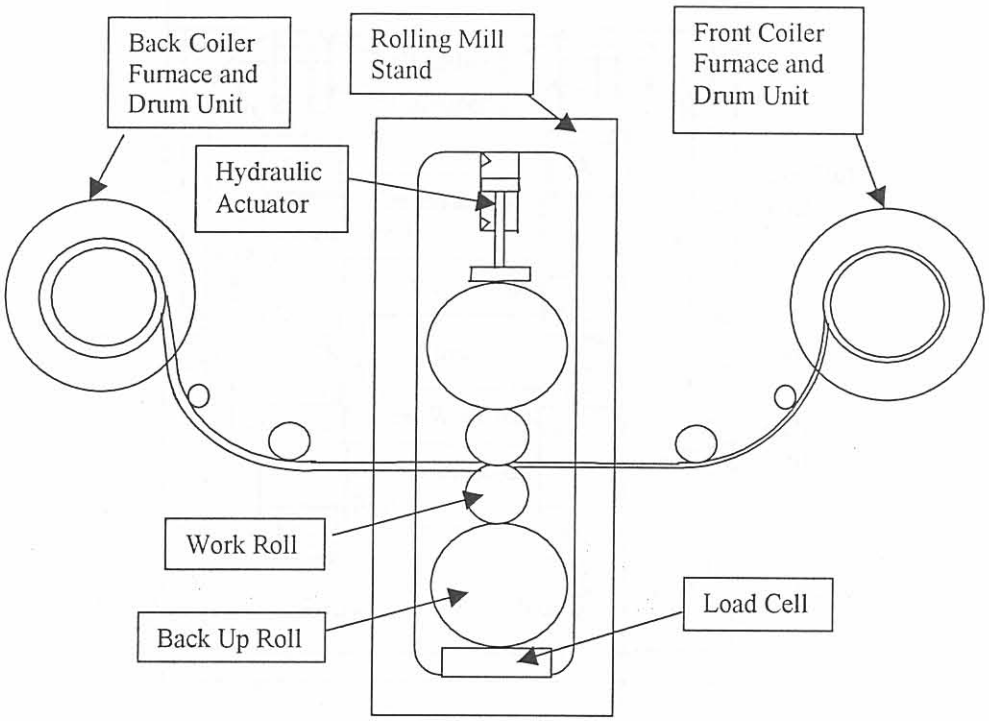

Figure 2.2: Side view of a Steckel hot rolling mill.

2.3.2 Principle of Steckel Hot Rolling

After the strip has been cropped ahead of the Steckel mill, the strip head end is passed underneath the entrance coiler furnace and threaded into the roll gap by the entry side pinch roll unit. After the first pass the strip is fed to the delivery side coiling mandrel and as soon as the first wraps have been coiled and the strip tension has assumed its setup value, the coiler accelerates together with the mill [2]. A constant strip tension is maintained during a pass. When the tail end of the strip enters the roll gap, the mill is slowed down such that the tail end stops before the pinch roll unit on the current delivery side of the mill. The roll gap is then preset for the next pass and the process is reversed

such that the entry side pinch roll unit now feeds the entry side coiling mandrel. The nature of this reversing process is such that the ends of the strip are exposed to greater cooling because the process involves braking, feed into the roll gap and threading in. Therefore the rolling force increases when the strip ends move through the roll gap. This is a characteristic of Steckel hot rolling mills.

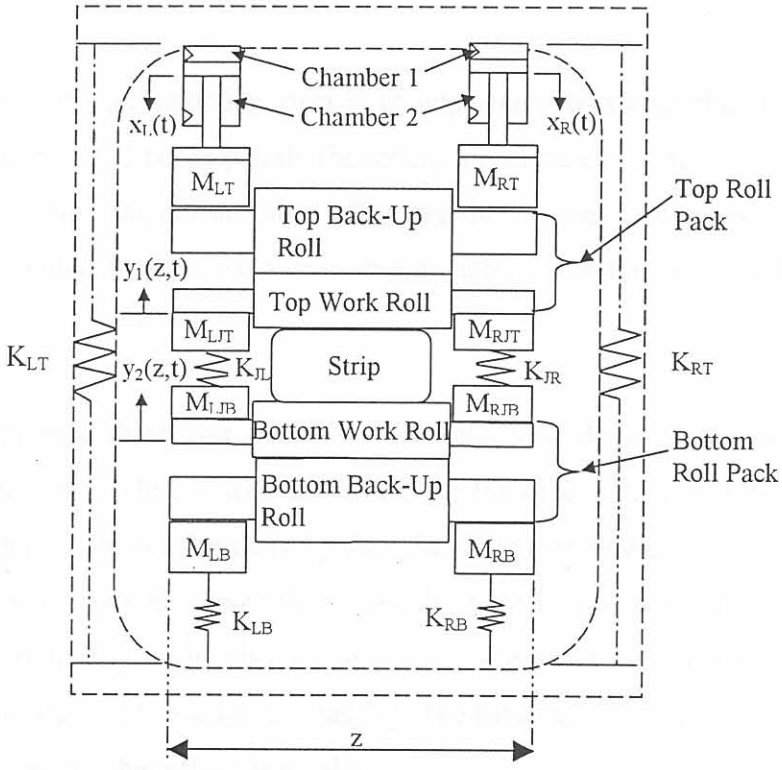

Figure 2.3: Cross sectional view of rolling mill (figure adapted from [4]).

2.3.3 Roll Gap Physics

Across the roll gap the law of mass flow continuity holds [18]. With the assumption that material spread in the width is negligible it can be stated that:

$$v_1 \cdot h_1 = v_2 \cdot h_2 \tag{2.1}$$

where

v_1: strip's entrance velocity into the roll gap,

h_1: strip's entrance thickness into the roll gap,

v_2: strip's exit velocity from the roll gap and

h_2: strip's exit thickness from the roll gap.

In the roll gap metal flows plastically. Because of this plasticity of the material the whole roll gap is filled with strip material. The strip entering the finishing mill has a temperature of more than 1000°C. In the roll gap the entering strip exerts a separating force, the specific roll force P' in [N/m], on the work rolls causing them to bend and the arc of contact to flatten elastically. Due to bending of the rollers the strip leaving the roll gap is slightly thicker along the center. This deviation of strip thickness across its width is termed the crown.

The temperature of the incoming strip is of importance in so far that the material yield stress depends on it and consequently the rolling forces necessary for a certain reduction in thickness. The strip temperature also influences the thermal crown on the working rolls and their differential thermal expansion in turn affects the thickness crown of the strip ([2],[19]).

Slipping in opposite directions occurs at the entry and delivery side along the arc of contact. At the entry side the strip moves slower than the rollers such that it gets drawn into the roll gap while on the delivery side the strip gets braked because the peripheral speed of the work rolls is slower than the exit speed of the strip. This phenomenon of friction forces opposing each other along the arc of contact and increasing in a direction towards the roll gap lead to a friction hill [7]. The location of this friction hill is called the neutral point, a point where there is no slip.

It is possible to shift the position of the neutral point by applying back tension, T_1, which is strip tension between the entry coiler and the stand, and front tension, T_2, which is the tension between the stand and the exit coiler. The application of back tension moves the neutral point towards the roll gap exit while front tension shifts it towards the entrance [7]. It is known that back tension is more effective in shifting the neutral point than front tension [20].

2.4 Variables

2.4.1 Modeling Variables

Variables that are significant in the rolling process and that have been used in the modeling work of Scholtz [4] are mentioned below, the purpose of which is to give a more detailed description of the process. Some variables affect the deformation in the roll gap directly and some indirectly.

Temperature θ: Temperature is an independent process parameter [7] and is regarded as a key variable [10] in the deformation of metal as it influences the yield stress, which is also dependent on strain and strain rate of the material.

Friction coefficient μ : The friction coefficient, which was in [4] computed as a linear function of temperature of the material in the roll gap, affects the force balances in the derivation of Orowan's differential equation [5]. It is by means of this equation that the specific rolling force, P', which was already mentioned in section 2.3.3, is determined.

Vertical pressure p: The vertical pressure distribution along the arc of contact between the strip and the rollers depends on the deformed roll radius and is influenced by the independent variables [7], and front and back tension.

Deformed roll radius R': Part of the geometry of the roll gap is the deformed roll radius. While exerting roll pressure onto the strip the rolls tend to deform which results in an increase in the roll radius in the arc of contact [22]. An interdependency exists between the deformed roll radius R' and the specific rolling force P'.

Rolling velocity v_{roll} : The rolling velocity is an independent process parameter [7] and it influences the strain rate in the roll gap and the front and back tensions of the strip.

Entrance velocity v_1 (see Fig. 2.4): The entrance velocity of the strip into the roll gap is determined by the material flow $h_1 v_1$ entering the roll gap.

Exit velocity v_2 (see Fig. 2.4): The exit velocity of the strip depends on the material flow $h_1 v_1$ as well as on the reduction in thickness, known as draft, $\delta = h_1 - h_2$.

Back coiler peripheral speed v_{bc} (see Fig. 2.5): The back tension T_1 is influenced by the difference between v_1 and v_{bc} via an integral relationship.

Front coiler peripheral speed v_{fc} (see Fig. 2.5): The front tension T_2 is influenced by the difference between v_2 and v_{fc} via an integral relationship.

Draft δ: The draft is used to calculate the bite angle and the horizontal length of the arc of contact and indirectly determines the specific rolling force P'.

Yield stress k: Yield stress is a function of strain rate and temperature of the material. Elastic regions exist before and after plastic regions in the roll gap [23] and can be attributed to the yield stress, which is higher than the local applied stress.

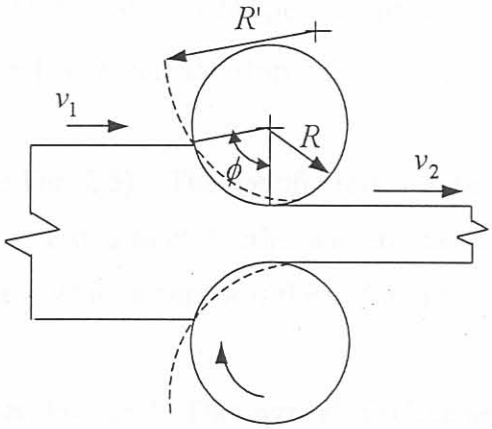

Figure 2.4: Roll gap variables.

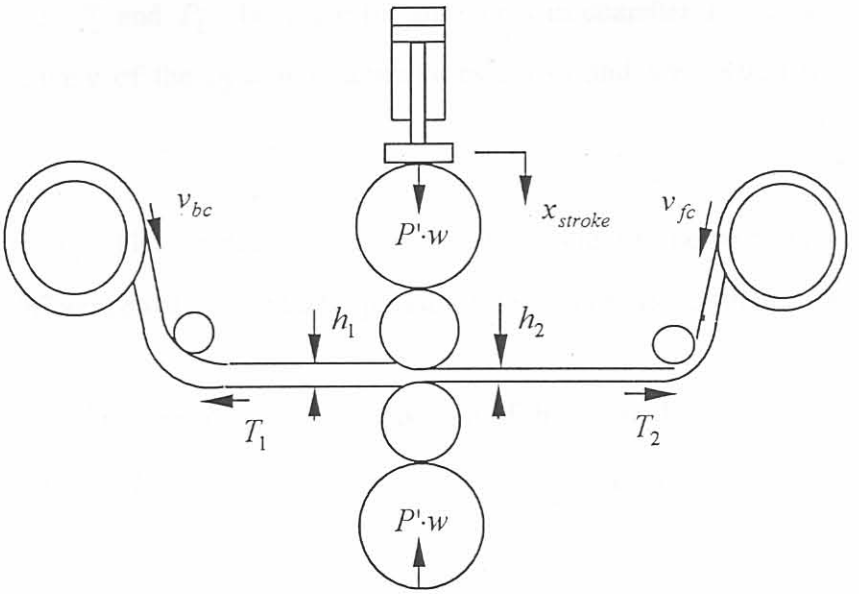

Figure 2.5: Rolling process variables.

Back tension T_1 (see Fig. 2.5): Regarding the deformation process back tension is an independent process parameter [7] braking the material flow into the roll gap.

Front tension T_2 (see Fig. 2.5): It is also an independent process parameter with respect to the deformation in the roll gap [7] causing the strip to be drawn.

Specific rolling force P' (see Fig. 2.5) : The specific rolling force and vertical pressure in the roll gap are proportionally related to each other and are the result of hydraulic actuator stroke. The total rolling force is $P'\cdot w$, where w is the width of the strip.

Vertical displacement y_1 (see Fig. 2.3): The vertical displacement y_1 of the upper roll pack consisting of the upper work and backup roll is determined from a force balance of the seperating force of the strip and the forces exerted by the hydraulic jacks and roll chocks, i.e. the discrete elements in the modeling work in [4], onto the roll pack.

Vertical displacement y_2 (see Fig. 2.3): This is the vertical displacement of the bottom roll pack consisting of the bottom work and back up roll and it is also determined from a

force balance of the seperating force of the strip and the forces exerted by the chocks and hydraulic jacks onto the roll pack.

Cylinder pressures P_1 and P_2: They are the pressures in chamber 1 and chamber 2 (see Fig. 2.3) respectively of the hydraulic actuator cylinders and are related to the specific rolling force P'.

Supply pressure P_s: This pressure is on the supply side of the hydraulic positioning system and its difference with the cylinder pressures determines the cylinder flows.

Tank pressure P_t: This pressure is on the tank side of the hydraulic positioning system and its difference with the cylinder pressures determines the cylinder flows.

2.4.2 State Variables

The state space model of the Steckel hot rolling mill process comprises 18 state variables. The first eight state variables represent the normal time coordinates $q(t)$ of the stand and their derivatives $\dot{q}(t)$. Together with the assumed modes, $\psi(z) = [\psi_1 \quad \psi_2]$, vertical displacement $\hat{y}_i(z,t)$, $i \in [1,2]$, of the roll packs can be expressed as:

$$\hat{y}_i(z,t) = \sum_{j=1}^{2p} \psi_{i_j}(z) q_{i_j}(t) = \psi_i(z) q_i(t) \tag{2.2}$$

with the assumed modes vectors, $\psi_1(z)$ and $\psi_2(z)$, as described in section 2.5.1.

The other 10 state variables describe the state of the hydraulic positioning system by means of hydraulic pressures, hydraulic stroke, servo valve openings and the derivatives of servo valve openings. The part of the model described by these 10 variables forms the nonlinear part of the state space model.

2.5 Simulator

2.5.1 Models

As it became obvious in the previous sections, the rolling process is ruled by different aspects such as the strip tension on both sides of the roll gap, the hydraulic actuators exerting forces on the rollers, the stand which consists of rollers changing their position thereby influencing the roll gap and the material in the roll gap itself. In order to take all these aspects into account in a simulator of the process, four core models were derived in [4]. These models are the roll gap model (RGM), the tension models (TM), the stand model (SM) and the hydraulic actuator model (HA), which together form the simulator. They are described below in terms of their inputs, outputs as well as the theory the models are based on.

Roll gap model: For the RGM the draft, δ, roll speed , v_{roll}, entrance and exit temperatures, θ_1 and θ_2, and entrance and exit tensions, T_1 and T_2, are the inputs while the specific rolling force, P', entrance and exit velocities, v_1 and v_2, and the length of the arc of contact, L_p, are the outputs, i.e. the values calculated from the input values.

P' in [N/m] is computed from the vertical rolling pressure, p in [Pa], which is determined by solving the following ODEs.

$$\frac{dp}{d\phi} = \frac{2R'}{h(\phi)}\left[p(\phi)\left(\frac{\sin\phi \pm \mu\cos\phi}{1 \mp \mu\tan\phi} \right) - p(\phi) - k \right)\sin\phi \Bigg] \tag{2.3}$$

where

ϕ: angle of arc of contact measured from the exit of the roll gap in [rad] (see Fig. 2.4),

h: strip thickness [m].

P' is also a function of R' [24] which in turn depends on P' by the relationship of Hitchcock's formula given as

$$R' = R\left[1 + \frac{16(1-\upsilon^2)P'}{\pi E \delta} \right] \tag{2.4}$$

where

υ: Poisson's ratio for steel and

E: Young's modulus of the work rolls.

The structure of the RGM is an iterative loop with a relaxation step for R' because of this implicit relationship between P' and R'. In this loop R' is updated and the two ODEs in Eq. 2.3 are solved.

Tension model (TM): The TM describes the strip tension behaviour during the rolling process. The inputs of the TM are v_1 and v_2 from the RGM as well as v_{bc} and v_{fc}, the back and front coiler speeds respectively. A change in draft, δ, results in a change in v_1 and v_2 and therefore in tension variations according to

$$T_i = \frac{E_{ss}(h_i w)}{L_{cfrg}} \int_0^t (\pm v_i(\tau) \mp v_c(\tau)) d\tau \tag{2.5}$$

where

$i \in [1,2]$, $v_c|_{i=1} = v_{bc}$, $v_c|_{i=2} = v_{fc}$,

E_{ss}: Young's modulus of strip material,

w: width of the strip,

L_{cfrg}: strip length between coiler furnace and roll gap.

At a given instant T_1 and T_2 are determined iteratively in a loop in which $T_i, i \in [1,2]$ is updated and which contains a relaxation step for T_1 and T_2. As soon as the tension has stabilized in the iteration loop, time is incremented by $\Delta t_{tension}$ and the iteration for T_1 and T_2 in the next time step is repeated. The integrals of Eq. 2.5 are computed in every execution of the iteration loop.

Stand model (SM): Elastic stretch of the mill stand and roll bending are the phenomena that are described by the SM. Its inputs are P' across the width of the strip and the cylinder chamber pressures of the hydraulic actuators ($P_{L1}, P_{L2}, P_{R1}, P_{R2}$ in [Pa]) where L and R denote left and right respectively and 1 and 2 denote the chambers. This model has a draft deviation as output, which is calculated as

$$\delta(z,t) = \delta_{setup} - (\delta h_1(t) - (y_1(z,t) - y_2(z,t))), \tag{2.6}$$

where

$-\frac{w}{2} \le z \le \frac{w}{2}$.

By means of separation of the dependency on the variables t and z with an assumed modes vibration analysis method, a decoupled normal coordinate system was derived in [4] to form the following linear ODE system.

$$\begin{bmatrix} \dot{q} \\ \ddot{q} \end{bmatrix} = \begin{bmatrix} I & 0 \\ -M^{-1}K & -M^{-1}C \end{bmatrix} \begin{bmatrix} q \\ \dot{q} \end{bmatrix} + \begin{bmatrix} 0 \\ M^{-1}U^T B \end{bmatrix} u_{SM} \ , \tag{2.7}$$

where

M : system mass matrix,

K : system stiffness matrix,

C : system damping matrix,

U : modal matrix,

B : input matrix and

u_{SM} : input vector to the SM = $[P_{L1} \quad P_{R1} \quad P_{L2} \quad P_{R2} \quad P']^T$.

B was derived in [4] as

$$B = \begin{bmatrix} -\psi_1^T(-\frac{l_1}{2})A_{L1} & \psi_1^T(-\frac{l_1}{2})A_{L2} & -\psi_1^T(\frac{l_1}{2})A_{R1} & \psi_1^T(\frac{l_1}{2})A_{R2} & \Delta_z\psi_1(z)^T \\ 0 & 0 & 0 & 0 & -\Delta_z\psi_2(z)^T \end{bmatrix}, \tag{2.8}$$

where

l_1 : length of top roll pack,

ψ_1 : assumed modes vector for top roll pack,

ψ_2 : assumed modes vector for bottom roll pack,

A_{si} : cylinder cross sectional areas with $s \in (L,R)$ and $i \in (1,2)$. L and R denote left and right side of the stand and 1 and 2 denote top and bottom roll pack respectively.

Δ_z : length of one of the 51 elements into which a roll pack is divided along its length.

Hydraulic actuator model (HA): The inputs of the HA are the left and right hydraulic stroke set points and the outputs are the left and right hydraulic strokes of the actuators. The HA is integrated into the simulator by the relationship that exists between the hydraulic stroke, the vertical displacement of the upper roll pack and mill stretch. In addition the derivatives of the cylinder pressures are expressed in terms of state variables, namely cylinder pressures and vertical displacement derivatives of the upper roll pack showing how the HA is linked to the SM. The relationships that describe the behaviour of the hydraulic actuators are based on the continuity laws of the fluid flow in them as well as on second order dynamics of the servo valve opening (spool movement).

2.5.2 Simulator Structure

Two dynamic models and a static model constitute the simulator. The two dynamic models are the tension model and the state space model. The latter is formed by the stand and hydraulic actuator models. Since the problem solved by the RGM is an off-line analysis problem [5] with computation of force under static conditions, the RGM, which is based on Orowans roll gap theory, can be regarded as a static model. It is recommended by [4] that the tension model is simulated at a higher sampling rate than the main time advancement of the simulator in order to keep the tension loop stable, i.e. values for tensions that converge have to be found iteratively before the tension values for the next time step of the tension loop can be computed.

Referring to Fig. 2.6, the simulator is started by reading input files. It then calculates the initial conditions. At the very beginning of a simulation the initial conditions are determined from steady state values because the simulation is not started before commencement of rolling, but after the pass has been partially completed. Also, before the main time advancement loop starts, the stroke caused by the cascaded hydraulic actuator controller is calculated for the set up of the initial piston extension. The combined actions of the initial set up of the piston extension and the gauge meter compensator are then determined and taken into account in the state space model.

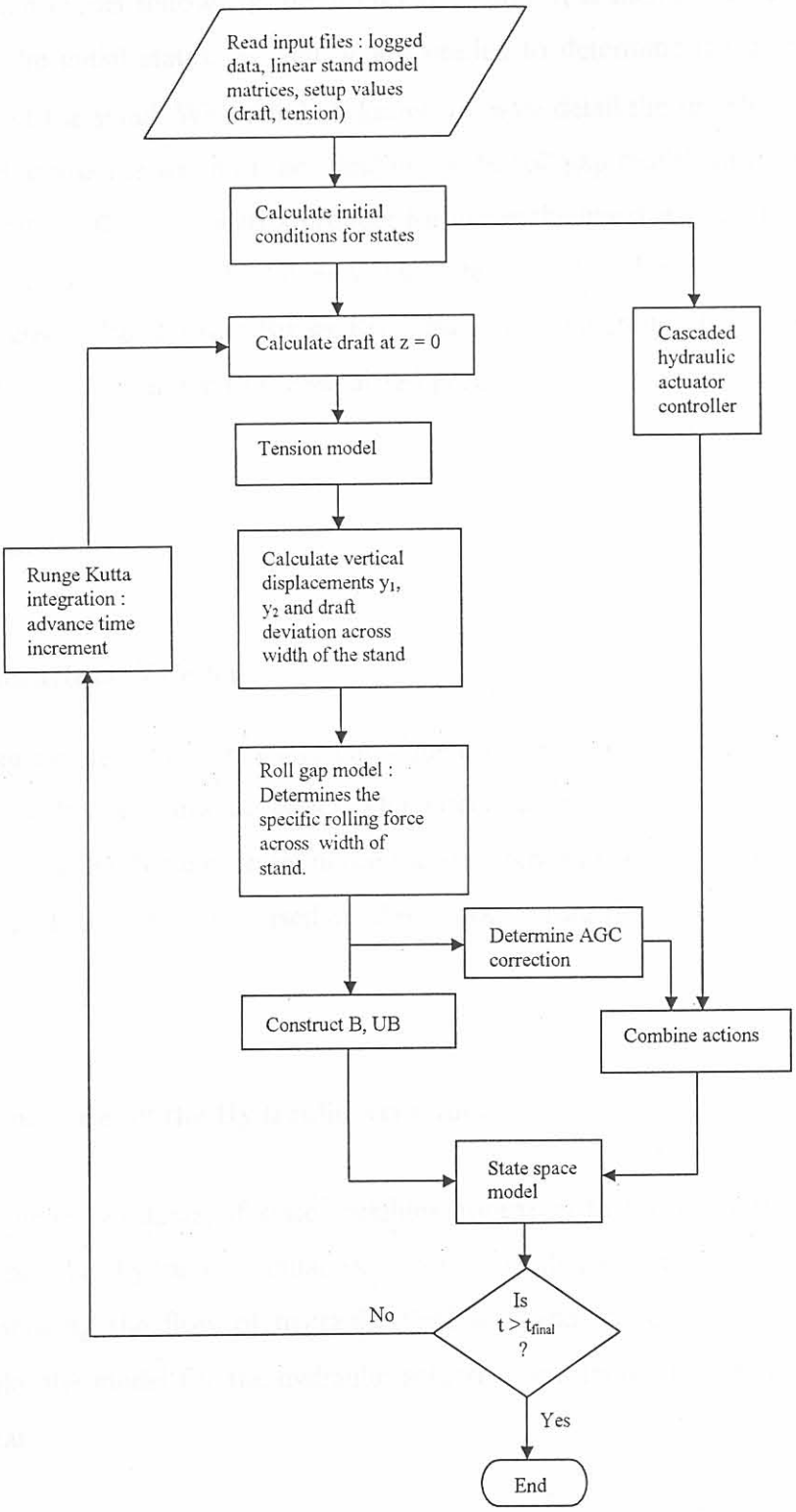

Figure 2.6 : Mill simulator flowchart (figure adapted from [4])

i16539990
01595318X

The main loop of the simulator starts with a calculation of the draft, which is necessary because the draft is an input to the roll gap model, which in turn is a part of the tension model. The tension model follows on the draft calculation. It is then possible to compute y_1 and y_2 from the initial states. y_1 and y_2 are needed to determine the draft deviation across the width of the stand. With the draft known in more detail the specific rolling force can be calculated across the width of the stand using the roll gap model. In the subsequent steps the input matrix, B, and a matrix product for use in the linear part of the state space model are formed (see Fig. 2.6). All new 18 states, i.e. for the next time step, are integrated by means of fourth order Runge Kutta numerical integration from the old states before the next time advancement of the simulated process.

2.5.3 Nonlinearities

2.5.3.1 Nonlinearities of Coilers

Due to the large moment of inertia and consequently very slow response of the coilers their behaviour exhibits a saturation effect. This effect can be expected when a change in coiler speed is demanded for e.g. to influence the strip tensions. Because the coiler inertia does not form part of the model used in this work, saturation in coiler speed is not considered here.

2.5.3.2 Nonlinearities of the Hydraulic Actuators

Terms which contain products of state variables appear in that part of the state space model describing the hydraulic actuators. More specifically these terms appear in expressions describing the flow of hydraulic fluid into and out of the cylinders. These expressions make the model for the hydraulic actuators and therefore the entire model of the mill nonlinear.

2.5.4 Control Systems of Hot Rolling Mills

2.5.4.1 Introduction

Common control systems for hot rolling mills are discussed in this section. The following control system architecture applies - besides other manufacturing processes - also to hot rolling [15].

i) Level 3: Plant wide control. This includes production planning and scheduling.
ii) Level 2: Supervisory control. It includes set-up and control strategy selection.
iii) Level 1: Dynamic control. It is concerned with closed loop control parameters such as exit gauge, strip temperature, profile and shape of the material to be rolled, i.e. it is concerned with the process itself.

The overview of control systems given in the sections to follow will focus on level 1 control.

2.5.4.2 Automatic Gauge Control

As mentioned in the first chapter it is one of the main objectives of hot rolling to maintain a constant thickness for the rolled strip. Disturbances that can prevent this objective from being achieved can be of two different kinds [15].

i) Disturbances arising from the incoming strip, such as gauge or yield strength variations.
ii) Disturbances arising from mill equipment, such as roll eccentricity, roll expansion and roll wear.

The difficulty associated with thickness measurement, which would be necessary for thickness control, is that it cannot be done directly at the location where reduction in thickness takes place. Information about strip thickness can however be derived from load force measurements. The British Iron and Steel Research Association (BISRA)-Davy gauge meter [15] makes use of this principle by which the roll force is manipulated to control the strip exit gauge. It is used on multi stand as well as on Steckel type hot rolling mills.

The relationship between roll force and gauge is linear over a significant range of roll force values. In its linearized form the relationship is.

$$\delta h_2 = -\delta x + \frac{\delta F}{M} \tag{2.9}$$

where M is constant and

δh_2 : strip exit gauge,

δx : hydraulic actuator stroke,

δF : roll force and

M : mill modulus.

The aim is to keep $\delta h_2 = 0$ such that $\delta x = \delta F / M$. A correction in δx can thus be made with exact knowledge of M. Compensation of initial condition errors and drift in the gauge meter thickness estimates is done by means of X-ray gauge measurements on the delivery side of the mill.

The output of the automatic gauge control system, also called gauge meter compensation, is a position reference, which is used by the actuators to position the rolls such that a rolling force is effected. The actuators can either be electrical screw down or hydraulic capsules.

2.5.4.3 Mass Flow and Tension Control

Tension control of Steckel mills will be considered eventually but first a look will be taken at tension control of multi stand rolling mills. However, because the same device, the looper arm, is used for tension control as well as mass flow control, i.e. two control functions, both will be explained briefly.

These two functions of loopers are:

i) They prevent width and thickness changes by means of tension control.

ii) They prevent the formation of strip loops between stands by regulating mass flow.

Strip tension is controlled by torque of the looper motor. Torque is changed by manipulating the motor current. This control is thus indirect. The looper angle is the angle, which the looper arm makes with the horizontal. This angle is an indication of the mass flow. Mass flow is regulated by manipulating the speed of the upstream stand drive motor.

Via the looper both control functions take place close to each other: The looper angle influences the loop length and torque on the looper axis affects the tension. Yet, it is common that tension and loop length (mass flow) are controlled independently.

Mass flow control:

Before and during threading of the strip the set up velocity is the reference velocity. At threading speed it can be trimmed by the mass flow controller, the temperature controller or by zooming. Zooming is the speed increase of the strip in order to minimize temperature losses. The choice of the set up velocities depends on the gauge reduction schedule. If the mass flow has to be increased the looper angle is increased by a speed up of the upstream stand drive motor. Initially this will result in a reduction of the strip tension causing the looper motor to supply more torque. Even if the error in looper angle is zero the looper motor will have its current increased to increase the torque such that the tension reference is achieved.

Tension control:

The problem with tension control in multi stand mills is that no direct measurements of tension are possible and are therefore not available. This makes tension control more complicated. Instead the looper angle is used to calculate the torque required to maintain the tension at the desired reference level. The torque applied at the looper axis is needed not only to oppose the moments caused by strip tension, but also the moments due to the weight of the strip, looper arm and roll as well as the bending of the strip. The sum of these components therefore constitute the reference torque. Each one of these components is a function of the looper angle [15].

The reference torque is the torque needed to regulate the tension at a reference value at the current looper angle. This torque changes in accordance with the looper angle. The reference torque cannot be determined exactly with equations available because of errors in physical assumptions that result in physically wrong equations. Also strip width, gauge and yield stress are not exactly known at each time instant. By means of the current feedback loop the reference torque, which is an input to the looper motor, is maintained. More difficulties in maintaining tension arise during acceleration and deceleration phases of the looper motor. Interaction between looper angle and tension makes independent control of mass flow and tension difficult and multivariable control necessary.

2.5.4.4 Steering Control

Because reversing mills, such as the Steckel mill, are particularly intolerant to camber errors in comparison with tandem mills, steering control is used in Steckel mills. For this control system the measurement system consists of two single-sensor (mono-scopic) Charged Coupled Device (CCD) cameras one each at the mill entry and exit. These two cameras are used in addition to another pair of CCD cameras in a stereo-scopic configuration. The mono-scopic cameras take independent measurements of the strip centerline while the stereo-scopic cameras provide an accurate measurement of the finished width and centerline position [35].

Depending on the strip centerline deviations from the centerline position of the mill a differential roll gap correction is applied. In order to avoid worsening the capability of the mill to maintain constant strip thickness across the width of the strip, the automatic steering system does as little as possible to keep the strip centered.

The conventional method of automatic steering in reversing mills is to apply a differential roll gap correction based on a measured differential load. This method is however only effective if the source of the error is a temperature difference across the width of the strip. The controller will then tend to command a higher force on the side of the strip with the higher resistance to deformation and in doing so ensuring equal elongation over the width of the strip, keeping it straight. When the measured load difference is caused by a wedge profile of the strip unequal elongation will take place, producing a cambered bar.

2.5.4.5 Profile and Flatness Control

The profile and flatness control system present in Steckel mills is used to counteract the influence of progressive wear and thermal crowns on the work rolls as well as changes in roll force due to temperature variations of the strip.

Because changing the profile in thinner strips would also result in flatness errors, profile modifications are done during the first passes while during the last passes it is kept constant to also assure flatness. These demands are met by use of a CVC (Continuously Variable Crown) system in combination with a work roll bending system.

Part of the CVC system are work rolls with S-shaped barrel contours and with the rolls in a diametrically opposite arrangement. The work rolls can be shifted in opposite directions in order to change the crown. Depending on whether a positive or a negative crown is desired the shifting direction is changed accordingly.

Another precondition for a profile and flatness control system is an efficient computer model by means of which preset values for the CVC system and the work roll bending system can be determined based on data for each pass such as strip width, strip thickness and rolling force. Also included in this data would be the desired strip profile.

The function of the automatic profile control (APC) then is to keep the roll gap contour – and thus the strip profile – constant over the length of the strip in the presence of varying rolling forces. Because on Steckel mills extreme differences in rolling force can occur, it happens that the setting range of the work roll bending system is not always sufficient. When it happens that the predetermined bending force is reached the CVC system automatically shifts the rolls, preventing the bending system from reaching its limits [27].

CHAPTER 3

MODEL IDENTIFICATION

3.1 Literature Review

Hearns et al. [8] and Anbe et al. [9] consider the rolling process as multivariable with interaction between strip tensions and thickness and designed an H_∞ controller for the process. [8] and [9] tested their designs on a nonlinear model and a real plant respectively. Their designs were for the threading speed phase of rolling and for a multi stand mill in contrast to this work in which controllers were designed for the speed up phase of a reversing hot rolling mill. In their linear time invariant (LTI) rolling mill model Anbe et al. use tension stress instead of tension as a controlled and state variable. This is an effective way of approaching the control of tension stress because stress is of interest rather than only tension as it is done in this work. However it is also sufficient to use tension as controlled variable because deviations from the setup value of the strip cross section are only very small compared to the total cross section area.

Hearns et al. did their controller design later than Anbe et al. and showed that robust stability in the presence of a changing mill modulus is achievable while still obtaining high performance such as strip thickness accuracy, thereby bypassing the robustness/performance trade-off to an extent.

Pedersen et al. [21] also viewed the hot rolling process as multivariable for controller design purposes. In contrast to [8] and [9] Pedersen et al. investigated plate rolling and the focus mainly was on thickness control by means of a linear quadratic regulator (LQR).

In the projects of [8] and [9] the process variables do not vary across the width of the strip. With regard to this aspect [8] and [9] differ from the work done in [12] and [21]. In [12], however, a Generalised Predictive Controller (GPC) was designed to work on a supervisory level. The control design methodology thus differs from [8], [9] and [21] in so far that a time-varying controller with no fixed structure was designed – it has no fixed structure because an optimization problem is solved at each time step. However similar to the other three projects Grimble et al. [12] did their design for a multivariable multi stand rolling process at threading speed, i.e. steady state. In particular the process variables selected for control in [12] are gauge, profile and temperature.

This shows that the work done in this dissertation most closely resembles that done in [9] but is different from it in the sense that it is done for control of a reversing mill on the speed up ramp.

3.2 Modeling Considerations

The available nonlinear model for the Steckel mill is not in a format that can directly be used for controller design purposes. Therefore an identification of a linear model from the nonlinear simulator was first performed.

For the variable classification of the linear model the outputs of interest are the centerline thickness of the strip and the strip tensions on either side of the roll gap. Hydraulic stroke set points on both sides of the mill frame and back and front coiler peripheral speeds become the choice for the manipulated variables as intervention into the process is possible through these variables. In Laplace transfer function format the LTI model is then

$$\begin{bmatrix} \delta h_2(s) \\ \delta T_1(s) \\ \delta T_2(s) \end{bmatrix} = \begin{bmatrix} g_{11}(s) & g_{12}(s) & g_{13}(s) \\ g_{21}(s) & g_{22}(s) & g_{23}(s) \\ g_{31}(s) & g_{32}(s) & g_{33}(s) \end{bmatrix} \begin{bmatrix} \delta x_{sp}(s) \\ \delta v_{bc}(s) \\ \delta v_{fc}(s) \end{bmatrix}, \tag{3.1}$$

or in standard transfer function model notation,

$$y(s) = G(s)u(s) \tag{3.2}$$

where

$$y(s) = [\delta h_2(s) \quad \delta T_1(s) \quad \delta T_2(s)]^T :$$

the controlled variable vector,

$$u(s) = [\delta x_{sp}(s) \quad \delta v_{bc}(s) \quad \delta v_{fc}(s)]^T :$$

the manipulated variable vector.

A system identification technique (SID) is applied to the simulator of the process in order to get an LTI estimate of the nonlinear model for controller design. As the simulator consists of several sub models of the process (see Fig. 3.1), of which the TM and the RGM are implicitly related to each other, a linearization of the nonlinear model via an algebraic method would possibly not be suitable to reflect such a relationship satisfactorily [24]. The use of the Matlab System Identification toolbox [25] was therefore chosen to obtain the linear model. Fig. 3.1 is derived from the input/output relationships given in Table 3.1.

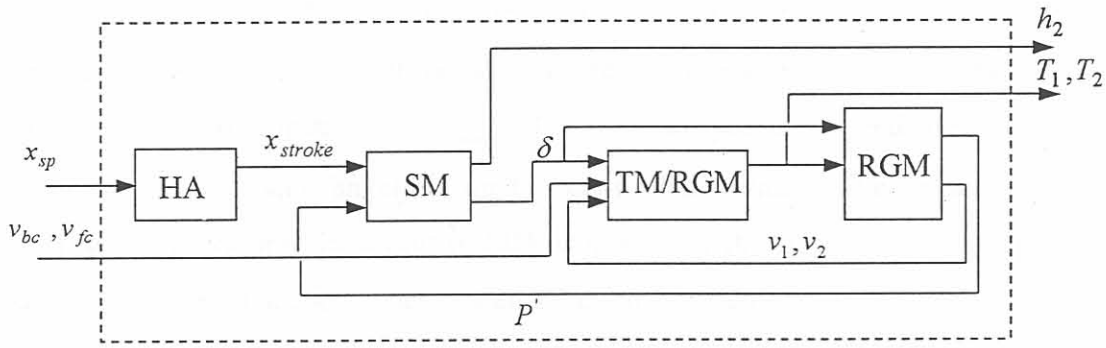

Figure 3.1: Block diagram of rolling process with I/O information.

Table 3.1: Inputs and outputs for process models.

Model	Inputs	Outputs
Hydraulic actuator (HA)	x_{sp}	x_{stroke}
Stand model (SM)	P', x_{stroke}	δ, h_2
Roll gap model (RGM)	δ, T_1, T_2	P', v_1, v_2
Tension model (TM)	v_1, v_2, v_{bc}, v_{fc}	T_1, T_2

With respect to the linear model as in Eq. 3.1 it is suitable to use a least squares method and solve for the best values of parameters of a transfer function that fit the time domain

data. These parameters are the coefficients of difference equation models for the process in which the current output is a function of previous values of the output and present and past values of the input. This is a linear relationship in the time domain, which can easily be converted into Laplace domain transfer function models [26] as desired for Eq. 3.1. By means of the Matlab System Identification toolbox ARX (Auto Regression with external input) linear transfer functions could be identified as elements of the MIMO plant in Eq. 3.1.

In the case of the least squares method any form of inputs can be used to generate data for SID but it was suggested in [4] to use steps with the main reason being the absence of a plant bandwidth, which is necessary to design a PRBS input signal.

In [13] the potential economic benefit for a rolling process of operating the mill optimally on the speed up and slow down phases of rolling was investigated. The results of these findings motivated the decision to choose an operating point and point of linearization during the acceleration phase of the mill. At the point of linearization the main mill drive speed was forced constant at $v_{main} = 3.5$ ms^{-1} to prevent speed deviations during acceleration from having an effect on the controlled outputs. The validity of the LTI model, which is obtained by means of SID, is limited by the size of the coiler speed steps, discussed in the next section. These speed steps can be used as limits because for the speed range of validity only the difference between the coilers peripheral speed and the main drive speed matters, such that the valid speed range is $v_{main} = 3.5 \pm 0.2$ ms^{-1}.

Steps were used as inputs to the simulator and the results used to identify the linear transfer functions between inputs and outputs. Because the reasoning behind the design of step tests in [4] were found to be plausible, the same steps were applied to the simulator in this work. The only difference to [4] lies in the values that were used for the initial states of the upper roll pack. In this work the initial states were given the first nonzero values, which are obtained during the steady state development of the exit gauge, whereas in [4] zero initial states were assumed. The reason for the use of nonzero initial states was to achieve a bumpless start up of the simulations.

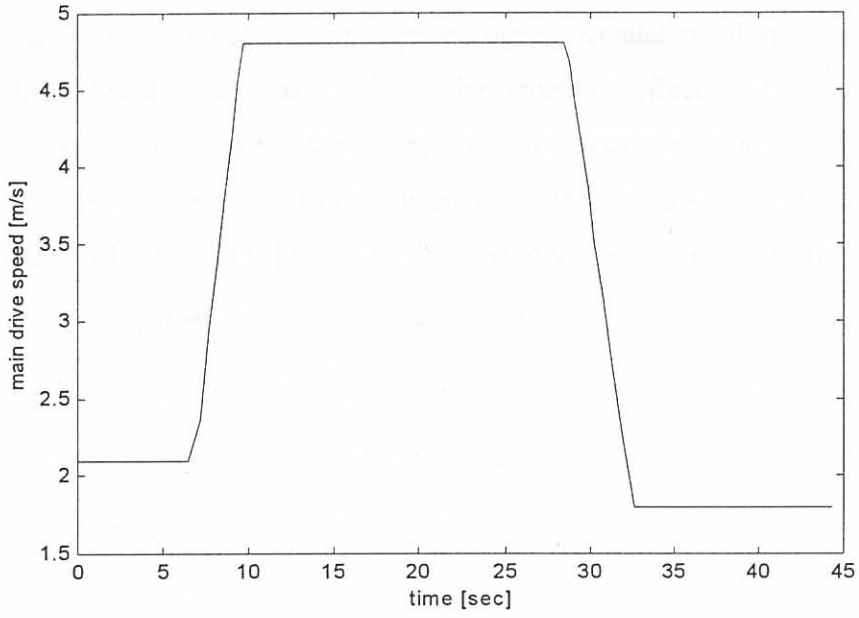

Figure 3.2: Main drive speed during pass 3 of the rolling process.

3.3 Step Tests

The steps are applied to the simulator at the point where the main mill drive speed is forced constant during the speed up phase of the mill.

3.3.1 Hydraulic Stroke Set Points, δx_{sp}

In [4] it is shown that the exit gauge changes even when no inputs are changed. A hydraulic stroke of 1mm was not exceeded in [12] when a supervisory GPC (Generalized Predictive Control)- controller was used to regulate the rolling process. Based on this information the same size of a step was suggested by [4]. The same author found that a 1 mm step is below the 2 mm bound of the step size, at which the strength limit of the mill frame is reached.

Because of the steady state development of the exit gauge, the effective dynamic behaviour of the mill due to a step in hydraulic stroke set point is the difference between the response of a step in hydraulic stroke and the response of a steady state simulation.

3.3.2 Speed Steps, $\delta v_{bc}, \delta v_{fc}$

Maximum values of speed steps were applied during simulation of speed step tests. The thought behind this decision was to obtain the maximum effect on the centerline output gauge [4]. An upper limit for the speed steps was the maximum value (i.e. a stress value of 200 MPa) for the strip back and front tension above the set up stress value of 8 MPa. The following relationship was in [4] the basis of the step size and duration of the step:

$$E_{ss} h_i w L_{rgcf}^{-1} \Delta v_c \Delta t_{step} = 2 \cdot 10^8 h_i w - T_{i\ setup} \tag{3.3}$$

where $i \in [1,2]$ for roll gap entrance and exit respectively. E_{ss} is Young's modulus for stainless steel, w the strip width, h the strip thickness and L_{rgcf} the length of the strip between the roll gap and the coiler furnace. A speed step $\Delta v_c = \pm 0.2$ ms^{-1} and a step duration $\Delta t_{step} = 60 \cdot 10^{-3}$ s was used.

3.4 Identification

In this section the inputs applied to the simulator as well as the corresponding output responses are given in the form of graphs and are discussed heuristically.

Three different linear models have been identified. In this work they will be called the first, the second and the third linear model and are given and discussed in sections 3.4.1, 3.4.2 and 3.4.3 respectively. Tab. 3.2 gives an overview of the differences between these three LTI models with respect to four criteria listed in the first column of the table.

Because of long simulation times involved (in excess of 6 days for 10 s of process time on a Pentium III, 533 MHz) to produce data for system identification purposes, the amount of data was sufficient to fit models but insufficient for a validation data range. For some of the transfer functions the quality of fit is however given in terms of auto-correlation plots of the error signal of the model output and also in terms of cross-correlation plots of the error signal and the input of a model.

Table 3.2: Differences between the three identified linear models.

Linear Model	1	2	3
Is TM part of simulator ?	SID data for all transfer functions, except for $g_{11}(s)$, were generated with the TM being part of the simulator.	SID data for all transfer functions were generated with the TM being part of the simulator.	SID data for all transfer functions were generated with the TM being part of the simulator.
Are non zero off-diagonal transfer functions present ?	Non zero off-diagonal transfer functions are: $g_{21}(s), g_{31}(s), g_{23}(s)$ and $g_{32}(s)$.	This linear model is decoupled, i.e. no non zero off-diagonal transfer functions.	All off-diagonal transfer functions are non zero.
Is gauge meter compensation incorporated in simulator ?	No	Yes	Yes
Are tensions controlled in an inner loop ?	No	Yes	Yes

3.4.1 First Linear Model

3.4.1.1 The Transfer Function $g_{11}(s)$

The transfer function $g_{11}(s)$ relates hydraulic stroke as input to centerline exit gauge as output, i.e. it relates exit gauge to that manipulated variable by which it is influenced most directly. Because constant exit gauge is a measure of strip quality, $g_{11}(s)$ represents the most important transfer function of the process. Its model was fitted as

$$g_{11}(s) = \frac{-8.2551 \cdot 10^{-2}}{s + 1.9942 \cdot 10^{-1}} e^{-2.5 \cdot 10^{-2} s} = \frac{-4.1936 \cdot 10^{-1}}{5.0145 s + 1} e^{-2.5 \cdot 10^{-2} s} . \quad (3.4)$$

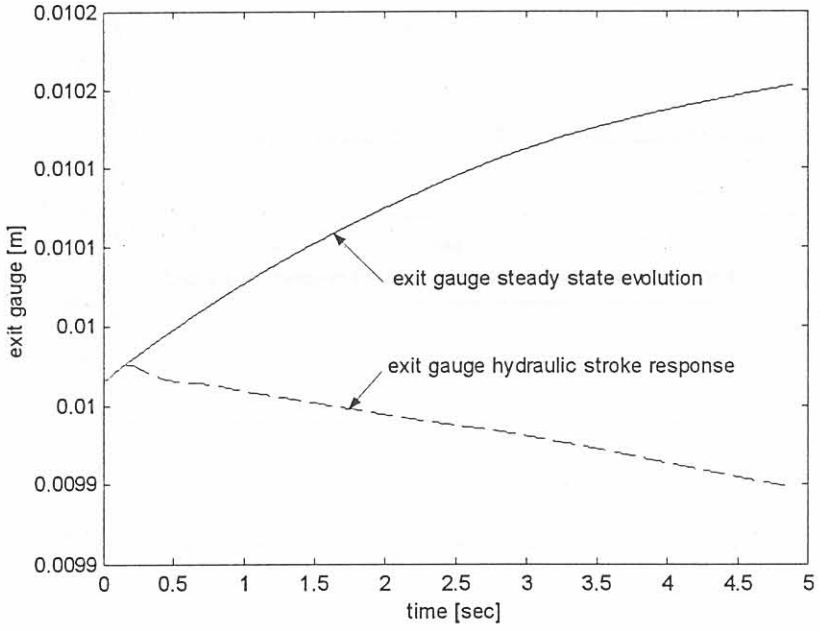

Figure 3.3: Steady state evolution of exit gauge and trend of exit gauge due to a hydraulic actuator stroke of 1 mm.

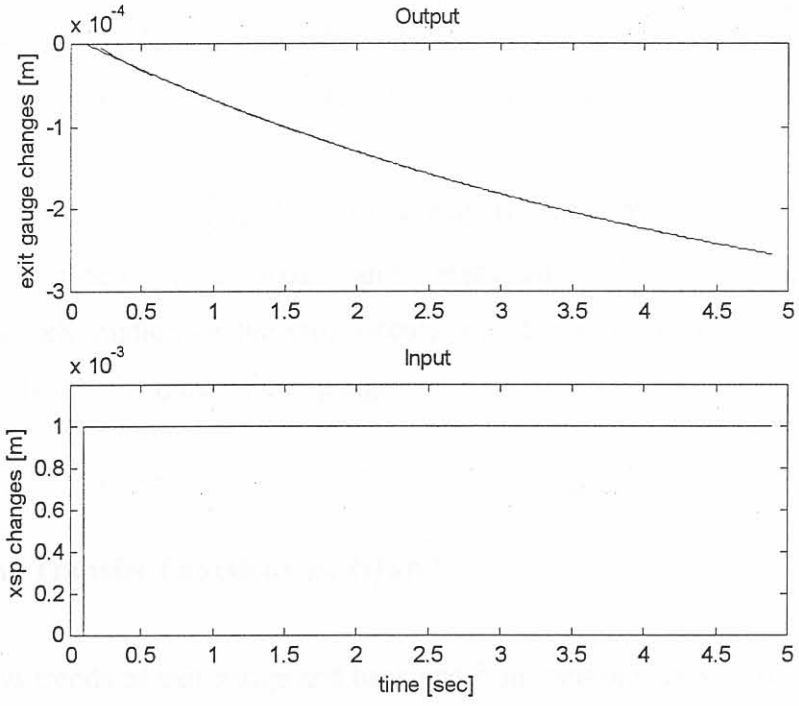

Figure 3.4: I/O data for the identification of $g_{11}(s)$ in the first linear model. (for outputs: solid: model output, dashed: measured output).

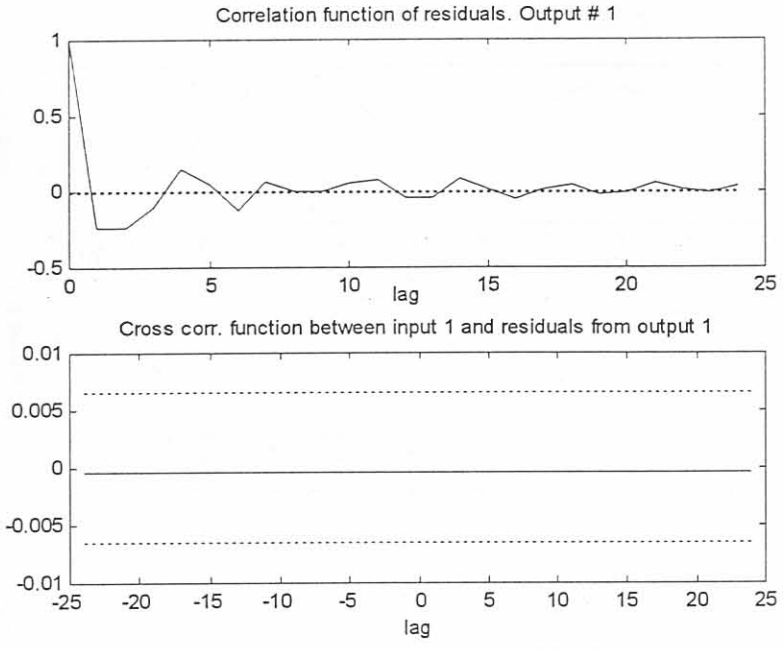

Figure 3.5: Correlation and cross correlation plots of the fitted model for $g_{11}(s)$. The dotted lines indicate the 99 % confidence level.

The output data for this transfer function as given in Fig. 3.4 was obtained by subtracting the steady state evolution of the exit thickness in Fig. 3.3 from the exit thickness data which resulted from the application of a hydraulic actuator stroke (also in Fig. 3.3). This is done in order to obtain the dynamic effect due to actuator stroke set point change.

As shown with Fig. 3.4, $g_{11}(s)$ is of a negative first order form with a delay of milliseconds. This delay of exit gauge can be explained by elastic mill stretch taking place before plastic deformation of the strip occurs, i.e. it is due to the time constant of mill stretch being shorter than that of exit gauge.

3.4.1.2 The Transfer Functions $g_{21}(s)$ and $g_{31}(s)$

Fig. 3.6 shows trends of exit gauge and back and front tensions for steady state, i.e. no step input, with the tensions allowed to vary uncontrolled. It can be seen from Fig. 3.6 that as exit gauge increases, i.e. as the roll gap opens, tensions also increase.

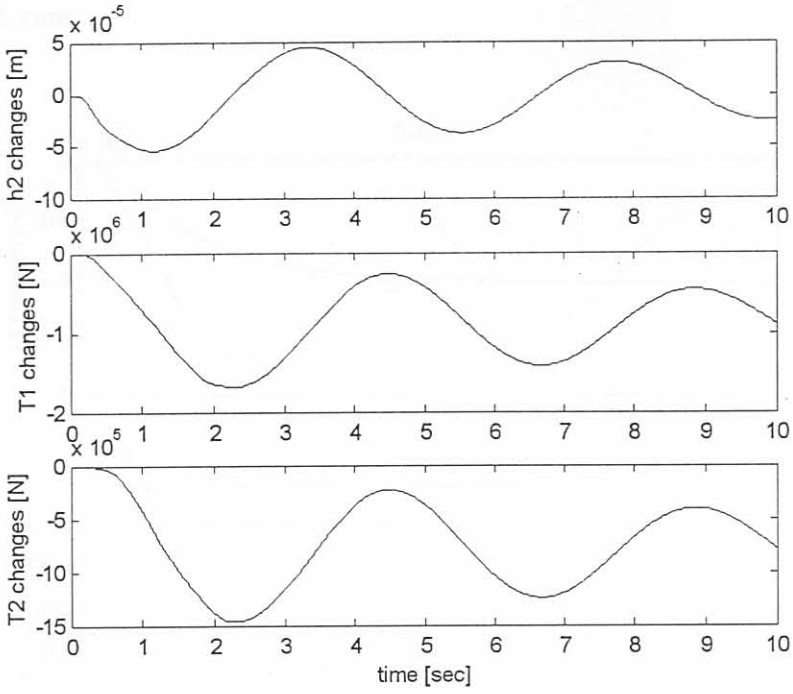

Figure 3.6: Trends of h_2, T_1 and T_2 with tensions uncontrolled and without application of steps on inputs.

The increase in front tension is caused by a decrease in exit speed, v_2, of the strip at the roll gap. v_2 decreases because the material flow, $h_1 v_1$ or $h_2 v_2$, through the roll gap changes in such a way that more material is allowed to travel through the roll gap, i.e. increase of v_1, but not enough to let v_2 increase, because h_2 increases in such a way that v_2 decreases in order for mass flow continuity to hold through the roll gap, i.e.

$$h_1 v_1 = h_2 v_2 \tag{3.5}$$

Tensions then increase to such an extent that they cause material deformation, which results in a thinner strip and therefore decrease of exit thickness as can be seen from Fig. 3.6.

Figures 3.7 and 3.9 show the input/output data that was used for the identification of the transfer functions $g_{21}(s)$ and $g_{31}(s)$ respectively. $g_{21}(s)$ and $g_{31}(s)$ relate hydraulic stroke set point change as input to back and front tension changes respectively as outputs. The output data for $g_{21}(s)$ and $g_{31}(s)$ was obtained by a subtraction similar as was done

for $g_{11}(s)$ in the previous section. It can be seen that the amplitude of tension oscillations decreases with time.

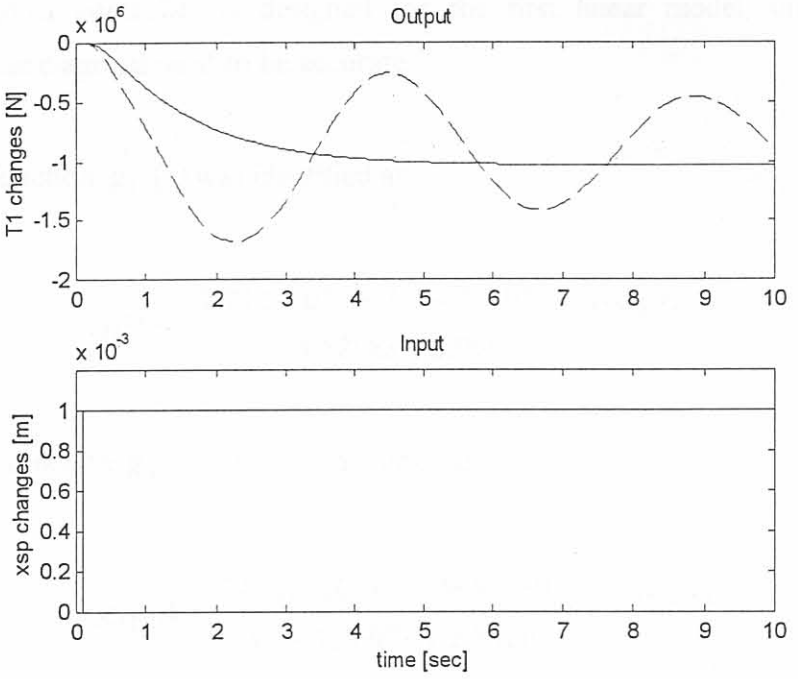

Figure 3.7: I/O data for the identification of $g_{21}(s)$ in the first linear model. (for outputs: solid: model output, dashed: measured output).

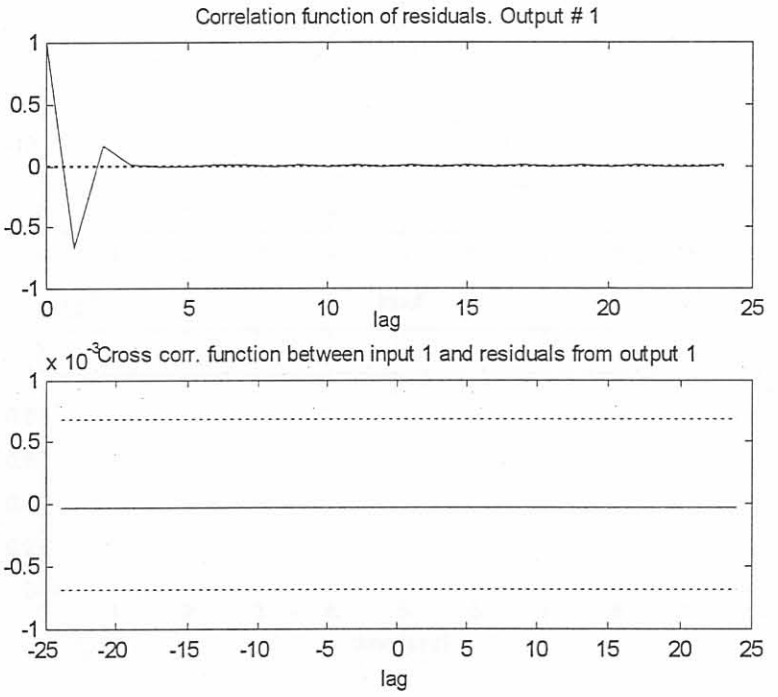

Figure 3.8: Correlation and cross correlation plots of the fitted model for $g_{21}(s)$. The dotted lines indicate the 99 % confidence level.

During identification of $g_{21}(s)$ and $g_{31}(s)$ it was found that high order models improved the accuracy of the fit. High order models are however impractical for controller design. Since a diagonal controller is designed for the first linear model, only the transfer functions on the diagonal need to be accurate.

The transfer function $g_{21}(s)$ was identified as

$$g_{21}(s) = \frac{7.712 \cdot 10^4 s - 3.0847 \cdot 10^9}{s^2 + 4.5298s + 2.966} \cdot e^{-7.25 \cdot 10^{-2} s}, \tag{3.6}$$

while transfer function $g_{31}(s)$ has been obtained as

$$g_{31}(s) = \frac{6.4215 \cdot 10^4 s - 2.5685 \cdot 10^9}{s^2 + 4.2697s + 2.8926} \cdot e^{-7.75 \cdot 10^{-2} s}. \tag{3.7}$$

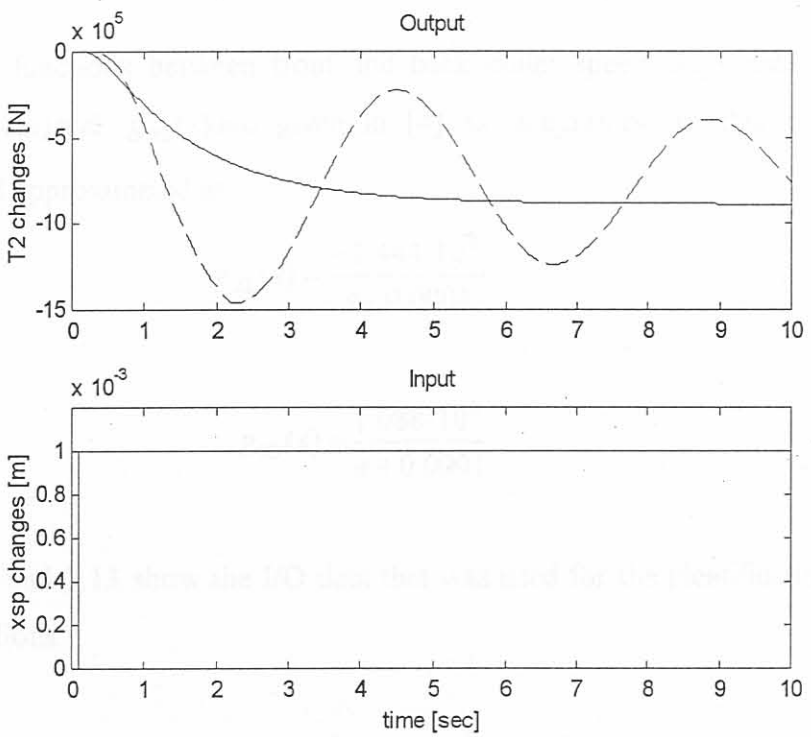

Figure 3.9: I/O data for the identification of $g_{31}(s)$ in the first linear model. (for outputs: solid: model output, dashed: measured output).

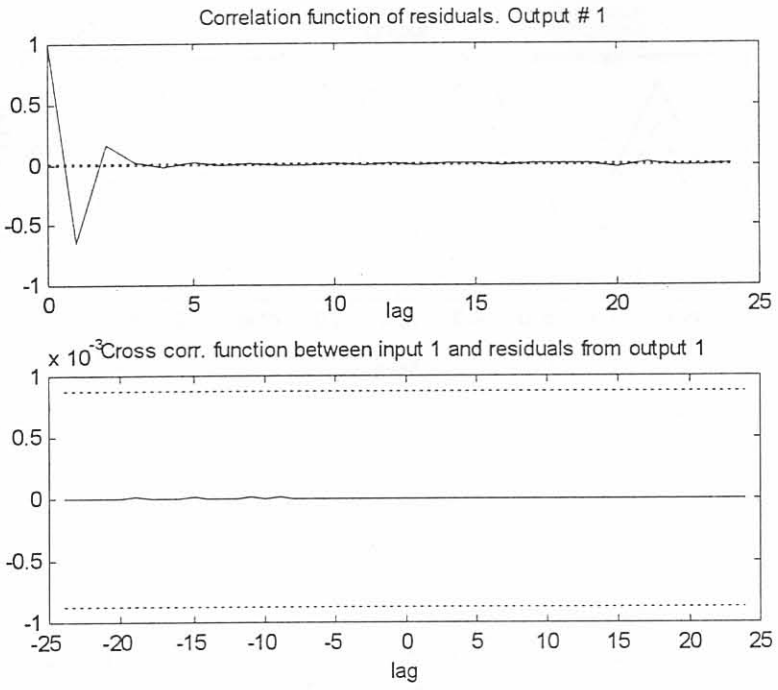

Figure 3.10: Correlation and cross correlation plot of the fitted model for $g_{31}(s)$ in the first linear model. The dotted lines indicate the 99% confidence level.

3.4.1.3 The Transfer Functions $g_{22}(s)$ and $g_{33}(s)$

The transfer functions between front and back coiler speed steps and front and back tensions, $g_{33}(s)$ and $g_{22}(s)$ are given in [4] as integrators. In this work they were identified and approximated as

$$g_{22}(s) = \frac{-1.444 \cdot 10^8}{s + 0.0001} \tag{3.8}$$

and

$$g_{33}(s) = \frac{1.088 \cdot 10^8}{s + 0.0001}. \tag{3.9}$$

Figures 3.11 and 3.13 show the I/O data that was used for the identification of these two transfer functions.

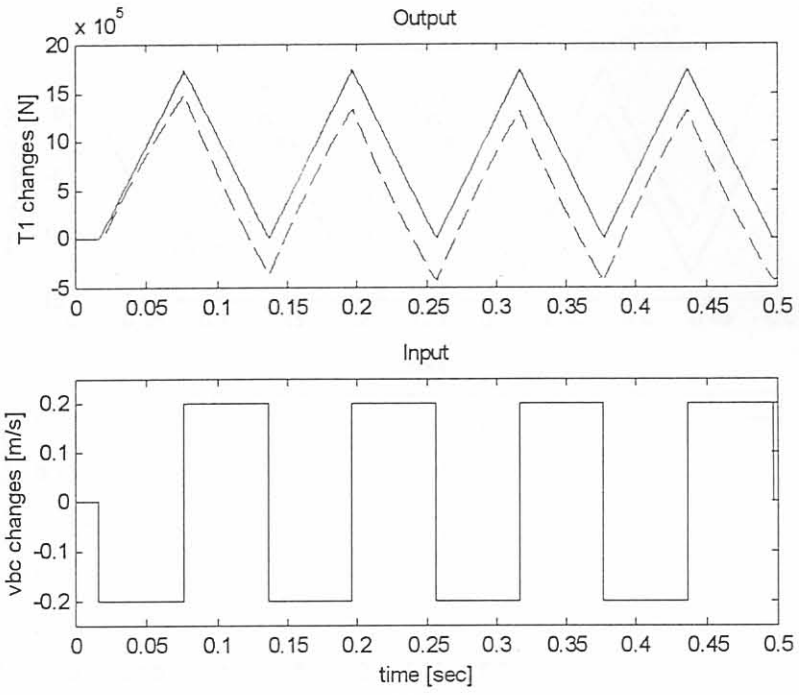

Figure 3.11: I/O data for the identification of $g_{22}(s)$ in the first linear model. (for outputs: solid: model output, dashed: measured output).

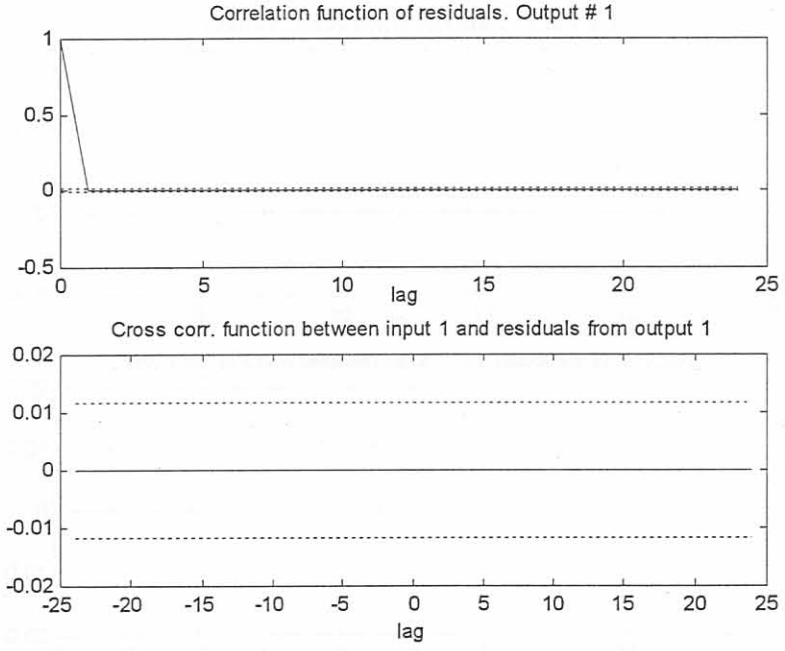

Figure 3.12: Correlation and cross correlation plot of the fitted model for $g_{22}(s)$ in the first linear model. The dotted lines indicate the 99% confidence level.

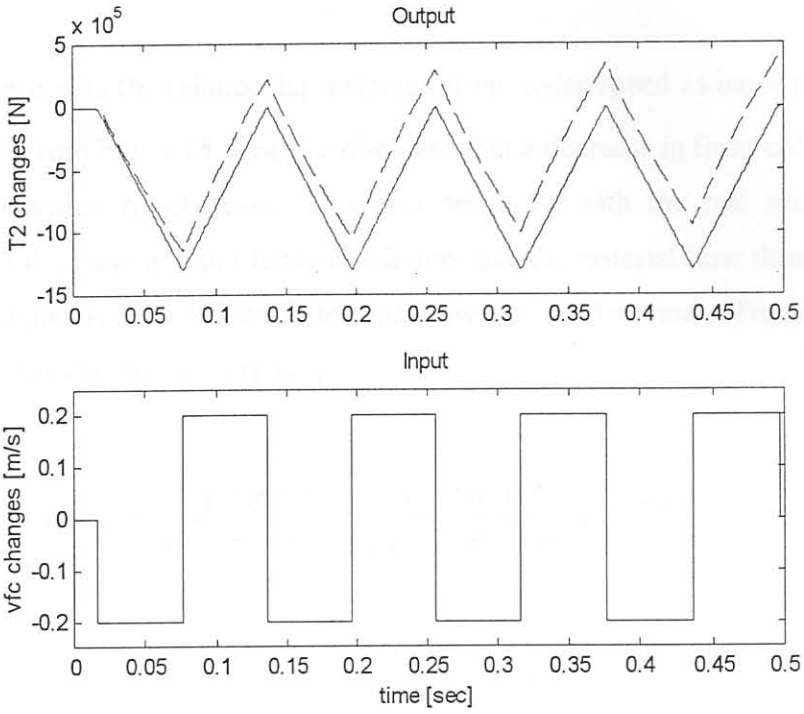

Figure 3.13: I/O data for the identification of $g_{33}(s)$ in the first linear model. (for outputs: solid: model output, dashed: measured output).

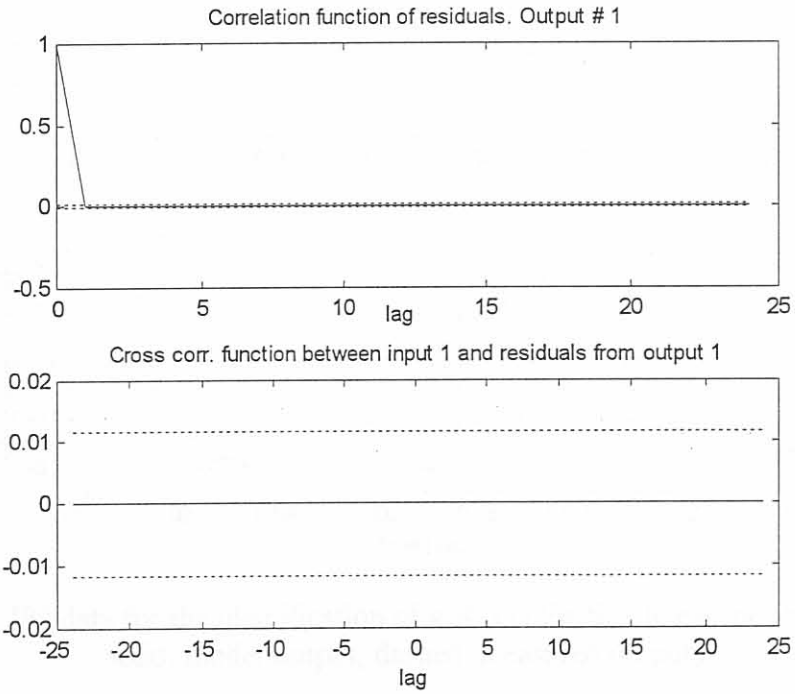

Figure 3.14: Correlation and cross correlation plot of the fitted model for $g_{33}(s)$ in the first linear model. The dotted lines indicate the 99% confidence level.

3.4.1.4 The Transfer Functions $g_{23}(s)$ and $g_{32}(s)$

$g_{23}(s)$ represents the relationship between front coiler speed as input and back tension as output. From Fig. 3.15 it can be observed that a decrease in front coiler speed causes the back tension to decrease. This also conforms with the real situation since the associated decrease in front tension will decrease the material flow through the roll gap and consequently also the back tension however not by much. The transfer function that was identified for $g_{23}(s)$ is

$$g_{23}(s) = \frac{-1.2461 \cdot 10^4 s + 6.1196 \cdot 10^8}{s^2 + 4.0453 \cdot 10 s + 4.0318 \cdot 10^2} \cdot e^{-2.15 \cdot 10^{-2} s} \quad (3.10)$$

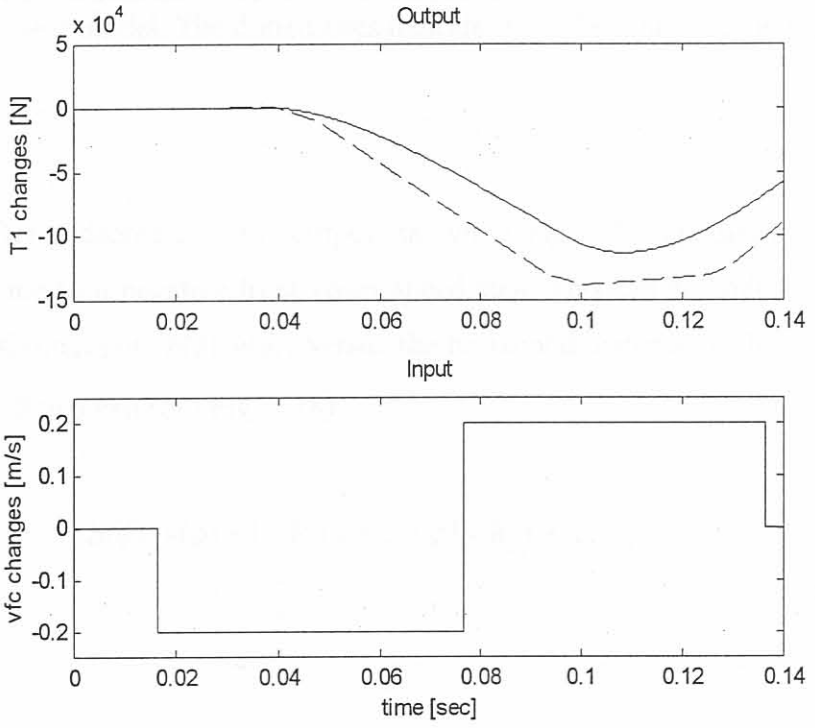

Figure 3.15: I/O data for the identification of $g_{23}(s)$ in the first linear model (for outputs: solid: model output, dashed: measured output).

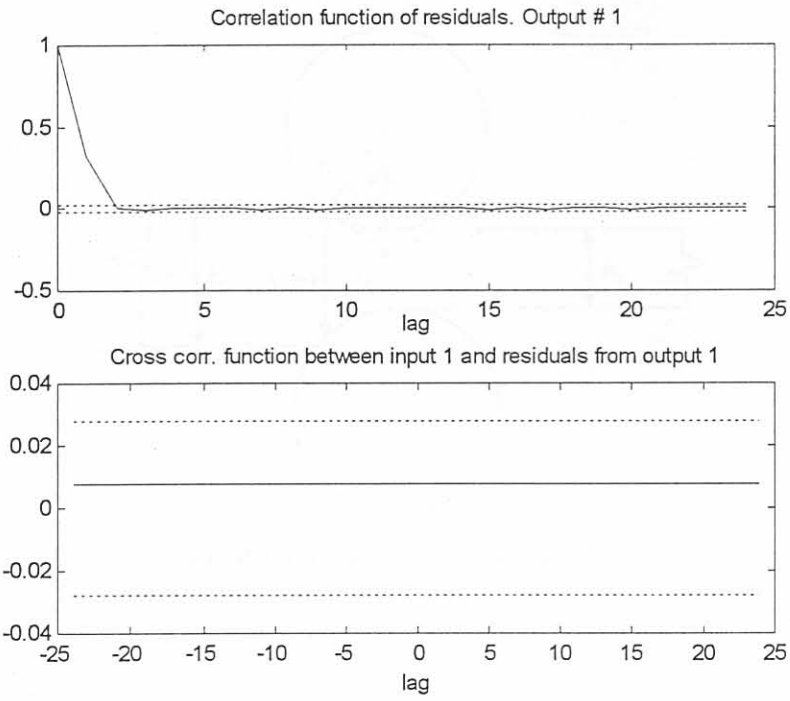

Figure 3.16: Correlation and cross correlation plot of the fitted model for $g_{23}(s)$ in the first linear model. The dotted lines indicate the 99% confidence level.

A flat part after a decrease of the output, shown in Fig. 3.15, appears like saturation of back tension due to a negative front coiler speed step. This can be understood by using a graph of the throughput, $h(\phi)\cdot v(\phi)$, versus the horizontal distance of the neutral point, at ϕ, from the roll gap exit (see Fig. 3.18).

$$h(\phi)\cdot v(\phi)=\left(2R'(1-\cos\phi)+h_2\right)v_r\cos\phi \quad , \tag{3.11}$$

where

v_r: peripheral speed of work rollers and

$R'\sin\phi$: horizontal distance of neutral point from roll gap exit.

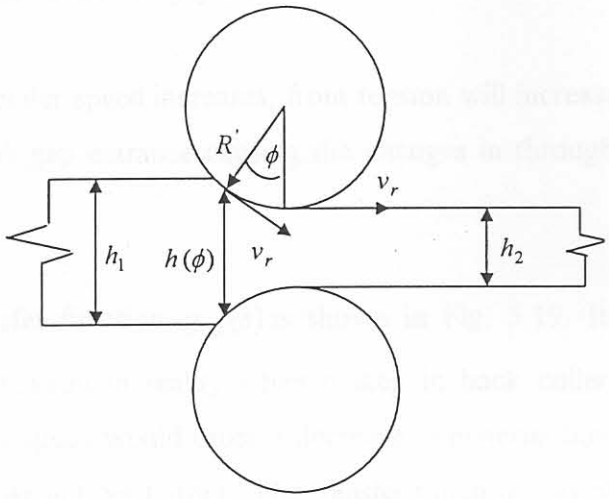

Figure 3.17: Roll gap geometry.

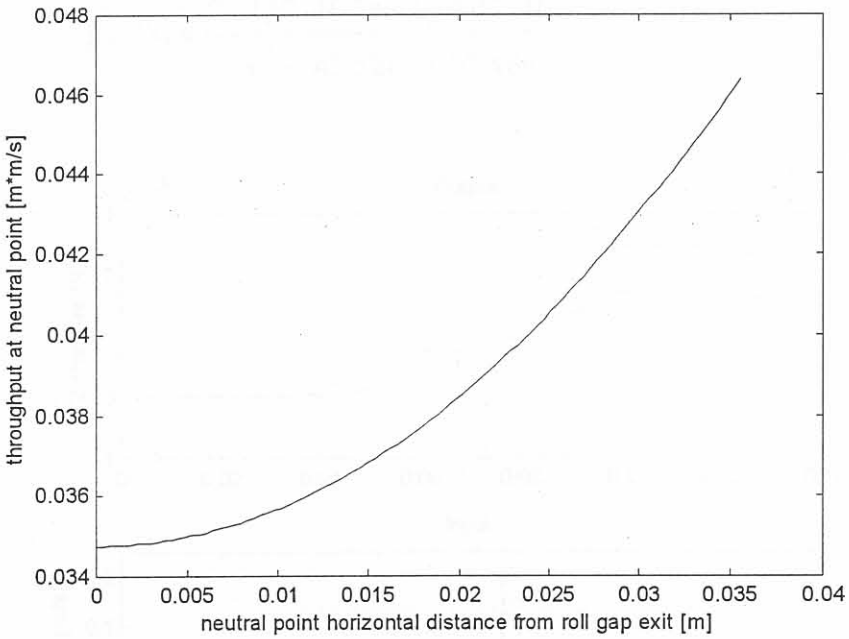

Figure 3.18: Throughput versus horizontal position of the neutral point from the roll gap exit.

When front tension decreases, which happens for a negative step in front coiler speed, a surplus of back tension, will cause the neutral point to shift towards the exit of the roll gap [24] decreasing the throughput , $h(\phi)\cdot v(\phi)$, and causing the back tension to decrease only until it saturates. The saturation occurs because the changes in throughput are only negligible, when the neutral point is close to the roll gap exit as Fig. 3.18 shows. This

explains why nonlinear saturation behaviour of back tension appears as a result of the neutral point being close to the roll gap exit.

However when front coiler speed increases, front tension will increase and shift the neutral point closer to the roll gap entrance causing the changes in throughput to become more pronounced.

I/O data for the transfer function $g_{32}(s)$ is shown in Fig. 3.19. It reflects what would happen to the front tension in reality when a step in back coiler speed is applied. A decrease in back coiler speed would cause a decrease in material flow through the roll gap and therefore an increase in front tension. The transfer function was obtained as

$$g_{32}(s) = \frac{2.3159 \cdot 10^4 s - 9.0907 \cdot 10^8}{s^2 + 43.528s + 92.486} \cdot e^{-2.0 \cdot 10^{-2} s} \quad (3.12)$$

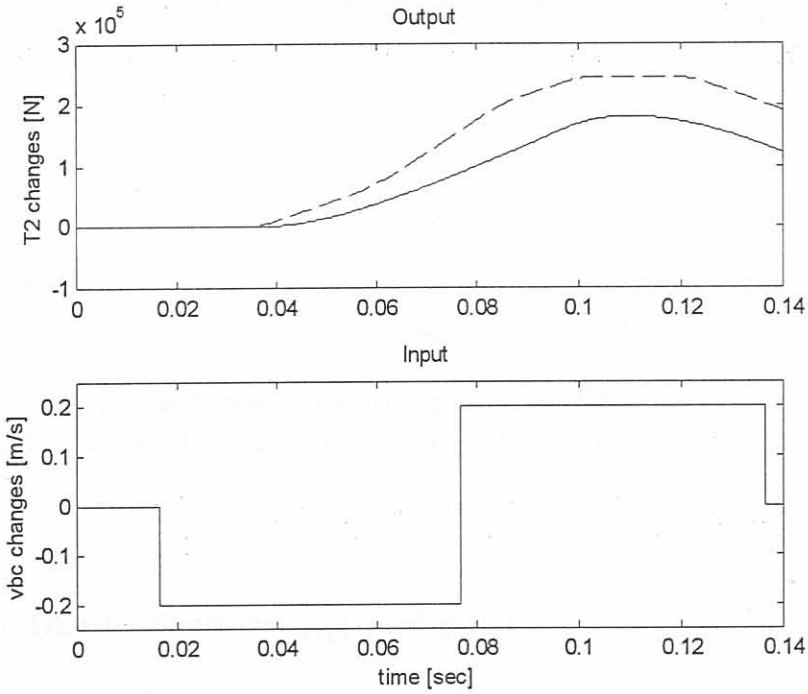

Figure 3.19: I/O data for the identification of $g_{32}(s)$ in the first linear model (for outputs: solid: model output, dashed: measured output).

The saturation phenomena of front tension due to a negative step in back coiler speed shown in Fig. 3.19 can be explained in a similar way as the saturation of back tension in Fig. 3.15.

The cross correlation plots are an indication of the linear independence between the input and the residual of the real and estimated model. The offsets of the cross correlation functions in figures 3.16 and 3.20 could therefore be caused by the attempt made to fit linear models on I/O data which shows a nonlinear saturation effect in figures 3.15 and 3.19.

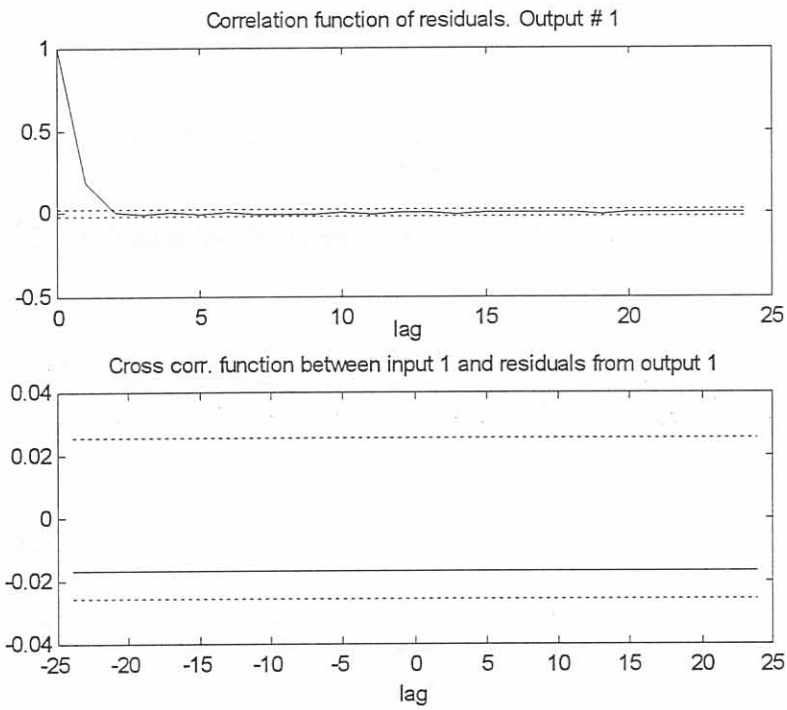

Figure 3.20: Correlation and cross correlation plot of the fitted model for $g_{32}(s)$ in the first linear model. The dotted lines indicate the 99% confidence level.

3.4.1.5 The Transfer Functions $g_{12}(s)$ and $g_{13}(s)$

The influence of the step in back coiler speed given in Fig. 3.21 on exit gauge is by a factor of approximately 60 smaller than the influence of a step in hydraulic actuator stroke set point given in Fig. 3.4. Therefore the influence of back coiler speed on exit gauge was neglected and the transfer function was chosen as

$$g_{12}(s) = 0. \tag{3.13}$$

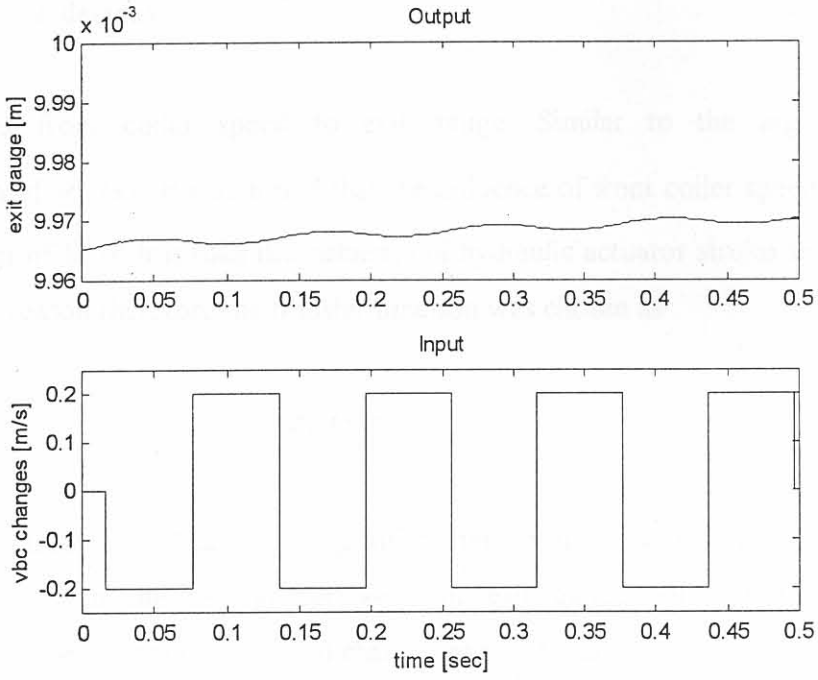

Figure 3.21: I/O data for the identification of $g_{12}(s)$ in the first linear model.

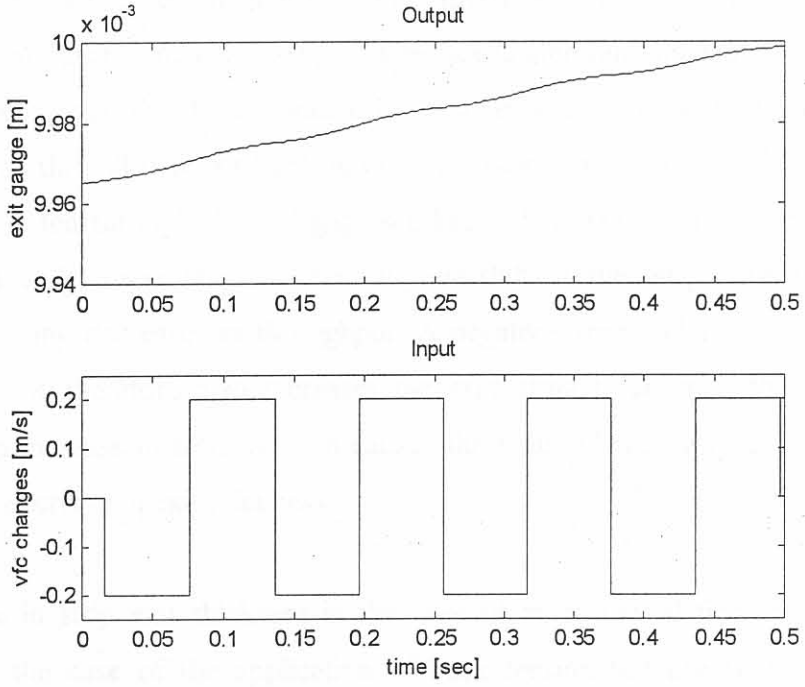

Figure 3.22: I/O data for the identification of $g_{13}(s)$ in the first linear model.

Fig. 3.21 is showing the I/O data for $g_{12}(s)$. From this figure one can see that for a decrease in back coiler speed and therefore an increase in back tension the trend of exit gauge is changed into a decreasing trend. This makes sense from a practical point of view

since tension helps with the deformation, i.e. thickness reduction, of the material, causing the exit gauge to decrease.

$g_{13}(s)$ relates front coiler speed to exit gauge. Similar to the argument for the identification of $g_{12}(s)$, it was found that the influence of front coiler speed on exit gauge is by an order of $1 \cdot 10^2$ less than the influence of hydraulic actuator stroke set point change. For a similar reason therefore the transfer function was chosen as

$$g_{13}(s) = 0 \ . \tag{3.14}$$

One can see from Fig. 3.22 that a positive step in front coiler speed causes a slight decreasing trend in the second derivative of exit gauge which reflects a plausible relationship between front coiler speed changes and exit gauge.

If the I/O data of $g_{12}(s)$ is compared with that of $g_{13}(s)$, the question arises why exit gauge in general increases when front coiler speed steps are applied while it shows an almost constant general trend when back coiler speed steps are applied. The reason for the decreasing exit gauge due to a negative back coiler speed step is that the neutral point moves towards the roll gap exit because of an increased back tension, which indicates that less material is fed through the roll gap (see Fig. 3.18) resulting in a thinner strip. With negative back coiler speed steps the neutral point shifts to the left part of the curve in Fig. 3.18, thus causing decreases in throughput. A negative front coiler speed step decreases front tension. It therefore also increases the separating force such that exit thickness increases. An increase in front tension causes the required rolling force to decrease and with it also a decrease in exit thickness.

The decrease in strip exit thickness in the case of an increased front tension is not as severe as in the case of the application of back tension because with increased front tension the neutral point shifts towards the roll gap entrance resulting in more throughput. One therefore has more throughput together with a surplus of rolling force which cancel each other to an extent.

Back tension is also known to be twice as effective as front tension in decreasing the separating force between the work rolls [20] thus decreasing the strip exit thickness more severely when it is applied.

3.4.2 Second Linear Model

3.4.2.1 The Transfer Function $g_{11}(s)$

Fig. 3.23 shows the input and output data used to identify $g_{11}(s)$. The output represents the exit gauge steady state evolution subtracted from the exit gauge trend during an input as shown by the bottom curve of Fig. 3.23.

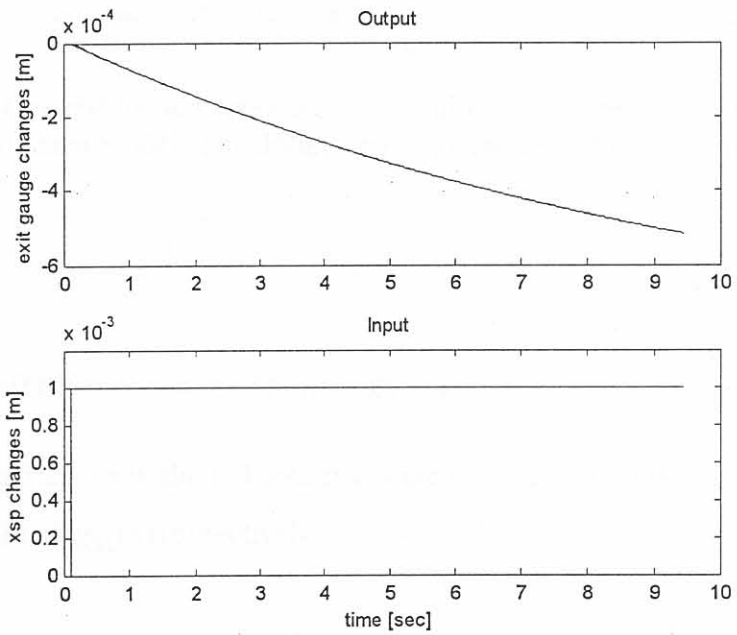

Figure 3.23: I/O data for the identification of $g_{11}(s)$ in the second linear model. (for outputs: solid: model output, dashed: measured output).

From Fig.3.23 and also from the steady state gain of $g_{11}(s)$ it can be registered that although the gauge meter compensation was present in the simulation, the input step of 1mm is not completely converted into change of exit gauge but only to about 87 %. This can be attributed to the fact that tensions were not regulated at perfectly constant values. The transfer function obtained for $g_{11}(s)$ is

$$g_{11}(s) = \frac{-8.3334 \cdot 10^{-2}}{s + 9.5039 \cdot 10^{-2}} \cdot e^{-2.5 \cdot 10^{-2} s} = \frac{-0.8768}{10.52s + 1} \cdot e^{-2.5 \cdot 10^{-2} s}. \qquad (3.15)$$

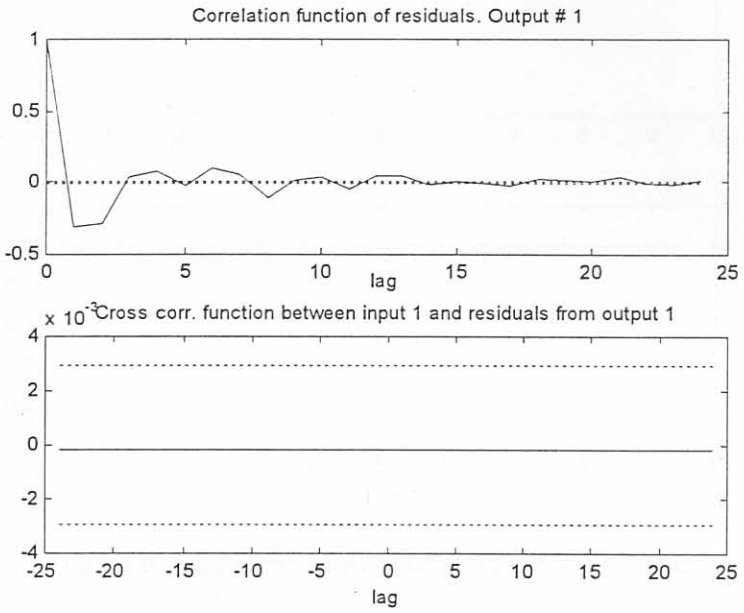

Figure 3.24: Correlation and cross correlation plot of the fitted model for $g_{11}(s)$ in the second linear model. The dotted lines indicate the 99% confidence level.

3.4.2.2 Transfer Functions $g_{21}(s)$ and $g_{31}(s)$

Figures 3.25 and 3.26 show the I/O data that were used to make a decision on the transfer functions $g_{21}(s)$ and $g_{31}(s)$ respectively.

Because of the close to constant outputs of $g_{21}(s)$ and $g_{31}(s)$ it was decided to use

$$g_{21}(s) = 0 \qquad (3.16)$$

and

$$g_{31}(s) = 0. \qquad (3.17)$$

Constant output data for $g_{21}(s)$ and $g_{31}(s)$ were also obtained by subtracting the steady state simulations of the tensions from the tension trends obtained during a hydraulic stroke step test as done for the identification of $g_{11}(s)$.

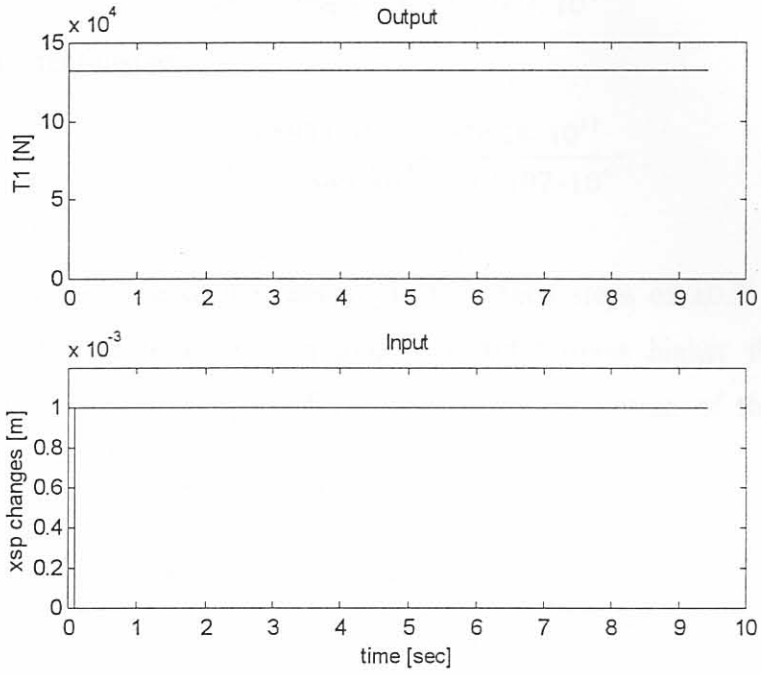

Figure 3.25: I/O data for the identification of $g_{21}(s)$ in the second linear model.

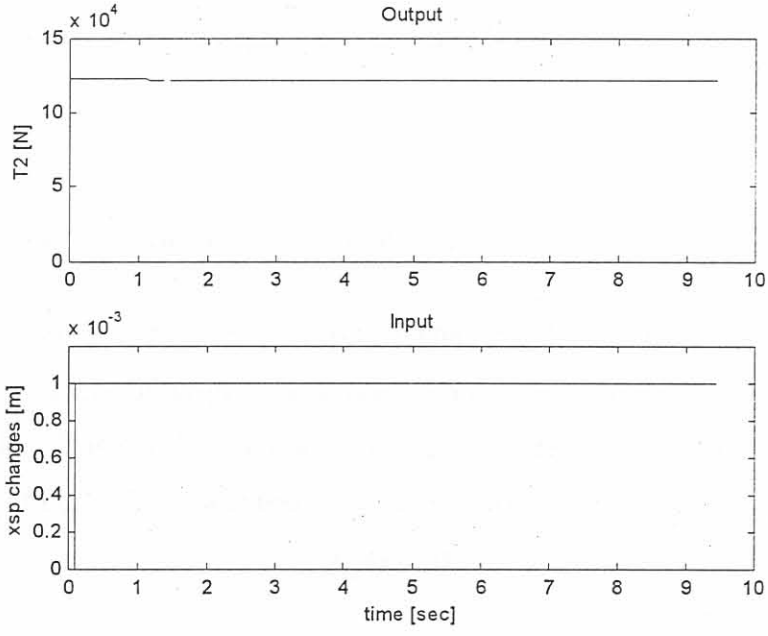

Figure 3.26: I/O data for the identification of $g_{31}(s)$ in the second linear model.

3.4.2.3 Transfer Functions $g_{22}(s)$ and $g_{33}(s)$

Figures 3.27 and 3.29 show the I/O data used for the identification of $g_{22}(s)$ and $g_{33}(s)$.

$g_{22}(s)$ was identified as

$$g_{22}(s) = \frac{-6.9002 \cdot 10^6 s - 1.3594 \cdot 10^{12}}{s^2 + 9.0963 \cdot 10^3 s + 5.071 \cdot 10^6} \tag{3.18}$$

and $g_{33}(s)$ was identified as

$$g_{33}(s) = \frac{-4.5934 \cdot 10^6 s + 9.0628 \cdot 10^{11}}{s^2 + 8.1846 \cdot 10^3 s + 5.5107 \cdot 10^6} \tag{3.19}$$

The higher order response of the tensions to the speed steps of ±0.2 m/s is due to the control applied to the tensions at a frequency 1000 times higher than the sampling frequency of the outer main loop of the simulator. The design of these controllers is discussed in section 5.3.

In figures 3.28 and 3.30 auto and cross correlation plots are given for the models fitted for $g_{22}(s)$ and $g_{33}(s)$ respectively. The correlation present in the auto correlation plots of figures 3.28 and 3.30, indicate that the model structures for $g_{22}(s)$ and $g_{33}(s)$ can still be improved. It was found that their structural fit improved when models of a higher order than given above for $g_{22}(s)$ and $g_{33}(s)$ were identified. The cross correlation present for positive lags in figures 3.28 and 3.30 are a consequence of the improvable model structures.

3.4.2.4 Transfer Functions $g_{12}(s)$ and $g_{13}(s)$

The changes of exit gauge in response to step changes of ±0.2 m/s of the coiler speeds are more than two orders of magnitude smaller than in its response to a step of 1 mm in hydraulic stroke. This can be seen when comparing the output data of figures 3.31 and 3.33 with that of Fig. 3.23. It was therefore decided to use

$$g_{12}(s) = 0 \tag{3.20}$$

and

$$g_{13}(s) = 0 \tag{3.21}$$

for the second linear model of the nonlinear plant.

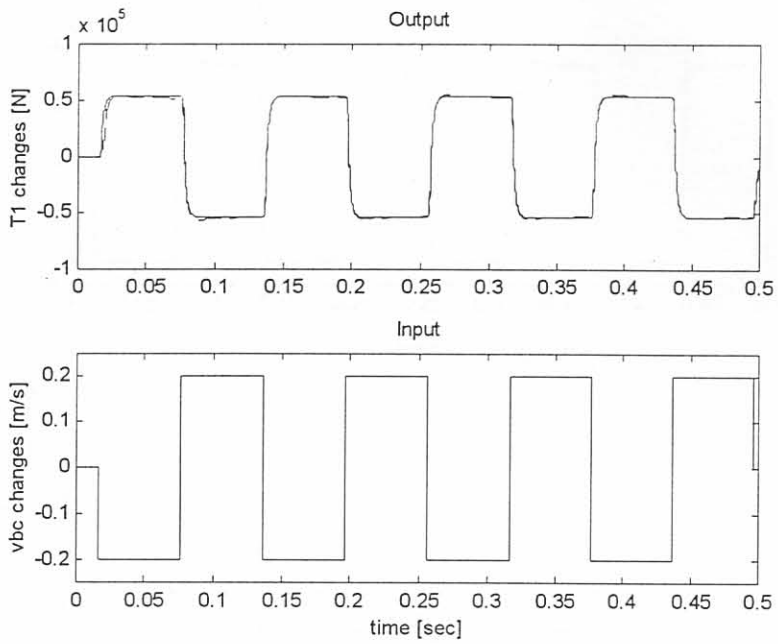

Figure 3.27: I/O data for the identification of $g_{22}(s)$ in the second linear model. (for outputs: solid: model output, dashed: measured output).

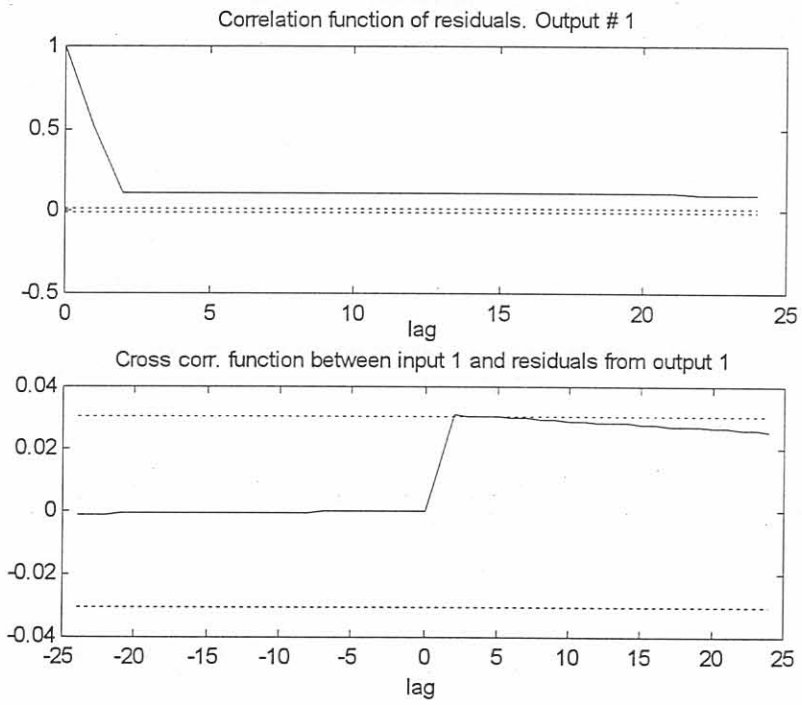

Figure 3.28: Correlation and cross correlation plot of the fitted model for $g_{22}(s)$ in the second linear model. The dotted lines indicate the 99% confidence level.

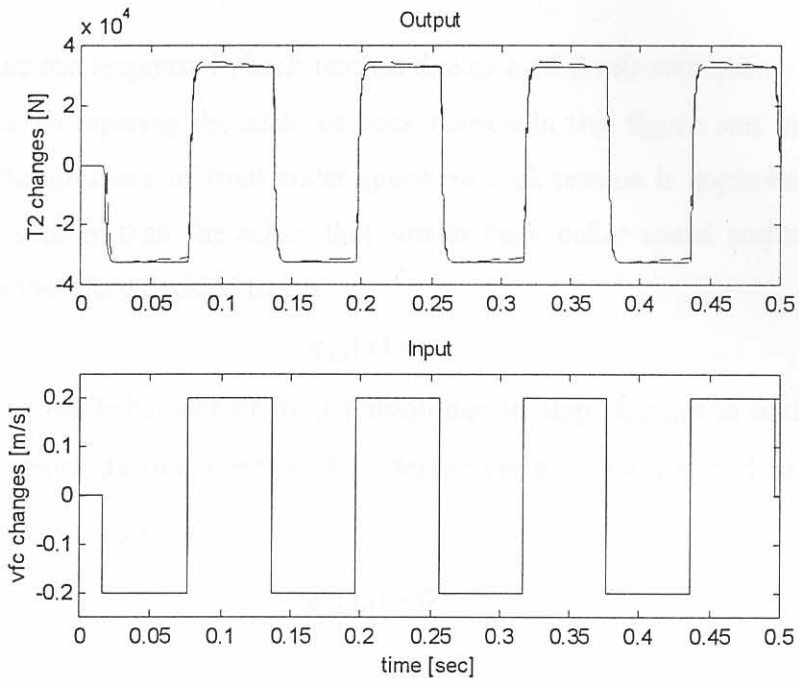

Figure 3.29: I/O data for the identification of $g_{33}(s)$ in the second linear model. (for outputs: solid: model output, dashed: measured output).

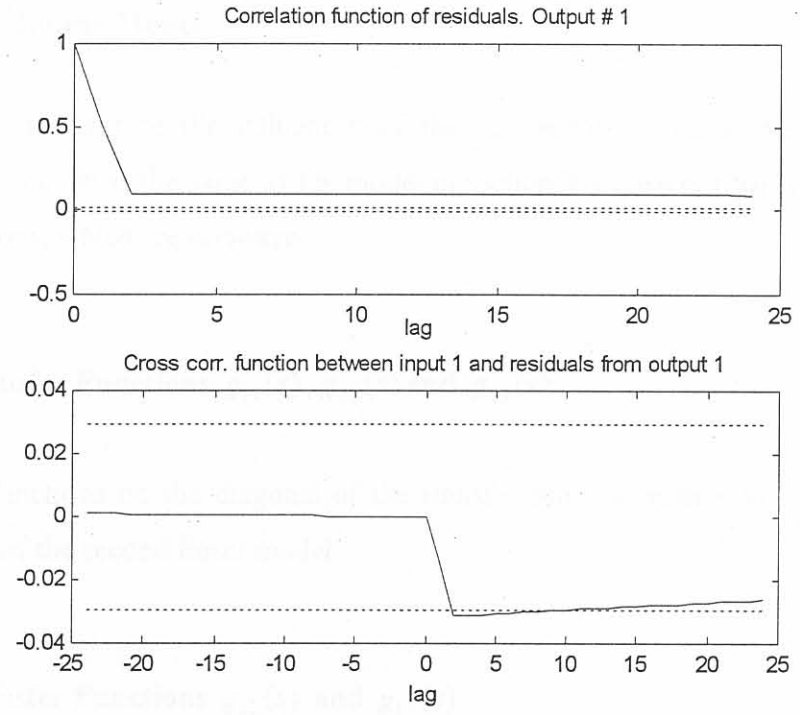

Figure 3.30: Correlation and cross correlation plot of the fitted model for $g_{33}(s)$ in the second linear model. The dotted lines indicate the 99% confidence level.

3.4.2.5 Transfer Functions $g_{23}(s)$ and $g_{32}(s)$

Fig. 3.37 shows the response in back tension due to a ±0.2 m/s step change in front coiler speed as input. Comparing the scale of back tension in this figure and in Fig. 3.27 one realizes that the influence of front coiler speed on back tension is approximately 5 orders of magnitude smaller than the effect that similar back coiler speed steps have on back tension. It was therefore decided to use

$$g_{23}(s) = 0 \ . \tag{3.22}$$

Fig. 3.35 shows the behaviour of front tension due to step changes in back coiler speed. Here similar arguments that were used to decide on $g_{23}(s)$ were used to determine the transfer function $g_{32}(s)$ as

$$g_{32}(s) = 0 \tag{3.23}$$

for the second linear model of the nonlinear plant.

3.4.3 Third Linear Model

In an attempt to capture the influences of the interactions a third linear model was identified. This model is the same as the model in section 3.4.2 except for the off-diagonal transfer functions, which are non-zero.

3.4.3.1 Transfer Functions $g_{11}(s), g_{22}(s)$ and $g_{33}(s)$

The transfer functions on the diagonal of the transfer function matrix in Eq. 3.1 are the same as those of the second linear model.

3.4.3.2 Transfer Functions $g_{12}(s)$ and $g_{13}(s)$

In figures 3.31 and 3.33, exit gauge shows integrator behaviour in response to coiler speed steps. As it was seen in figures 3.27 and 3.29 the response of the tensions to the same speed steps is almost proportional, i.e. the tensions respond with steps (see figures 3.21 and 3.22). It makes sense that the response of exit gauge to a step change in back and front

coiler speeds is a ramp such as in figures 3.31 and 3.33 when compared to the exit gauge response due to the same inputs in the first linear model (see figures 3.21 and 3.22). The relationship between tensions and exit gauge can thus be approached as integrators.

The transfer function $g_{12}(s)$ has been identified as

$$g_{12}(s) = \frac{1.342 \cdot 10^{-5}}{s + 0.01}, \tag{3.24}$$

while the transfer function $g_{13}(s)$ was estimated as

$$g_{13}(s) = \frac{-7.73 \cdot 10^{-6}}{s + 0.01} \cdot e^{-3.57 \cdot 10^{-3} s}. \tag{3.25}$$

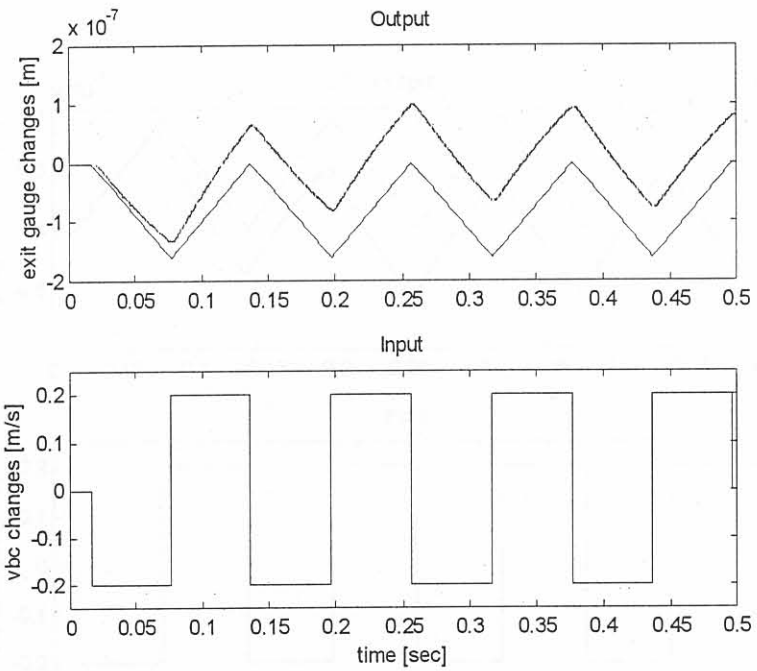

Figure 3.31: I/O data for the identification of $g_{12}(s)$ in the third linear model(for output: upper curve: measured output, lower curve: model output).

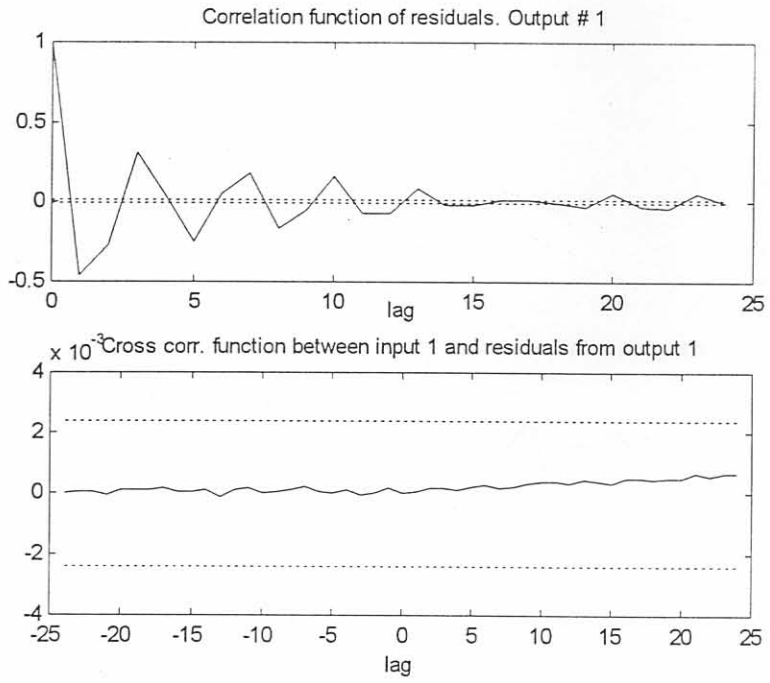

Figure 3.32: Correlation and cross correlation plot of the fitted model for $g_{12}(s)$ in the third linear model. The dotted lines indicate the 99% confidence level.

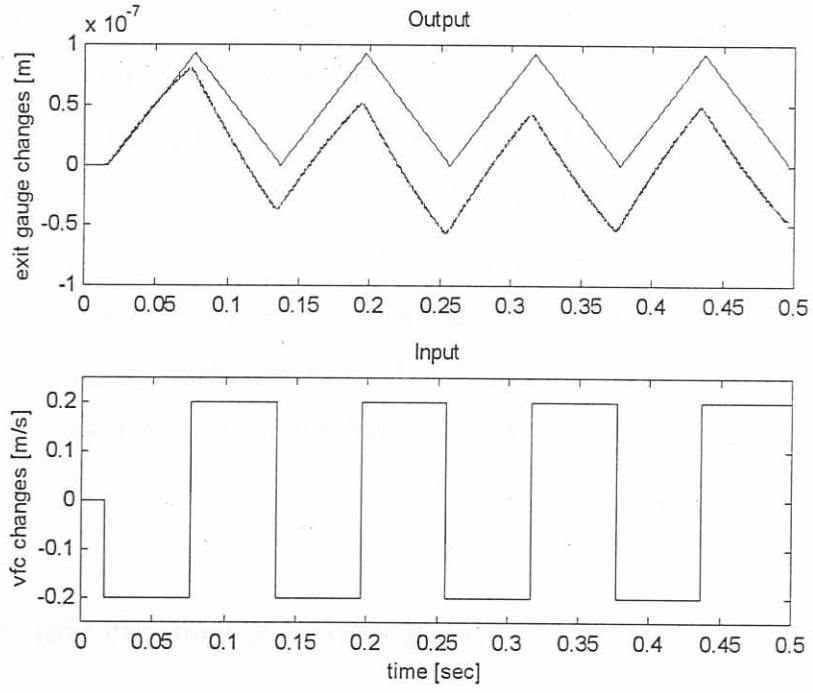

Figure 3.33: I/O data for the identification of $g_{13}(s)$ in the third linear model (for output: upper curve: model output, lower curve: measured output).

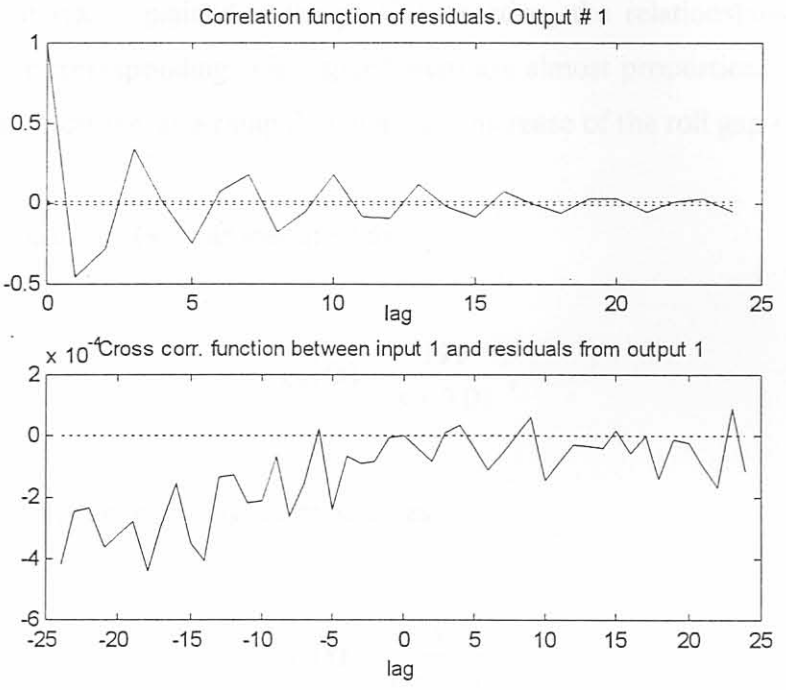

Figure 3.34: Correlation and cross correlation plot of the fitted model for $g_{13}(s)$ in the third linear model. The dotted lines indicate the 99% confidence level.

The cross correlation plot of $g_{13}(s)$ mainly shows correlation for negative lags, which means that output feedback occurs in the estimation of this transfer function. This could improve by changing the structure of the transfer function. The delay in $g_{13}(s)$ is only in the order of milliseconds and was added since with the application of front tension exit gauge must change first before back tension is affected. As an initial step towards controller design it was decided to use the transfer function as given in Eq. 3.25 since from its parameters it is assumed that it may have only a weak influence on exit gauge.

3.4.3.3 Transfer Functions $g_{32}(s)$ and $g_{23}(s)$

Fig. 3.35 shows the response of front tension to back coiler speed steps. For a negative back coiler speed step and thus increasing back tension the surplus of rolling force will cause the roll gap to become smaller and therefore deliver a thinner strip at a higher speed in order to maintain the throughput. This causes the front tension to drop. Because the exit gauge responds to back coiler speed steps and therefore to the back tension steps as a

ramp, the roll gap exit speed will also change as a ramp in order to maintain the throughput. As it was explained in the previous section, the relationships between strip tensions and their corresponding coiler speed steps are almost proportional. Therefore the front tension will decrease as a ramp due to a ramp increase of the roll gap exit speed.

The transfer function $g_{32}(s)$ was identified as

$$g_{32}(s) = \frac{191}{s + 0.01}, \tag{3.26}$$

and the transfer function $g_{23}(s)$ was estimated as

$$g_{23}(s) = \frac{-452.1}{s + 0.01} \cdot e^{-3.57 \cdot 10^{-3} s}. \tag{3.27}$$

A delay in the order of milliseconds was incorporated in this transfer function because of the dead time involved for the exit gauge to change due to a change in front tension. This change of exit gauge is then registered in a change in back tension. For example, if the front tension decreases as a negative step because of a step decrease in front coiler speed the exit gauge would increase as a ramp (see section 3.4.3.2) causing more material to pass through thereby increasing the entry speed as a ramp. This would then result in a proportional, i.e. also ramp increase of back tension.

Pertaining the auto correlation plots of the transfer function estimation for $g_{23}(s)$ (see Fig. 3.38), similar comments as those made about the auto correlation plots for $g_{13}(s)$ (see Fig. 3.34) in section 3.4.3.2 apply.

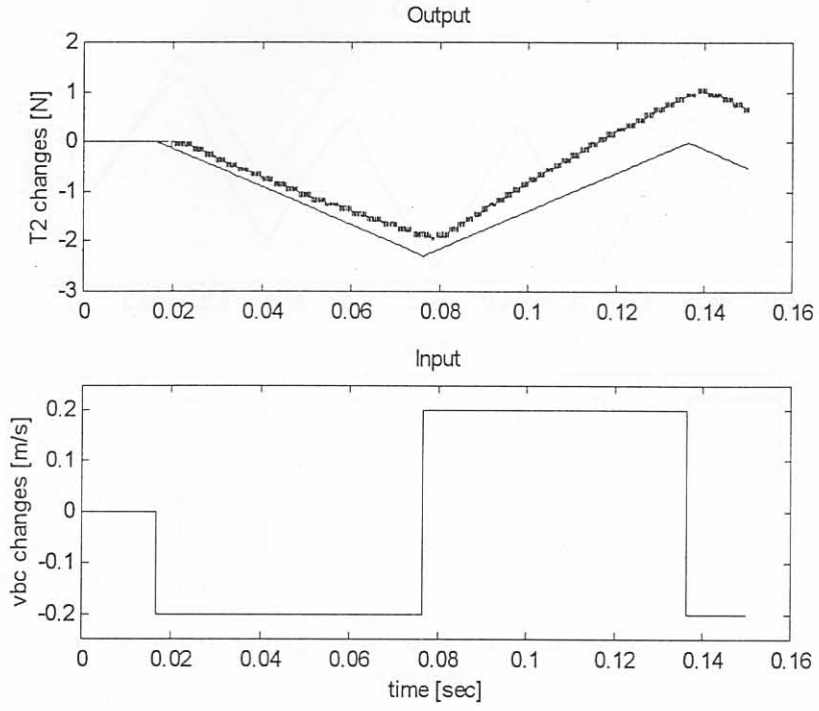

Figure 3.35: I/O data for the identification of $g_{32}(s)$ in the third linear model. (for outputs: upper curve: measured output, lower curve: model output).

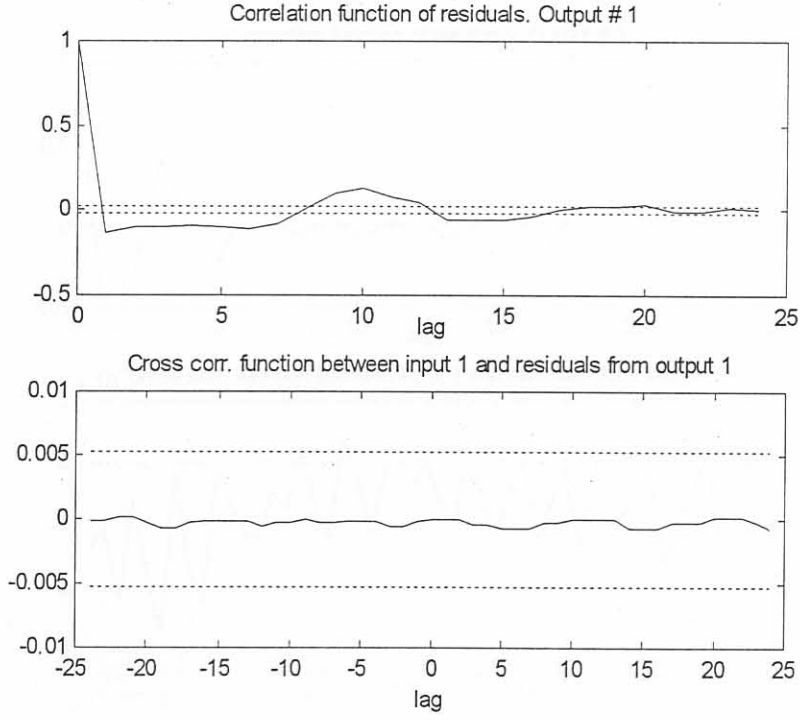

Figure 3.36: Correlation and cross correlation plot of the fitted model for $g_{32}(s)$ in the third linear model. The dotted lines indicate the 99% confidence level.

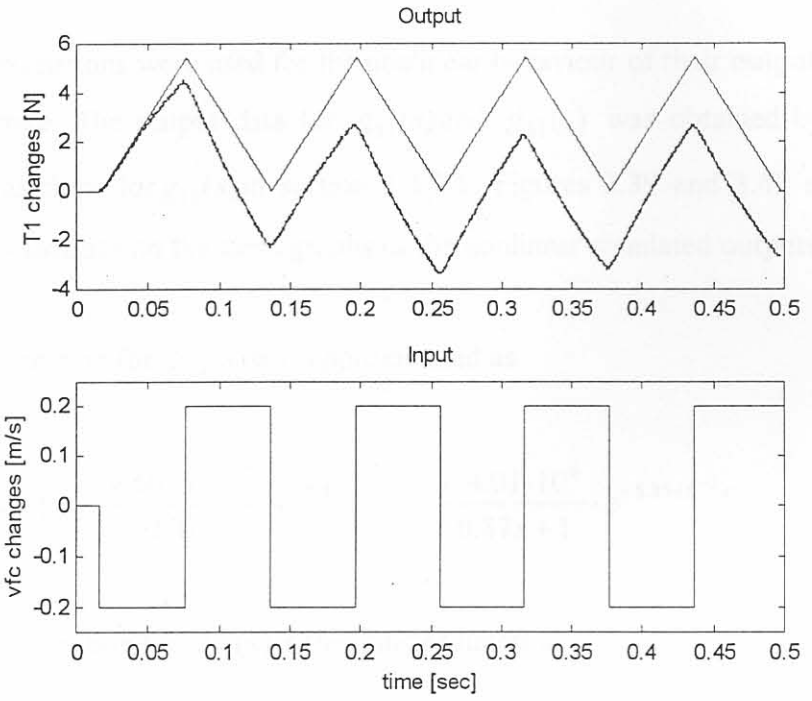

Figure 3.37: I/O data for the identification of $g_{23}(s)$ in the third linear model. (for outputs: upper curve: model output, lower curve: measured output).

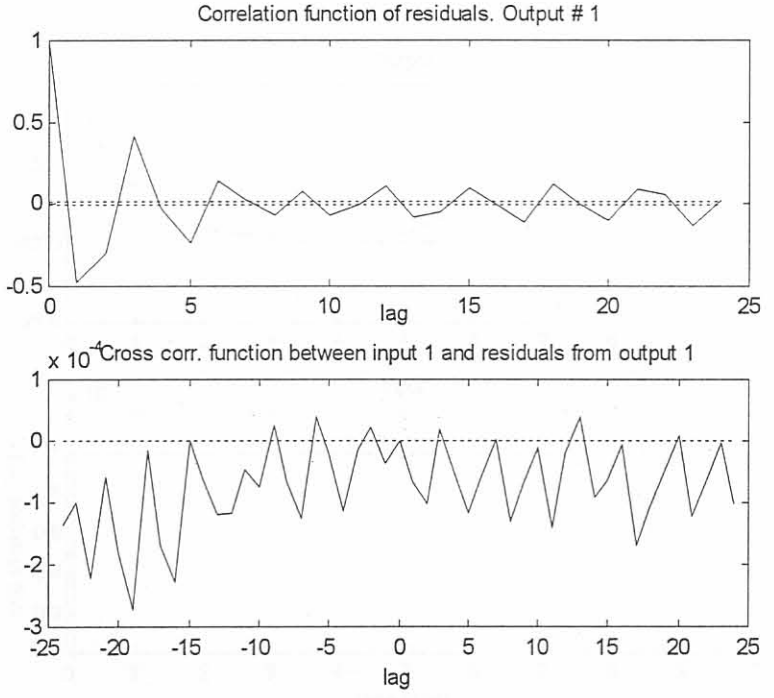

Figure 3.38: Correlation and cross correlation plot of the fitted model for $g_{23}(s)$ in the third linear model. The dotted lines indicate the 99% confidence level.

3.4.3.4 Transfer Functions $g_{21}(s)$ and $g_{31}(s)$

Linear approximations were used for the nonlinear behaviour of their output responses to a hydraulic stroke. The output data for $g_{21}(s)$ and $g_{31}(s)$ was obtained by a subtraction similar as was done for $g_{11}(s)$ in section 3.4.2.1. Figures 3.39 and 3.40 show the linear model approximations on the same graphs as the nonlinear simulated outputs.

The transfer function for $g_{21}(s)$ was approximated as

$$g_{21}(s) = \frac{-4.6035 \cdot 10^6}{s+1.1481} \cdot e^{-5.85 \cdot 10^{-3} s} = \frac{-4.01 \cdot 10^6}{0.87s+1} \cdot e^{-5.85 \cdot 10^{-3} s} \quad . \tag{3.28}$$

A linear approximation for $g_{31}(s)$ is the transfer function

$$g_{31}(s) = \frac{-1.1928 \cdot 10^6}{s+1.1763} \cdot e^{-5.85 \cdot 10^{-3} s} = \frac{-1.014 \cdot 10^6}{0.85s+1} \cdot e^{-5.85 \cdot 10^{-3} s} \quad . \tag{3.29}$$

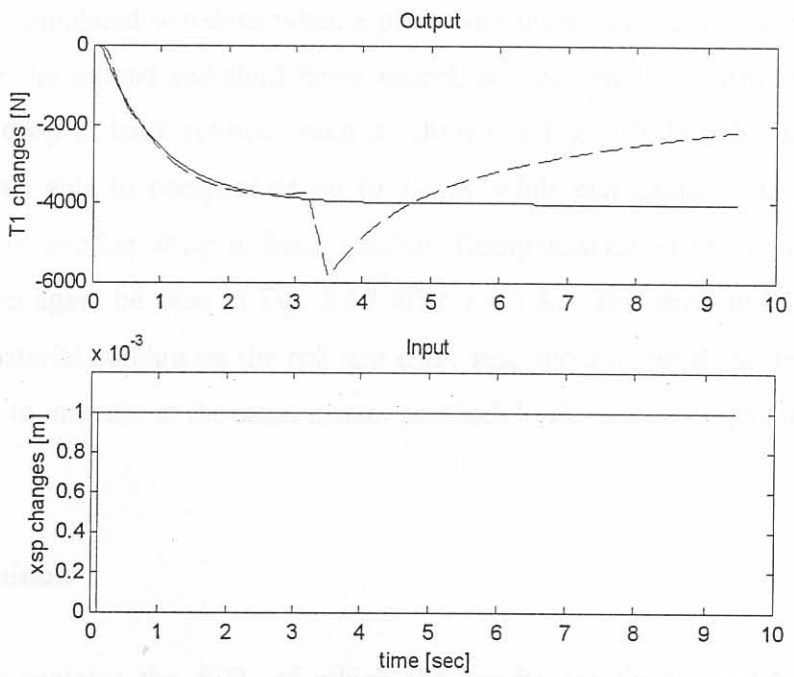

Figure 3.39: I/O data for the identification of $g_{21}(s)$ in the third linear model. (for outputs: solid: model output, dashed: measured output).

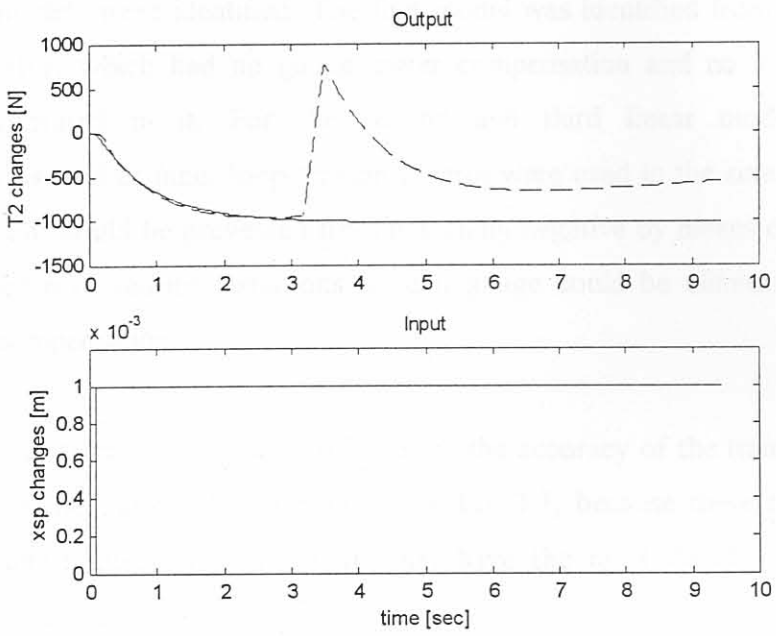

Figure 3.40: I/O data for the identification of $g_{31}(s)$ in the third linear model (for outputs: solid: model output, dashed: measured output).

The nonlinear behaviour of $g_{21}(s)$ and $g_{31}(s)$ can be attributed to a disturbance due to exit gauge/tension interaction since the tensions are the controlled variables and the coiler speeds the manipulated variables when a plant with inner loop tension control, such as the simulator for the second and third linear model, is considered. A positive hydraulic stroke results in a drop in back tension, such as shown in Fig. 3.9, but the inner loop tension control is only able to compensate up to $t \approx 3s$ while exit gauge continues to decrease. This results in another drop in back tension. Compensation of the second back tension drop can then again be seen in Fig. 3.39 after $t \approx 3.5s$. This drop in back tension is the result of a material buildup on the roll gap entry side and a material shortage is causing the front tension to increase at the same instant at which back tension drops (see Fig. 3.40).

3.5 Conclusion

This chapter contains the SID, of which the results are linear models used to design controllers for the nonlinear plant. The data for SID purposes were obtained by running the nonlinear plant simulator at an operating point, at which the mill main drive speed was forced constant, on the speed up ramp of the mill.

Three linear models were identified. The first model was identified from simulations with a plant simulator, which had no gauge meter compensation and no inner loop tension control incorporated in it. For the second and third linear model gauge meter compensation as well as inner loop tension control were used in the simulator. The result was that tensions could be prevented from becoming negative by means of tension control and the influence of tension variations on exit gauge could be eliminated by means of gauge meter compensation.

With the SID an attempt was made to focus on the accuracy of the transfer functions on the diagonal of the transfer function matrix in Eq. 3.1, because these transfer functions relate the plant outputs to those inputs that have the most direct influence on their corresponding outputs.

CHAPTER 4

CONTROLLER DESIGN METHODS

The design methods for multi-loop as well as multivariable controllers for the LTI model of the Steckel hot rolling process are discussed in this chapter. First the design method of multi-loop PID and PI control of the plant is given. The design methodology of a multivariable controller is discussed in the second part of this chapter. As a multivariable control method an H_∞ controller was used.

4.1 PID/PI Controllers

4.1.1 Introduction

The application of SISO-PID/PI control to close the loop around the transfer functions on the diagonal of the transfer function matrix of the linear model in Eq. 3.1 was considered as an option for a controller. This was done because the inputs to these transfer functions have a more direct influence on the corresponding output than the other input variables of the MIMO model have on the same outputs. This is apparent from the simulations for SID purposes in chapter 3. The transfer functions on the diagonal of the linear model in section 3.4.1 are of two different forms. A PID synthesis using an affine parameterization was chosen to design the SISO controller for the transfer function $g_{11}(s)$ in the first LTI model. For the transfer functions $g_{22}(s)$ and $g_{33}(s)$ PI synthesis by using pole assignment was applied to design SISO controllers. In subsections of 4.1 these methods are briefly discussed.

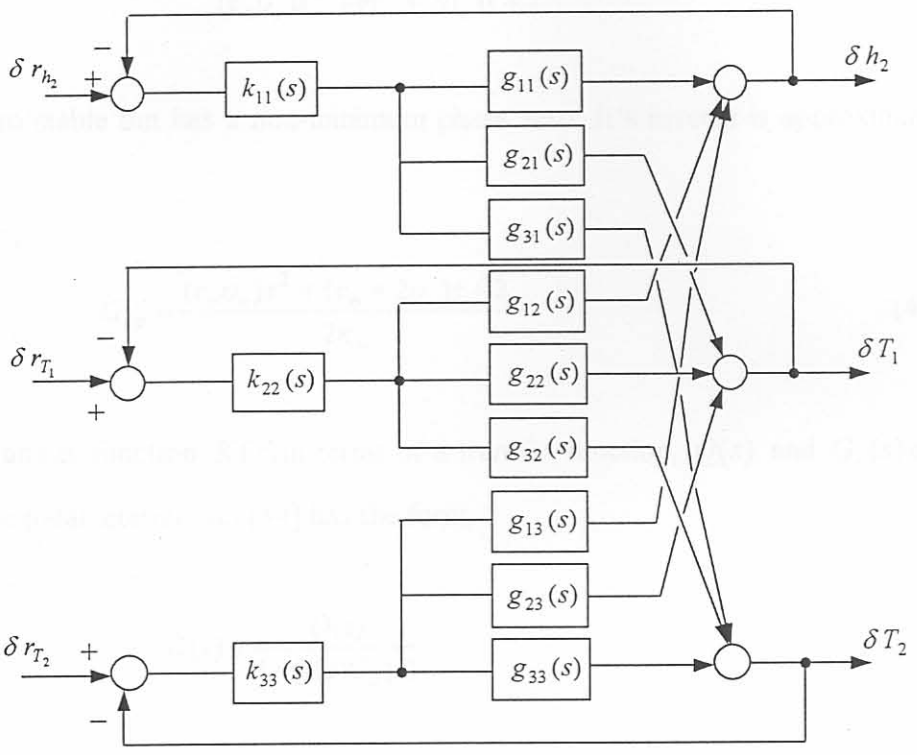

Figure 4.1: Blockdiagram for diagonal PID/PI control.

4.1.2 Controller Design Method for $g_{11}(s)$

4.1.2.1 Controller for Step Input

The time delay of $g_{11}(s)$ was replaced by a first order Pade approximation, given by,

$$e^{-s\tau_o} \approx \frac{2-s\tau_o}{2+s\tau_o} . \tag{4.1}$$

With this approximation the transfer function $g_{11}(s)$ which is of the form,

$$g_{11}(s) = G_o(s) = \frac{\kappa_o e^{-s\tau_o}}{\upsilon_o s+1} , \tag{4.2}$$

became

$$G_o \approx G_{op}(s) \equiv \frac{(-\tau_o \kappa_o)s + 2\kappa_o}{(\tau_o \upsilon_o)s^2 + (\tau_o + 2\upsilon_o)s + 2}. \tag{4.3}$$

This model is also stable but has a non-minimum phase zero. It's inverse is approximated by,

$$G_{op}^{i} = \frac{(\tau_o \upsilon_o)s^2 + (\tau_o + 2\upsilon_o)s + 2}{2\kappa_o}. \tag{4.4}$$

The controller transfer function $K(s)$ in terms of a transfer function, $Q(s)$ and $G_o(s)$ and based on an affine parameterization [34] has the form,

$$K(s) = \frac{Q(s)}{1 - Q(s)G_o(s)}. \tag{4.5}$$

With $Q(s)$ biproper an F_Q with relative degree 2 is chosen as,

$$F_Q = \frac{1}{\alpha_2 s^2 + \alpha_1 s + 1}. \tag{4.6}$$

The unity feedback controller then results as,

$$K_p(s) = \frac{Q(s)}{1 - Q(s)G_{op}(s)} = \frac{F_Q(s)G_{op}^{i}(s)}{1 - F_Q(s)G_{op}^{i}(s)G_{op}(s)} = \frac{(\tau_o \upsilon_o)s^2 + (\tau_o + 2\upsilon_o)s + 2}{(2\kappa_o \alpha_2)s^2 + (2\kappa_o \alpha_1 + \tau_o \kappa_o)s}. \tag{4.7}$$

For the PID controller of the form,

$$K_{PID}(s) = \kappa_p + \frac{\kappa_i}{s} + \frac{\kappa_d s}{\tau_d s + 1}, \tag{4.8}$$

the PID controller parameters become:

$$\kappa_p = \frac{2\tau_o \alpha_1 + 4\upsilon_o \alpha_1 + \tau_o^2 + 2\tau_o \upsilon_o - 4\alpha_2}{4\kappa_o \alpha_1^2 + 4\kappa_o \alpha_1 \tau_o + \tau_o^2 \kappa_o}, \tag{4.9}$$

$$\kappa_i = \frac{2}{2\kappa_o\alpha_1 + \tau_o\kappa_o}, \tag{4.10}$$

$$\kappa_d = \frac{(2\kappa_o\alpha_1 + \tau_o\kappa_o)^2(\tau_o\upsilon_o) - (2\kappa_o\alpha_2)(2\kappa_o\alpha_1 + \tau_o\kappa_o)(\tau_o + 2\upsilon_o) + 8\kappa_o^2\alpha_2^2}{(2\kappa_o\alpha_1 + \tau_o\kappa_o)^3}, \tag{4.11}$$

$$\tau_d = \frac{2\alpha_2}{2\alpha_1 + \tau_o}. \tag{4.12}$$

4.1.2.2 Compensator for Ramp Input

A compensator connected in series with the PID controller $K(s)$, as can be seen from Fig.4.2, was used to make the control system a type 2 system which is able to give a zero steady state error on the output for a ramp input. The purpose of the fast zero in the compensator is to draw the additional root locus branch, which is caused by the pole at $s = 0$, into the stable left half s-plane (LHP).

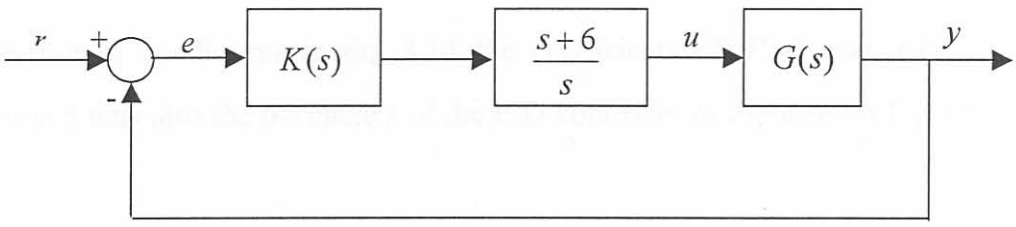

Figure 4.2: SISO feedback configuration with compensator.

4.1.3 Controller Design Method for $g_{22}(s)$ and $g_{33}(s)$

A SISO pole assignment technique, based on a polynomial approach [34], was used to find the PI controller parameters for the controllers for $g_{22}(s)$ and $g_{33}(s)$.

If the controller and model transfer functions are respectively,

$$K(s) = \frac{P(s)}{L(s)} \qquad \text{and} \qquad G_o(s) = \frac{B_o(s)}{A_o(s)}, \tag{4.13}$$

then for the PI synthesis of this approach $A_{cl}(s)$ can be an arbitrary (chosen) polynomial of degree $n_c = 2n-1$ and the polynomials $P(s)$ and $L(s)$, with degrees $n_p = n_l = n$, such that,

$$A_o(s)L(s) + B_o(s)P(s) = A_{cl}(s). \tag{4.14}$$

$A_{cl}(s)$ is a polynomial, of which the roots represent the closed loop poles. More on the choice of the closed loop poles is said in chapter 5 where the controller design is discussed.

For the PI synthesis the polynomials $P(s)$ and $L(s)$ were chosen as,

$$P(s) = p_1 s + p_0, \tag{4.15}$$

$$\overline{L}(s) = l_1 s + l_0, \tag{4.16}$$

$$L(s) = s\overline{L}(s). \tag{4.17}$$

By comparison of coefficients in Eq. 4.14 the coefficients of $P(s)$ and $\overline{L}(s)$ can be determined and thus also the parameters of the PID controller of the form in Eq. 4.8 such that,

$$\kappa_p = \frac{p_1 l_0 - p_0 l_1}{l_0^2}, \tag{4.18}$$

$$\kappa_i = \frac{p_0}{l_0}, \tag{4.19}$$

$$\kappa_d = \frac{-p_1 l_0 l_1 + p_0 l_1^2}{l_0^3}, \tag{4.20}$$

$$\tau_d = \frac{l_1}{l_0}. \tag{4.21}$$

For the PID controller of the form

$$K_{PID}(s) = \kappa_c \left(\frac{\tau_I s + 1}{\tau_I s} \right) \left(\frac{\tau_D s + 1}{\alpha \tau_D s + 1} \right), \tag{4.22}$$

the parameters in terms of the polynomial coefficients of $P(s)$ and $\overline{L}(s)$ become

$$\kappa_c = \frac{p_o}{l_o},\ \tau_I = 1,\ \tau_D = 0 \text{ and } \alpha = \infty$$

thus a PI controller of the form

$$K_{PI}(s) = \kappa_c \left(\frac{\tau_I s + 1}{\tau_I s} \right) \tag{4.23}$$

results.

4.2 H_∞ Controller

4.2.1 The H_∞ Control Problem

Since a MIMO control method is discussed in this section, small letters and large letters used in the figures here denote vectors and matrices respectively. The H_∞ controller design method, used to compute a multivariable controller, is confined to the H_∞ space. The norm of the space, H_∞, is defined as,

$$\|G\|_\infty := \sup_{\omega \in \Re} \overline{\sigma}(G(j\omega)), \tag{4.24}$$

i.e. the least upper bound of G [28].

When computing an admissible controller, $K(s)$, the H_∞ space norm of the closed loop transfer function $H_{\tilde{y}_1 \tilde{u}_1}$ (see Fig. 4.3) has to be minimized such that, given $\gamma > 0$,

where $\bar{\sigma}$ denotes the maximum singular value, ω_c the crossover frequency and S and C, the sensitivity and complementary sensitivity functions of the standard feedback configuration without weights (Fig. 4.5) respectively .

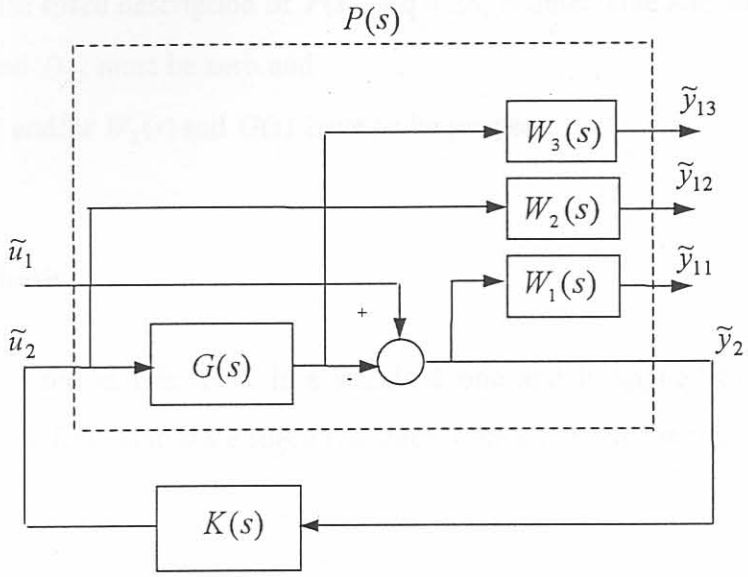

Figure 4.4: Standard feedback configuration with weights.

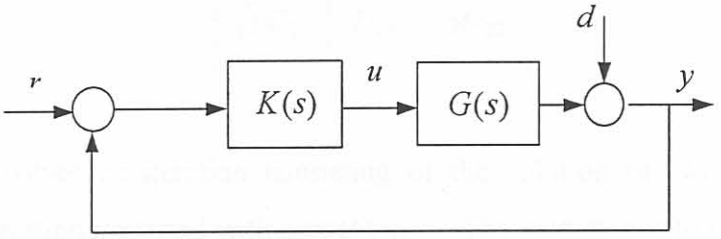

Figure 4.5: Standard feedback configuration

In Fig. 4.4 $\tilde{u}_1 = u$ is the exogenous input vector and $\tilde{y}_{13} = y$ is the output vector. Let plant $P(s)$ be given in its state space realization as

$$P(s) := \left[\begin{array}{c|cc} A & B_1 & B_2 \\ \hline C_1 & D_{11} & D_{12} \\ C_2 & D_{21} & D_{22} \end{array}\right] \tag{4.28}$$

$$\left\| H_{\tilde{y}_1\tilde{u}_1} \right\|_\infty \leq \gamma \tag{4.25}$$

with

$$\min_{K(s)} \left\| H_{\tilde{y}_1\tilde{u}_1} \right\|_\infty = \gamma_{optimal} \quad \text{with } \gamma_{optimal} < \gamma$$

The fixed parameter type controller obtained will thus be sub-optimal.

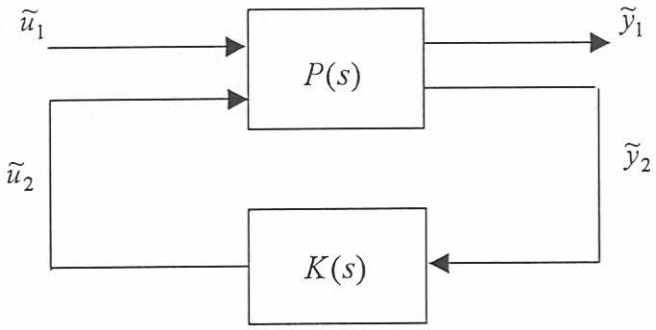

Figure 4.3: Synthesis block diagram

4.2.2 Weights for Plant Augmentation

As shown in Fig. 4.4 plant $G(s)$ was in this problem augmented by weighting functions $W_i(s) = c_i(s) \cdot I_{n\times n}$ $(i = 1,2,3)$ to form plant $P(s)$. Two bounds were taken into account when selecting weights: The performance bound given by

$$\bar{\sigma}[S(j\omega)] \leq \bar{\sigma}[W_1^{-1}(j\omega)] , \qquad \omega < \omega_c \tag{4.26}$$

and the robustness bound given by

$$\bar{\sigma}[C(j\omega)] \leq \bar{\sigma}[W_3^{-1}(j\omega)] , \qquad \omega > \omega_c \tag{4.27}$$

To be able to apply the H_∞ synthesis successfully, $P(s)$ must have the following properties:

i) the state space description of $P(s)$, Eq.4.28, is detectable and stabilizable,

ii) D_{11} and D_{22} must be zero and

iii) $W_2(s)$ and/or $W_3(s)$ and $G(s)$ have to be proper.

4.2.3 H_∞ Synthesis

The H_∞ synthesis used in this work is a standard one and is applied to the augmented plant, $P(s)$, with the following state space realization scaled by the iteration parameter, γ:

$$\tilde{P}(s) = \left[\begin{array}{c|cc} A & \frac{1}{\sqrt{\gamma}}B_1 & \sqrt{\gamma}B_2 \\ \hline \frac{1}{\sqrt{\gamma}}C_1 & \frac{1}{\gamma}D_{11} & D_{12} \\ \sqrt{\gamma}C_2 & D_{21} & \gamma D_{22} \end{array}\right] \tag{4.29}$$

The synthesis involves an iteration consisting of the solution of two modified Riccati equations. The iteration is started with a guess in γ. The next step is to determine X_∞ and Y_∞, denoting the unique, real, symmetric solutions of the following two algebraic Riccati equations (ARE).

For X_∞ the ARE is:

$$(A - B_2 D_{12}^T C_1)^T X_\infty + X_\infty (A - B_2 D_{12}^T C_1) - X_\infty (B_2 B_2^T - B_1 B_1^T) X_\infty + \tilde{C}_1^T \tilde{C}_1 = 0 \tag{4.30}$$

with

$$\tilde{C}_1 = (I - D_{12} D_{12}^T) C_1 \ .$$

For Y_∞ the ARE is:

$$(A - B_1 D_{21}^T C_2)Y_\infty + Y_\infty (A - B_1 D_{21}^T C_2)^T - Y_\infty (C_2 C_2^T - C_1 C_1^T)Y_\infty + \tilde{B}_1^T \tilde{B}_1 = 0, \qquad (4.31)$$

with

$$\tilde{B}_1 = B_1 (I - D_{21}^T D_{21}).$$

The parameter γ is increased stepwise for every iteration until the ARE solutions are positive semi-definite, i.e.

$$X_\infty \geq 0 \ , Y_\infty \geq 0 \text{ and } \bar{\lambda}(Y_\infty X_\infty) \leq 1$$

where $\bar{\lambda}$ denotes the maximum eigenvalue.

The controller finally obtained in its state space description is

$$\hat{K}(s) = \left[\begin{array}{c|c} A - K_F C_2 - B_2 K_C + Y_\infty C_1^T (C_1 - D_{12} K_C) & K_F \\ \hline K_C & 0 \end{array}\right]$$

where

$$K_F = (Y_\infty C_2^T + B_1 D_{12}^T),$$

$$K_C = (B_2^T X_\infty + D_{12}^T C_1)(I - Y_\infty X_\infty)^{-1}.$$

CHAPTER 5

CONTROLLER DESIGNS

5.1 Introduction

For the design of the diagonal controllers Bode and root locus plots as well as time domain simulations served as an indication of controller performance. In the design of the H_∞ controllers singular value plots of the sensitivity and complementary sensitivity transfer function together with singular value plots of the performance and robustness bounds respectively, are used as an indication of the performance of the H_∞ controllers. In addition to frequency domain plots, closed-loop time domain simulations were used as a check on the H_∞ controller behaviour. This chapter also gives some necessary specifications of the controller as well as the values that were used for their tuning parameters. Starting with the specifications in section 5.2, a brief discussion of the diagonal controllers design follows in section 5.3. In sections 5.4 and 5.5 the H_∞ controller designs for the LTI models in sections 3.4.2 and 3.4.3 respectively are given. Lastly in section 5.6 a comparison of the diagonal and H_∞ controllers is done by means of singular value plots of their closed loop transfer functions and also by means of time domain simulations.

5.2 Controller Specifications

Controller specifications are given in terms of the following requirements:

i) Exit gauge is to be kept within 1% of its setup value in the presence of control error changes [41].

ii) Front and back tensions are to be kept within 40% of their setup values [41].

iii) Control actions are to be kept within realistic limits, i.e. $|x_{sp}| = |u_1| \leq 6.5 \cdot 10^{-3}$ m, $|\dot{v}_{bc}| = |\dot{u}_2| \leq 21$ m/s^2 and $|\dot{v}_{fc}| = |\dot{u}_2| \leq 120$ m/s^2 (see App.B).

iv) Nominal stability is to be guaranteed.

5.3 Diagonal Controller Design

The parameters of the diagonal controller $K_{diag}(s)$,

$$K_{diag}(s) = \begin{bmatrix} k_{11}(s) & 0 & 0 \\ 0 & k_{22}(s) & 0 \\ 0 & 0 & k_{33}(s) \end{bmatrix} \tag{5.1}$$

were obtained by using the methods described in section 4.1.

The main reason for the design of a diagonal controller is to try the simplest controller first. Furthermore two arguments have relevance in the decision on a diagonal controller design. The first one is that for the maximum step sizes of coiler speed and actuator stroke, the influence of the coiler speed step on strip exit gauge is by two orders of magnitude smaller than that of the direct input, hydraulic actuator stroke. Another argument, which supported the choice for a diagonal controller scheme is that the frequency of the variations on the plant output, exit gauge, is less than its SISO closed-loop bandwidth. These variations in exit gauge are a result of tension variations and can be regarded as disturbances because of their frequency being lower than the corresponding closed-loop bandwidth. The bandwidths of the transfer functions on the diagonal of the first linear model in closed loop with their corresponding controllers can be obtained from the Bode plots in figures 5.1 through 5.3 at the frequency where the log magnitude curve crosses the –3 decibel line. The frequency of the gauge/tension interaction is approximately 1.34 rad/s, which is lower than the bandwidths of these transfer functions on the diagonal in closed loop with their controllers.

Table 5.1: Closed loop bandwidths of transfer functions on the diagonal

Transfer function	Closed loop bandwidth [rad/s]
$g_{11}(s)$	2
$g_{22}(s)$	90
$g_{33}(s)$	90

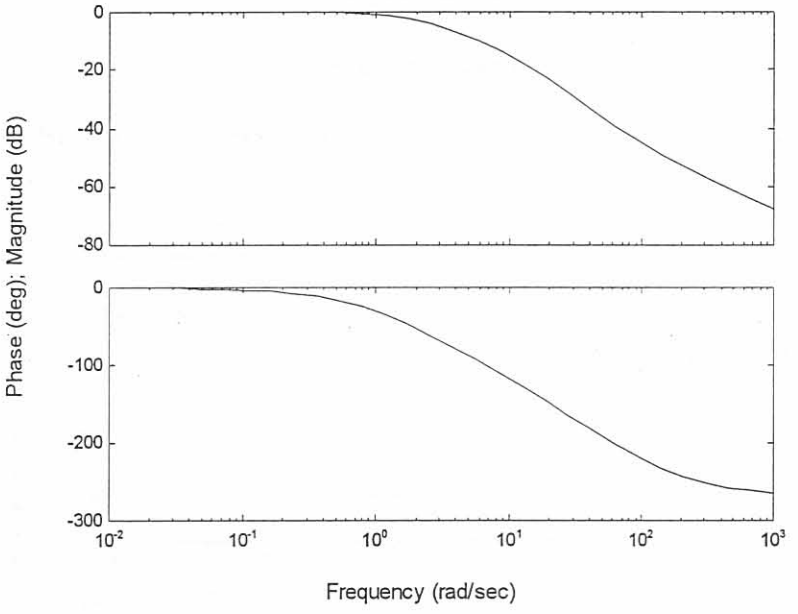

Figure 5.1: Bode plot of $g_{11}(s)$ of first linear model in closed loop with PID control.

The PID controller $k_{11}(s)$ was designed as SISO controller for the plant represented by the transfer function Eq. 3.4. The tuning parameters obtained for this design were $\alpha_1 = 0.55$ and $\alpha_2 = 0.03$. Speed of response of the closed loop had to be traded off against control action changes, which needed to be within realistic limits. Overshoot and bandwidth of this SISO system can be influenced by adjusting only α_1 and α_2, since the PID gains (equations 4.9 through 4.11) are given directly in terms of the model parameters in Eq. 4.2 and the design filter in Eq. 4.6 [34].

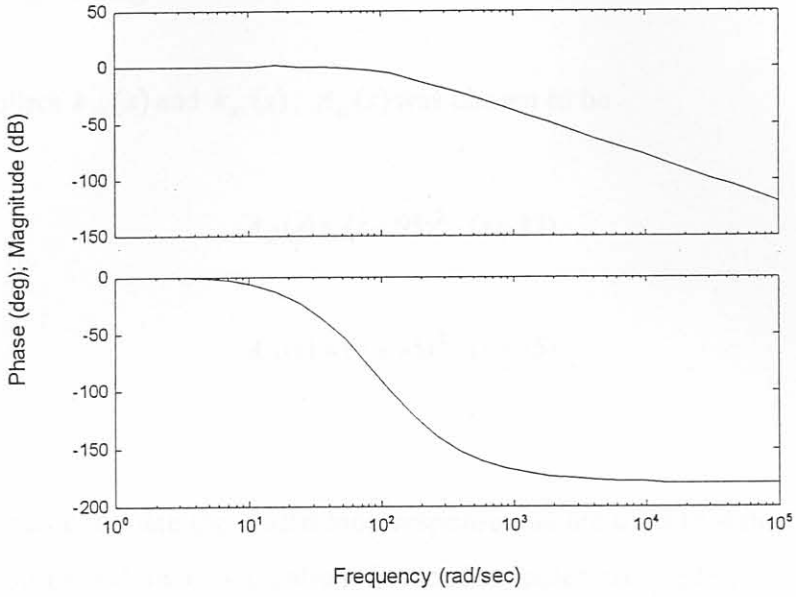

Figure 5.2: Bode plot of $g_{22}(s)$ of first linear model in closed loop with PI control.

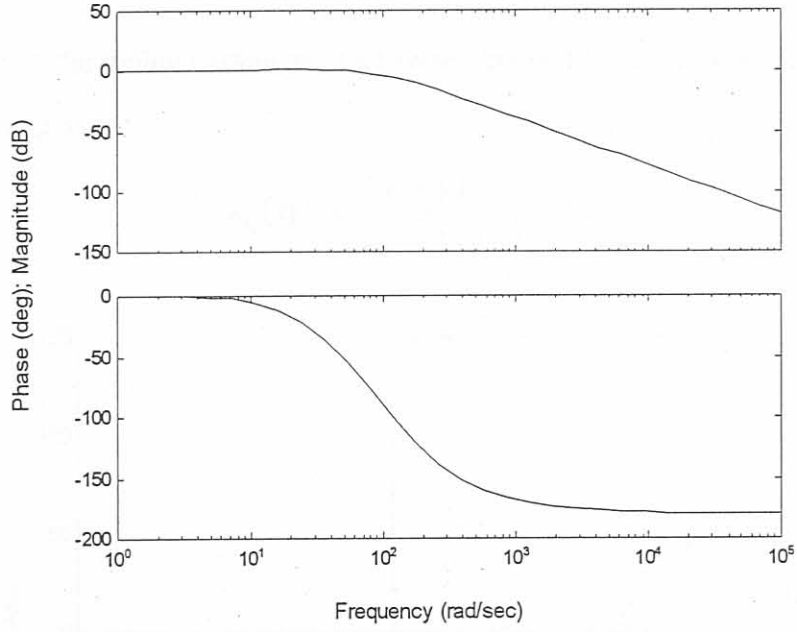

Figure 5.3: Bode plot of $g_{33}(s)$ of first linear model in closed loop with PI control.

PI control is used for $k_{22}(s)$ and $k_{33}(s)$, because it is a popular controller [36]. Integral control on its own would result in persistent oscillation. However some damping is produced with the addition of proportional control. By means of the chosen design method, pole placement design, proper tuning is available and oscillations that can accompany the use of PI controllers [36] are avoided. The root locus plots figures 5.4 and

5.5 indicate the tendency of the closed loops with PI controllers to oscillate with two branches leaving the negative real axis.

For PI controllers $k_{22}(s)$ and $k_{33}(s)$, $A_{cl}(s)$ was chosen to be

$$A_{cl}(s) = (s+95)^2 \cdot (s+12) \tag{5.3}$$

and

$$A_{cl}(s) = (s+95)^2 \cdot (s+15) \tag{5.4}$$

respectively.

The slower poles dominate the closed loop response and are used to influence overshoot in the closed loop time domain simulation. If the slow poles are made less negative it helps to reduce overshoot. The purpose of the fast poles, in $A_{cl}(s)$, is to give a fast response, i.e. a large bandwidth, of the closed SISO loops.

Table 5.2 shows the tuning parameters that were obtained for controllers $k_{22}(s)$ and $k_{33}(s)$ with the meaning as in

$$k_{ii}(s) = \kappa_c \left(\frac{\tau_I s + 1}{\tau_I s} \right) \quad , \; i \in [2,3] \tag{5.5}$$

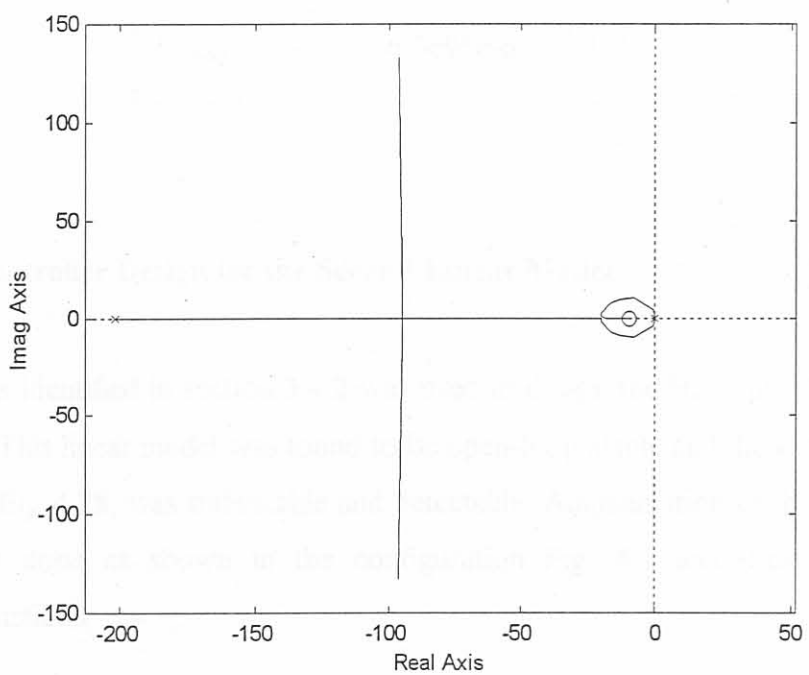

Figure 5.4: Root locus of $g_{22}(s)$ of first linear model in closed loop with PI control.

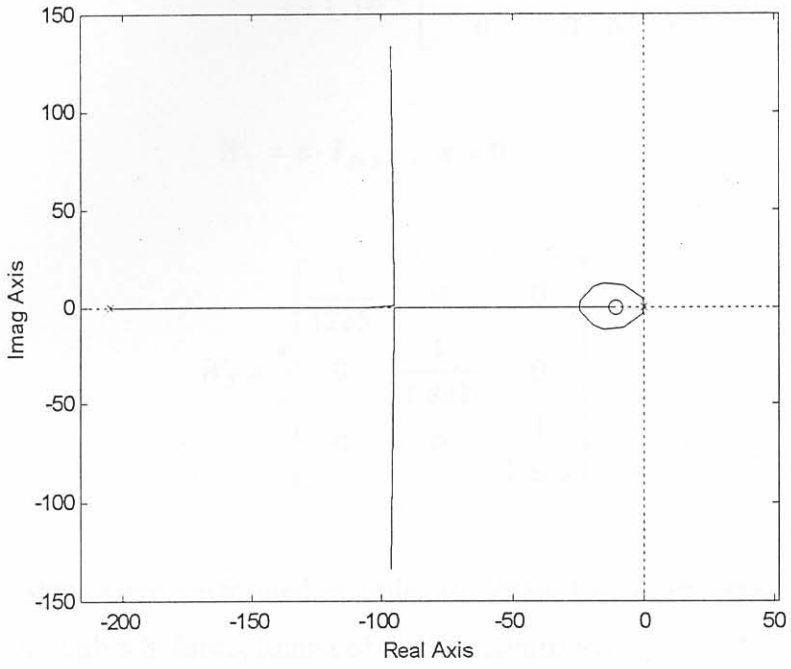

Figure 5.5: Root locus of $g_{33}(s)$ of first linear model in closed loop with PI control.

Table 5.2: Tuning parameters for $k_{22}(s)$ and $k_{33}(s)$

Controller	κ_c	τ_I
$k_{22}(s)$	-3.7129e-6	1.0
$k_{33}(s)$	6.0695e-6	1.0

5.4 H_∞ Controller Design for the Second Linear Model

The model as identified in section 3.4.2 was used to design the H_∞ controller discussed in this section. This linear model was found to be open-loop stable and therefore the plant, as described in Eq. 4.28, was stabilizable and detectable. Augmentation of the linear plant by weights was done as shown in the configuration Fig. 4.4 and using the following weighting functions.

$$W_1 = \frac{0.2}{s+1\cdot 10^{-6}}\begin{bmatrix} 0.5e-4 & 0 & 0 \\ 0 & 6 & 0 \\ 0 & 0 & 6 \end{bmatrix} \tag{5.6}$$

$$W_2 = \varepsilon \cdot \boldsymbol{I}_{3\times 3} \quad ; \quad \varepsilon = 0 \tag{5.7}$$

$$W_3 = \frac{s}{1}\begin{bmatrix} \frac{1}{12e5} & 0 & 0 \\ 0 & \frac{1}{1.8e3} & 0 \\ 0 & 0 & \frac{1}{1.8e3} \end{bmatrix} \tag{5.8}$$

The following steps were performed in order to obtain the parameters in the weights of equations 5.6 through 5.8 during tuning of the H_∞ controller.

1. Adjust parameters in positions (2,2) and (3,3) of $W_1(s)$ in order to affect the speed of response. In this step it was found that a large difference between the values of the elements of $W_1(s)$ caused the performance bound to be violated.
2. Adjust parameter in position (1,1) of $W_3(s)$ in order to meet the performance bound specification, Eq. 4.26, if it has been violated in step 1. Decreasing of element (1,1) of $W_3(s)$ was done until control action, u_1, exceeded the limit specified in 5.2 iii).
3. If necessary, the gain of $W_1(s)$ needs to be adjusted such that the controller's performance for output y_1 is the same as that of the diagonal controller. If the performance of the controller with respect to outputs y_2 and y_3 deteriorated, steps 1 and 2 were repeated.

Figures 5.6 and 5.7 show how the closed loop meets the performance and robustness bound specifications respectively as given in equations 4.26 and 4.27.

The continuous state space matrices of the model-reduced form of this controller is given in App. C.1.

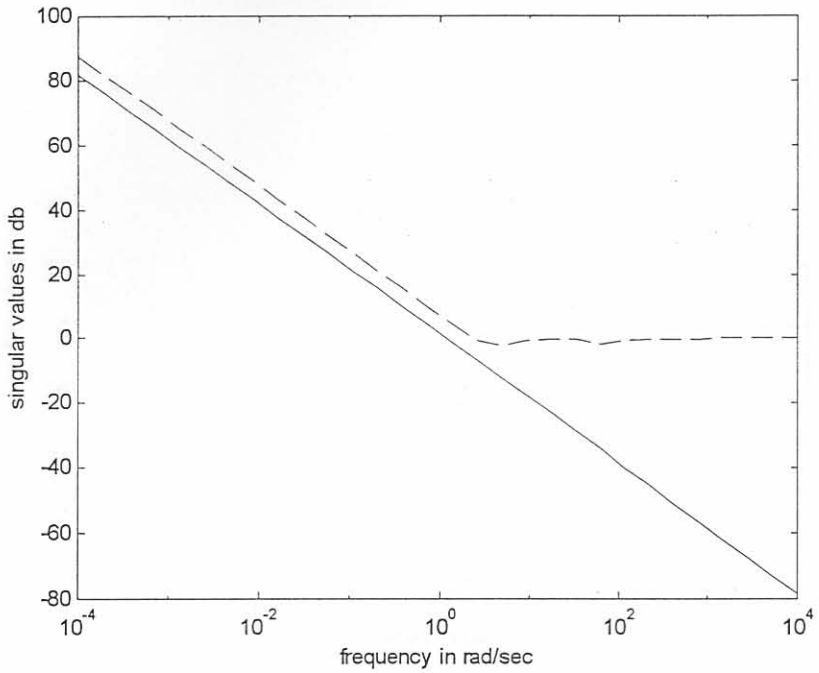

Figure 5.6: Plots of $1/\overline{\sigma}(S)$ (dashed line) and $\overline{\sigma}(W_1)$ (solid line) of second linear model in closed loop with its corresponding H_∞ controller.

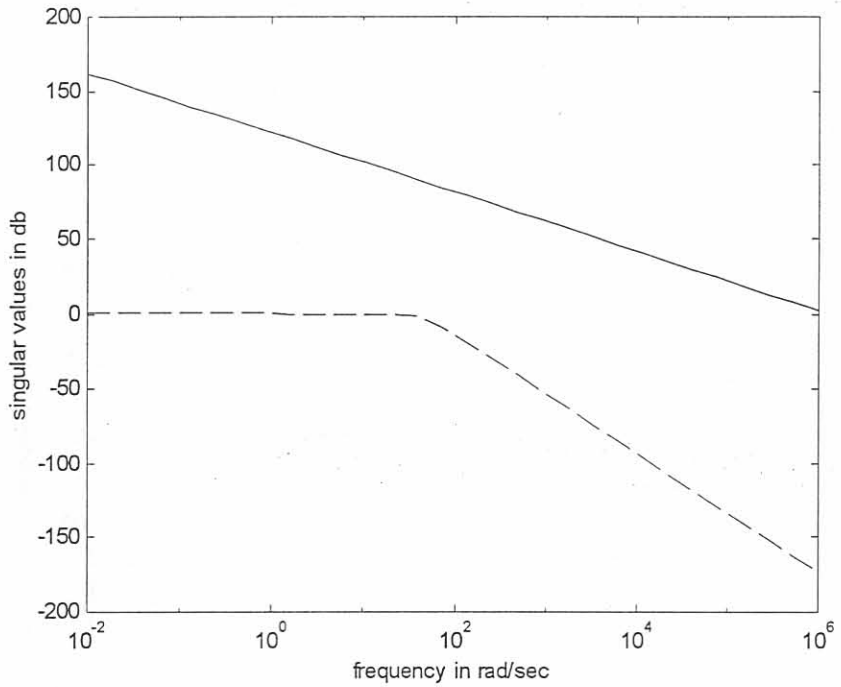

Figure 5.7: Plots of $\overline{\sigma}(T)$ (dashed line) and $\overline{\sigma}(W_3^{-1})$ (solid line) of second linear model in closed loop with its corresponding H_∞ controller.

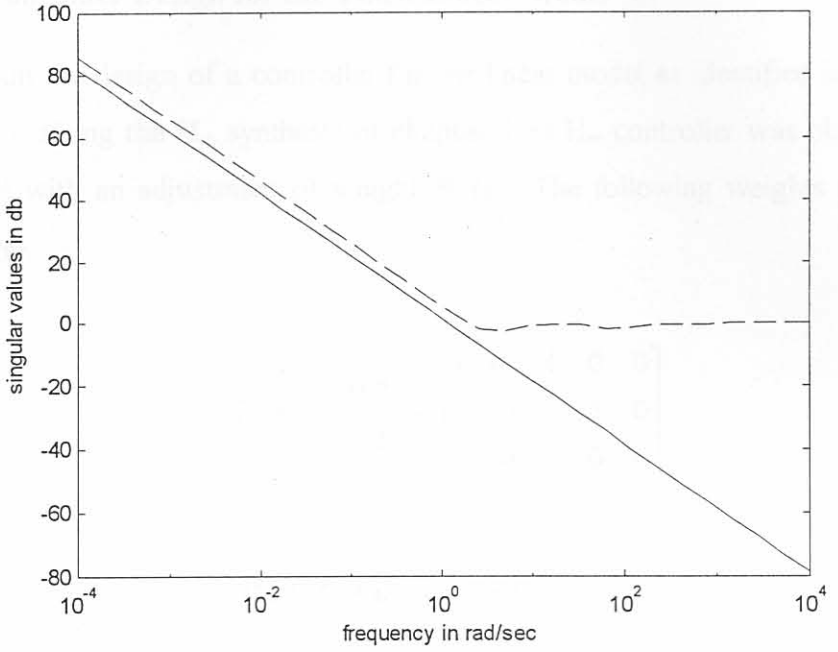

Figure 5.8: Plots of $1/\overline{\sigma}(S)$ (dashed line) and $\overline{\sigma}(W_1)$ (solid line) of third linear model in closed loop with its corresponding H_∞ controller.

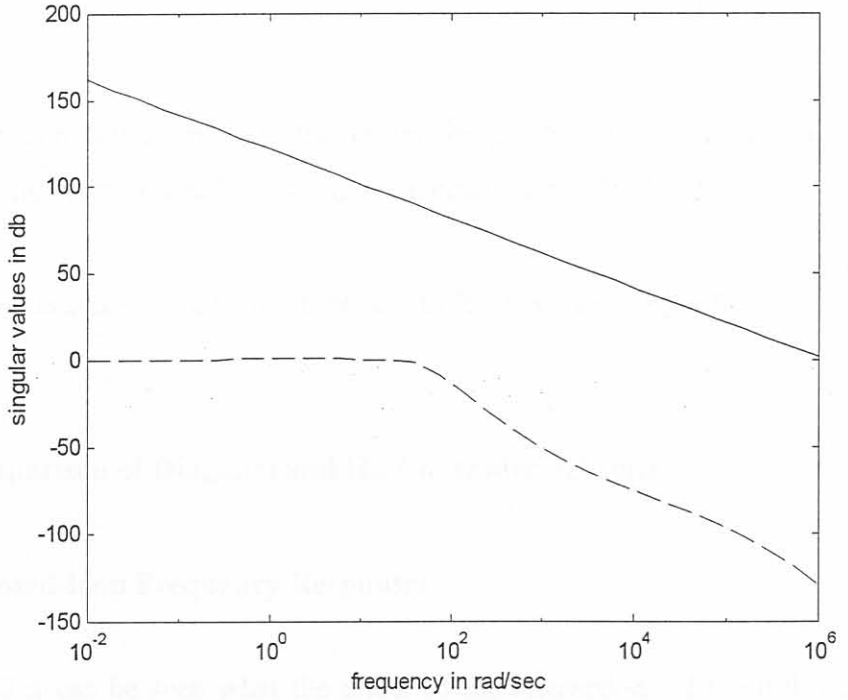

Figure 5.9: Plots of $\overline{\sigma}(T)$ (dashed line) and $\overline{\sigma}(W_3^{-1})$ (solid line) of third linear model in closed loop with its corresponding H_∞ controller.

5.5 H_∞ Controller Design for the Third Linear Model

In this section the design of a controller for the linear model as identified in section 3.4.3 is considered. Using the H_∞ synthesis of chapter 4 an H_∞ controller was obtained for this linear model with an adjustment of weight $W_1(s)$. The following weights were used for this controller.

$$W_1 = \frac{0.2}{s+1\cdot 10^{-6}}\begin{bmatrix} 0.4e-4 & 0 & 0 \\ 0 & 6 & 0 \\ 0 & 0 & 6 \end{bmatrix} \tag{5.6}$$

$$W_2 = \varepsilon \cdot I_{3\times 3} \quad ; \quad \varepsilon = 0 \tag{5.7}$$

$$W_3 = \frac{s}{1}\begin{bmatrix} \frac{1}{12e5} & 0 & 0 \\ 0 & \frac{1}{1.8e3} & 0 \\ 0 & 0 & \frac{1}{1.8e3} \end{bmatrix} \tag{5.8}$$

Figures 5.8 and 5.9 show how the closed loop meets the performance and robustness bound specifications respectively as given in equations 4.26 and 4.27.

The continuous state space form of this controller is given in App. C.2.

5.6 Comparison of Diagonal and H_∞ Controller Schemes

5.6.1 Closed-loop Frequency Responses

In Fig. 5.10 it can be seen what the effect of the interactions of the full first linear model are on the closed loop. The difference in maximum and minimum singular values of the diagonal controller in closed loop with the full first linear model is large compared to

corresponding quantities of the other two closed loop control systems. This is so because the interactions have not been accounted for in the design of the diagonal controller.

In closed loop with LTI models consisting of only the transfer functions on the diagonal, the diagonal and H_∞ controllers have a flat closed-loop frequency response for frequencies below 2 rad/s, which is desirable for good set point following and good disturbance rejection.

The effect of interactions can again be seen in Fig. 5.11, which compares the singular value plots of the closed-loop transfer function matrices of the H_∞ controllers for the second and third LTI models. The effect here is that the difference between maximum and minimum singular values becomes larger for higher frequencies.

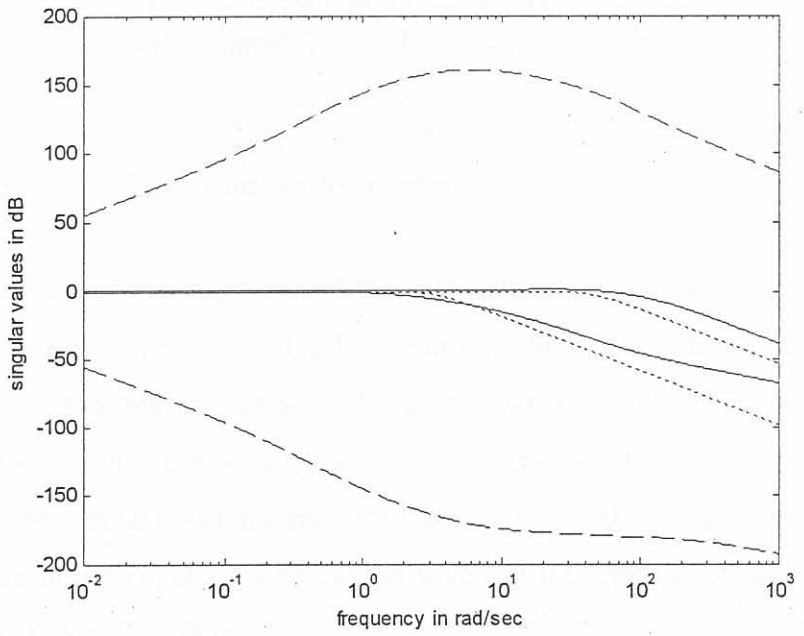

Figure 5.10: Maximum and minimum singular values of closed loop transfer functions of
i) diagonal controller with full first linear model (dashed),
ii) diagonal controller with diagonal first linear model (solid),
iii) H_∞ controller with second linear model (dotted).

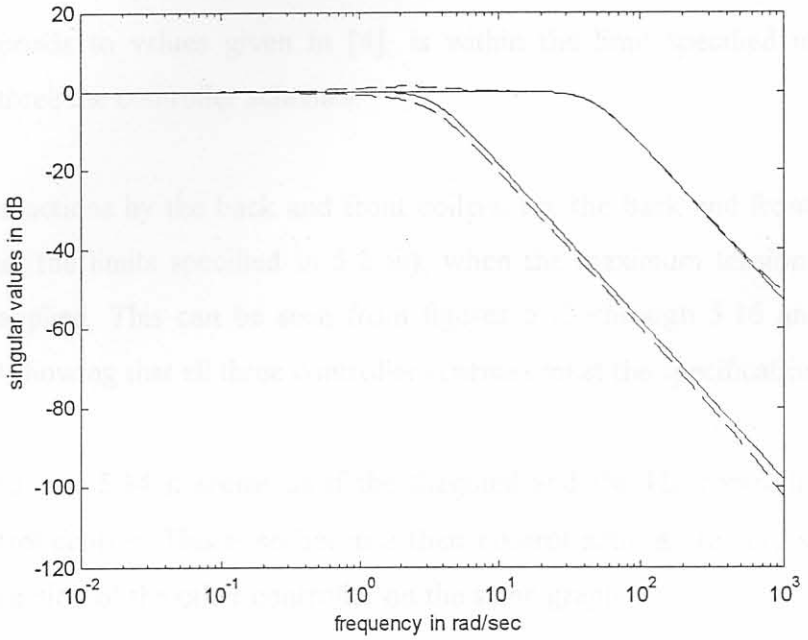

Figure 5.11: Maximum and minimum singular values of closed loop transfer functions of
i) H_∞ controller with second linear model (solid),
ii) H_∞ controller with third linear model (dashed).

5.6.2 Closed-loop Time Domain Responses

Fig. 5.12 shows that the diagonal and the H_∞ controller in closed loop with the first and second LTI model respectively have been tuned to have the same settling times for exit gauge. As shown in figures 5.13 and 5.14 the settling times for the tensions in the case of the diagonal controller scheme are 0.2 seconds longer than those of the H_∞ controller for the second linear model. For the matter of comparing both the latter controller schemes this difference in tension settling time is not severe in the light of the total settling time for exit gauge, which is 2.5 seconds.

Comparing the performance of the H_∞ controllers for the second and third LTI models no difference in settling times of the controlled variables can be found as shown in figures 5.17 through 5.19.

In the diagonal controller scheme the integrator parts of its individual controller transfer functions help to achieve specification i) and ii). So does the weight, $W_1(s)$, with its integrator characteristics in the H_∞ controllers for the second and third linear models.

The controller action, u_1, i.e. hydraulic actuator stroke, for set point changes in exit gauge, which corresponds to values given in [4], is within the limit specified in 5.2 iii). This applies to all three the controller schemes.

The controller actions by the back and front coilers, i.e. the back and front coiler speeds, are also within the limits specified in 5.2 iii), when the maximum tension step set point changes are applied. This can be seen from figures 5.13 through 5.16 and from figures 5.18 and 5.19 showing that all three controller schemes meet the specification 5.2 iii).

In figures 5.13 and 5.14 it seems as if the diagonal and the H_∞ controllers respectively apply no control actions. This is so because their control actions are very small compared to the control action of the other controller on the same graph.

The fact that for the closed loops for all three controller schemes and their corresponding LTI plant models, the poles are in the open left half s-plane shows that specification iv) is satisfied by all three systems.

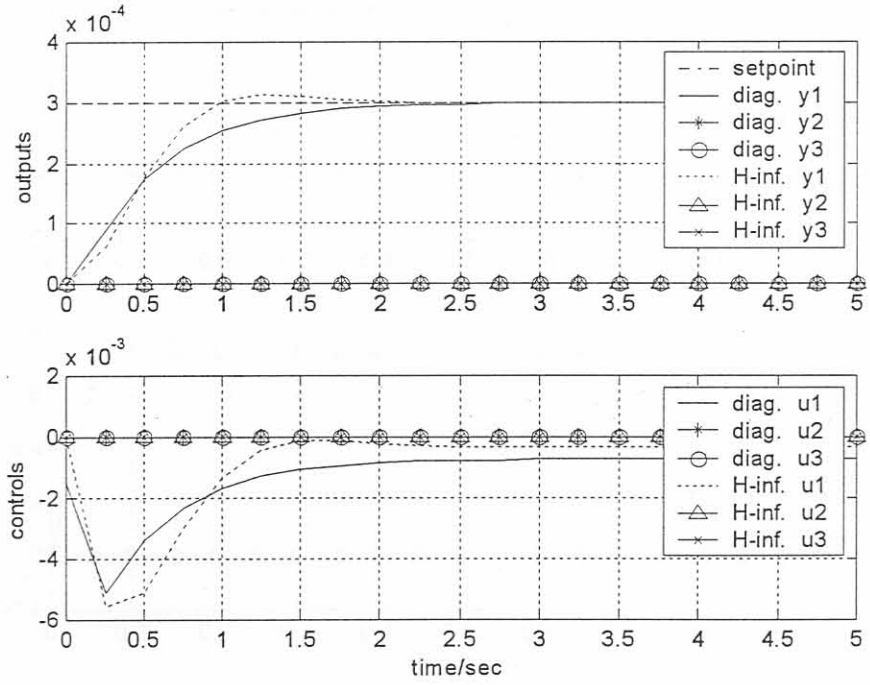

Figure 5.12: Closed loop simulation results of the diagonal controller with the diagonal first linear model and an H_∞ controller with the second linear model for the set point r = [3e-4 0 0] – (SI units apply).

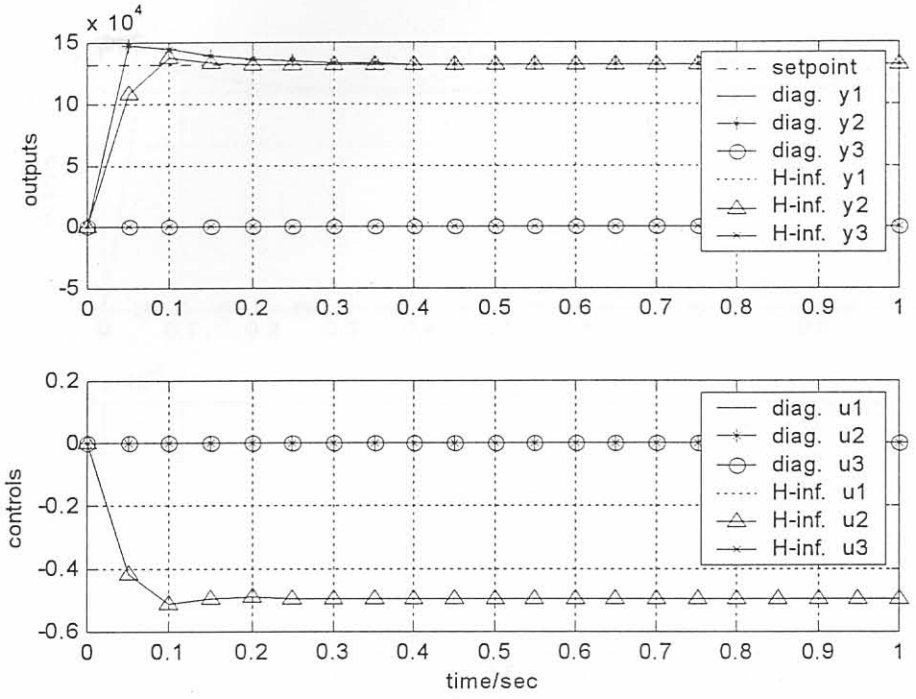

Figure 5.13: Closed loop simulation results of the diagonal controller with the diagonal first linear model and an H_∞ controller with the second linear model for the set point r = [0 1.32e5 0] – (SI units apply).

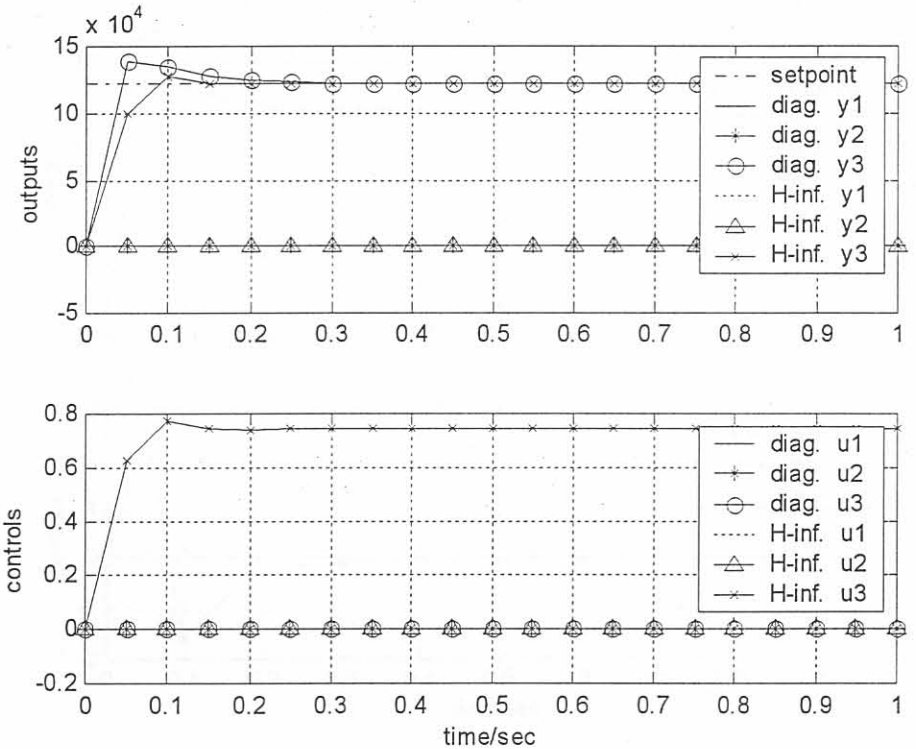

Figure 5.14: Closed loop simulation results of the diagonal controller with the diagonal first linear model and an H_∞ controller with the second linear model for the set point r = [0 0 1.22e5] – (SI units apply).

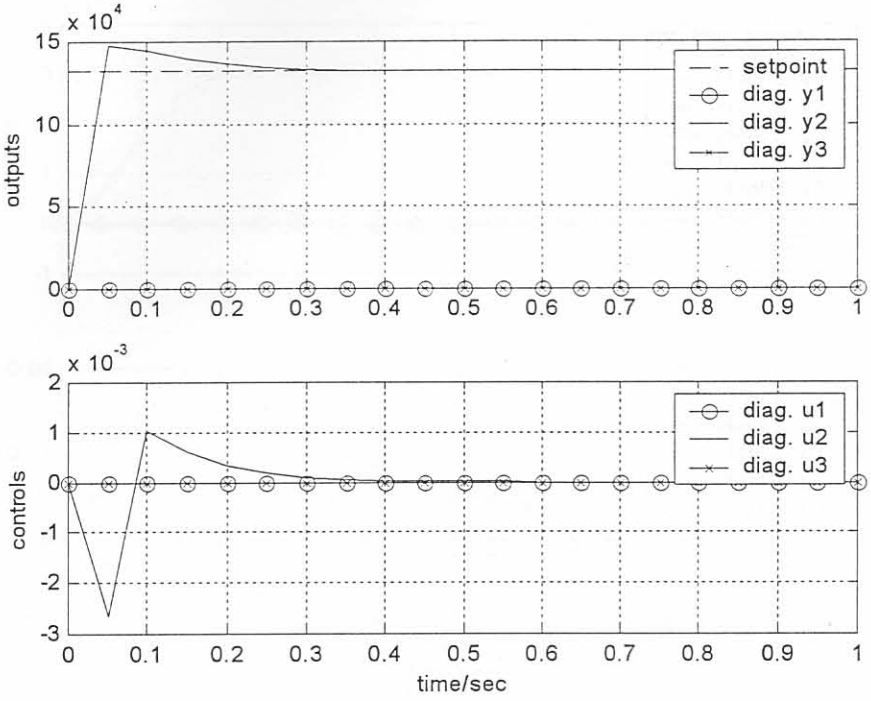

Figure 5.15: Closed loop simulation results of the diagonal controller with the diagonal first linear model for the set point r = [0 1.32e5 0] – (SI units apply).

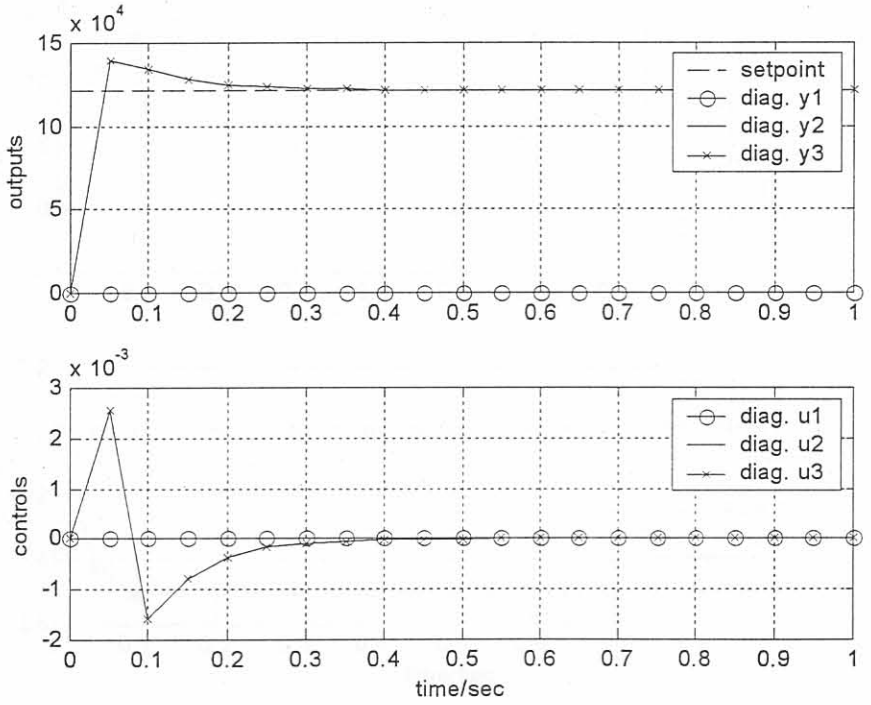

Figure 5.16: Closed loop simulation results of the diagonal controller with the diagonal first linear model for the set point r = [0 0 1.22e5] – (SI units apply).

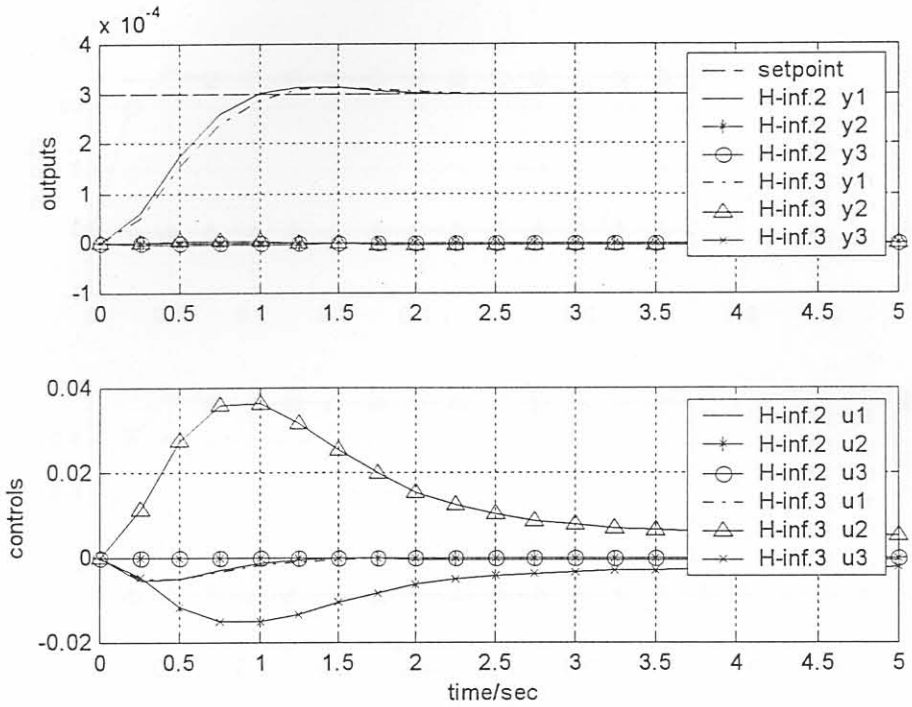

Figure 5.17: Closed loop simulation results of an H_∞ controller (H-inf.2) with the second linear model and an H_∞ controller (H-inf.3) with third linear model for the set point r = [3e-4 0 0] – (SI units apply).

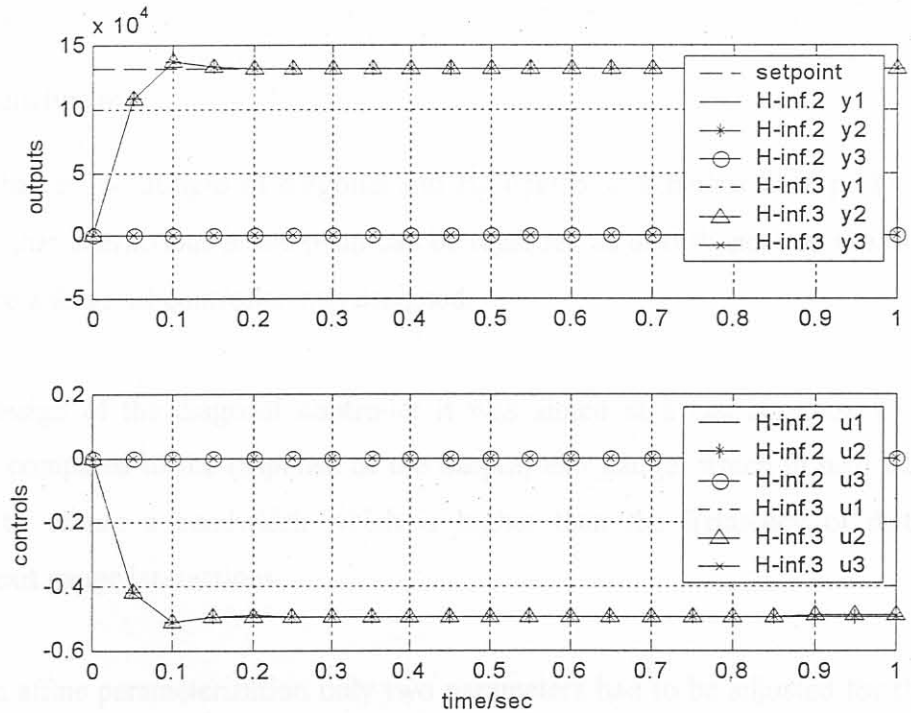

Figure 5.18: Closed loop simulation results of an H_∞ controller (H-inf.2) with the second linear model and an H_∞ controller (H-inf.3) with the third linear model for the set point r = [0 1.32e5 0] – (SI units apply).

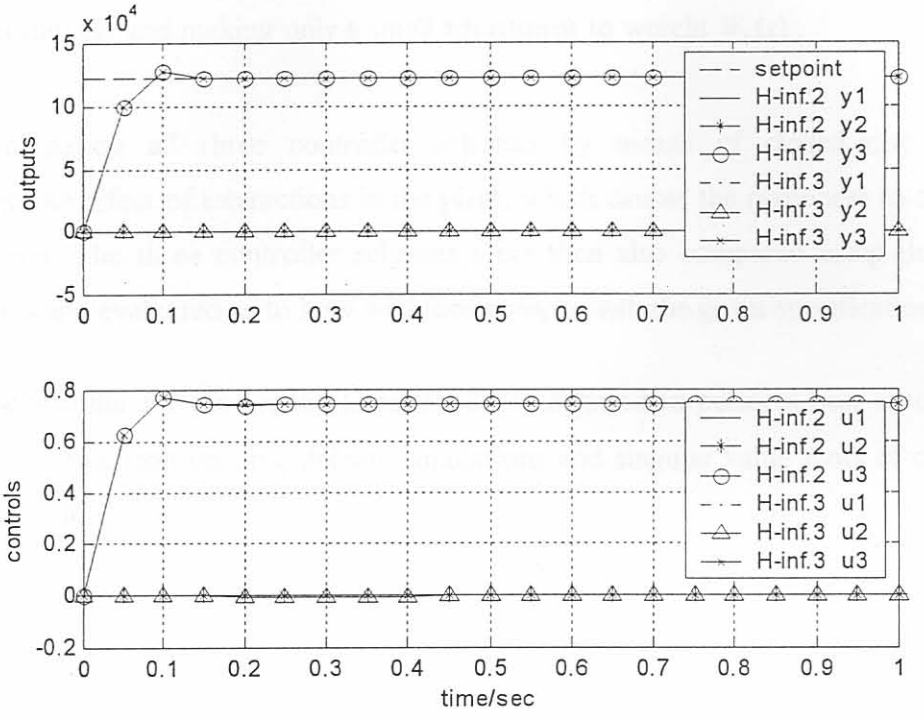

Figure 5.19: Closed loop simulation results of an H_∞ controller (H-inf.2) with the second linear model and an H_∞ controller (H-inf.3) with the third linear model for the set point r = [0 0 1.22e5] – (SI units apply).

5.7 Conclusion

In this chapter the designs of diagonal and H_∞ controller schemes were performed. It was assumed that interactions in the plant can be regarded as disturbances on the plant outputs, and hence a diagonal controller was designed.

In the design of the diagonal controller it was aimed at a fast response of the tension outputs, compared to the response of the output, exit gauge, which in turn had to be fast enough to ensure a bandwidth which is higher than the frequency of disturbance by tension/exit gauge interactions.

Using an affine parameterization only two parameters had to be adjusted for the tuning of the PID controller in the diagonal controller scheme. A desirable performance of the PI controllers in the diagonal control structure was obtained by pole placement design.

A diagonal H_∞ controller for the second linear model was designed by selecting weights on plant outputs and their errors appropriately. A second H_∞ controller was designed. This

design was based on the third linear model using the same weights as for the diagonal H_∞ controller initially and making only a small adjustment to weight $W_1(s)$.

When comparing all three controller schemes by means of closed-loop frequency responses, the effect of interactions in the plant, which causes the responses to deteriorate, can be seen. The three controller schemes were then also compared using time domain simulations and evaluated as to how well they comply with the given specifications.

The H_∞ controller for the second linear model was found to perform best according to a controller comparison on time domain simulations and singular value plots of closed loop transfer functions.

CHAPTER 6

RESULTS

6.1 Controller Implementation and Organization of Results

The three controller schemes, designed in chapter 5, were discretized first before they were implemented on the nonlinear simulator.

The discretization for the diagonal controller was done, by using the velocity form to compute the controller outputs. A model reduction was performed on the continuous state space matrices of the H_∞ controllers for the second linear model. Its number of states was reduced from 9 to 7.

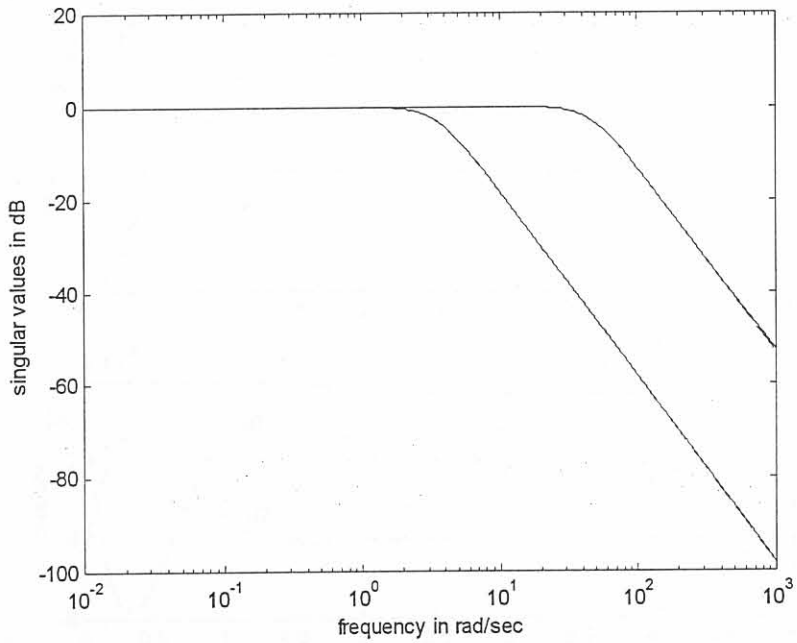

Figure 6.1: Closed-loop singular values of the H_∞ controller for the second linear model (dashed) and of the model reduced H_∞ controller for the second linear model (solid).

Fig. 6.1 compares the closed-loop singular value of the reduced to the unreduced controller. From this figure it can be seen that the singular values of the closed loops with the reduced and original controllers differ only at higher frequencies.

The time domain simulations for a set point $r = [3e-4 \quad 0 \quad 0]$ in figures 6.2 through 6.5 show a more severe interaction between the control actions and system outputs in the case of the model reduced controller. However figures 6.2 through 6.7 show that the model reduced controller and the unreduced controller are capable of performing equally well. In figures 6.2 through 6.5 only two outputs and control actions are shown on each graph although three set points were given for each. This was done because only two different scales were available for the ordinate of each graph. However all outputs and control actions for the H_∞ controller for the second linear model and the model reduced controller for the second linear model are covered. In Figures 6.6 and 6.7 all three outputs and controller actions are plotted but those with zero set points cannot be distinguished from each other because they lie on the same lines.

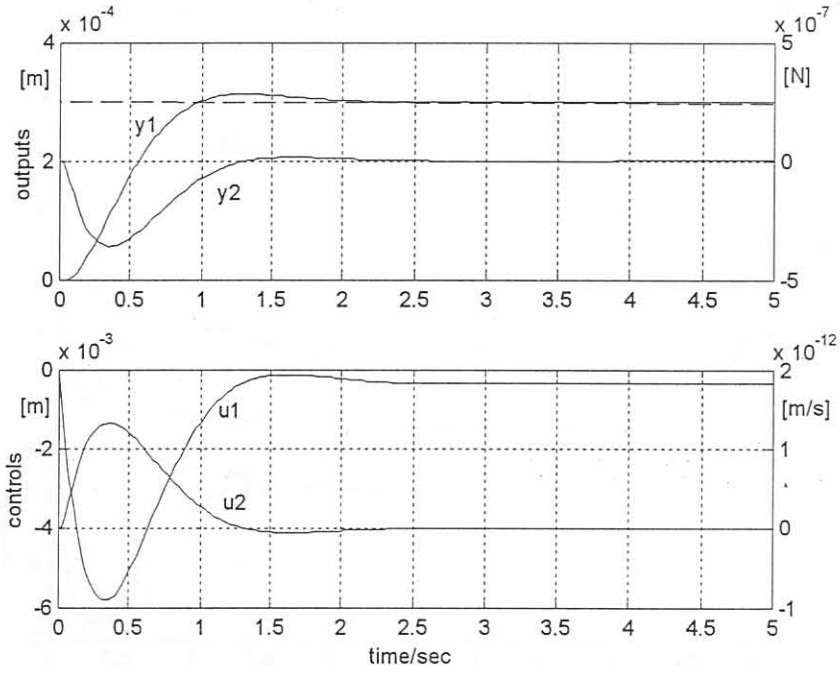

Figure 6.2: Closed-loop simulation results of the H_∞ controller and the second linear model for the set point r = [3e-4 0 0] – (SI units apply).

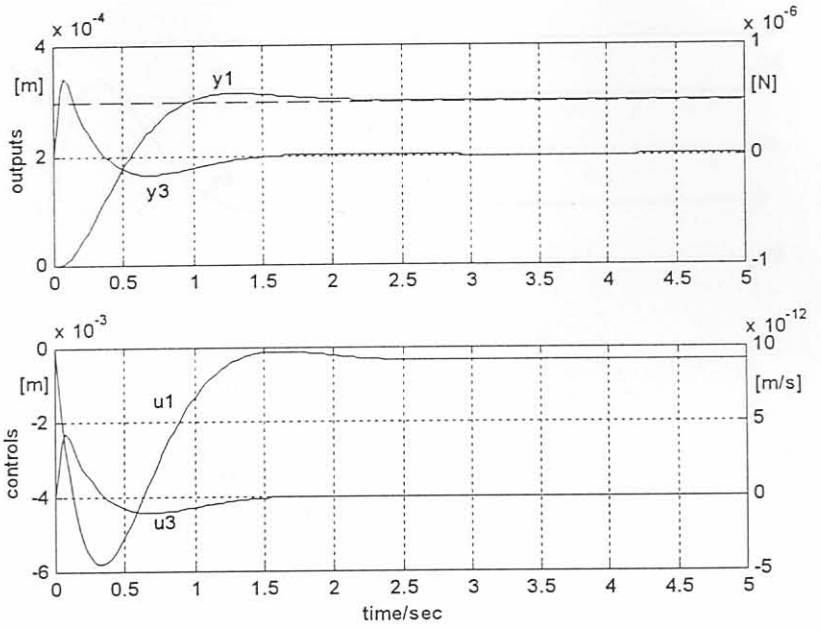

Figure 6.3: Closed-loop simulation results of the H_∞ controller and the second linear model for the set point r = [3e-4 0 0] – (SI units apply).

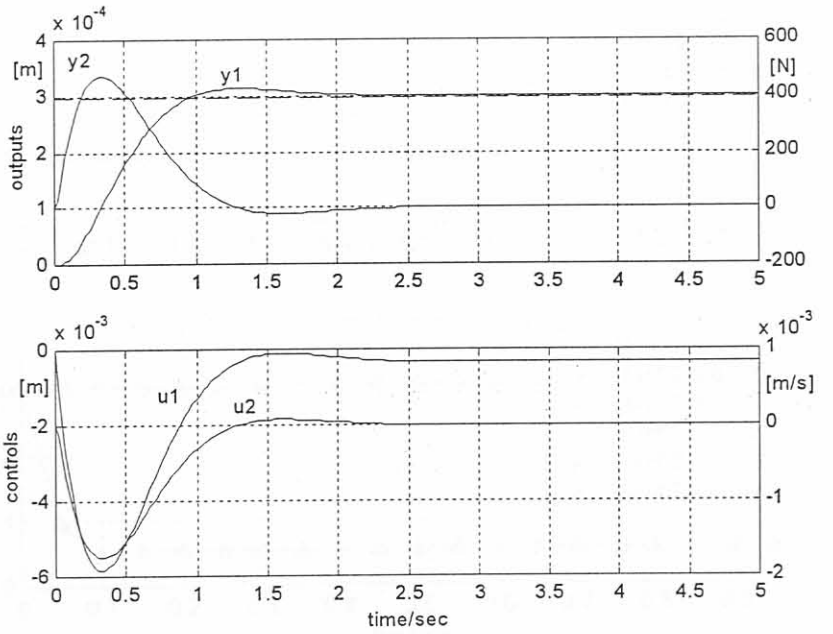

Figure 6.4: Closed-loop simulation results of model-reduced H_∞ controller and the second linear model for the set point r = [3e-4 0 0] – (SI units apply).

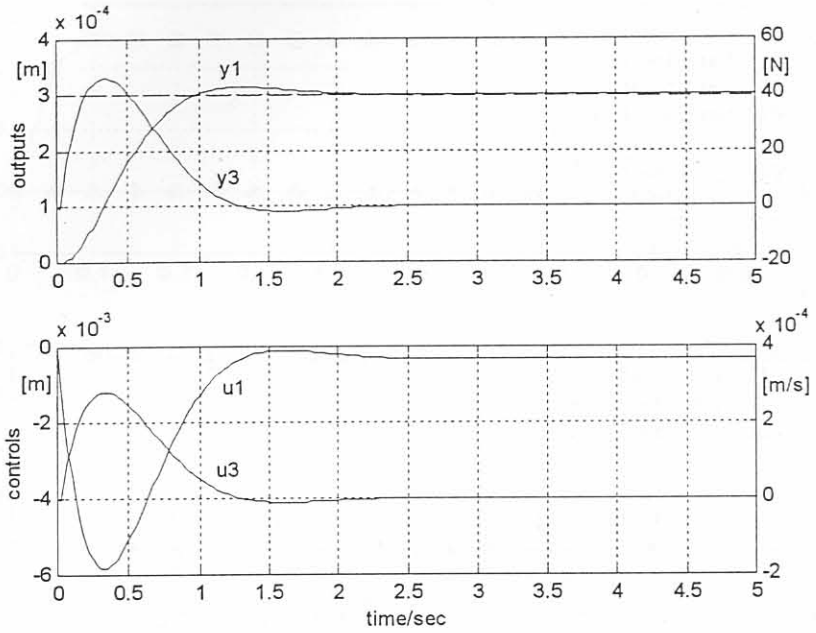

Figure 6.5: Closed-loop simulation results of the model-reduced H_∞ controller and the second linear model for the set point r = [3e-4 0 0] – (SI units apply).

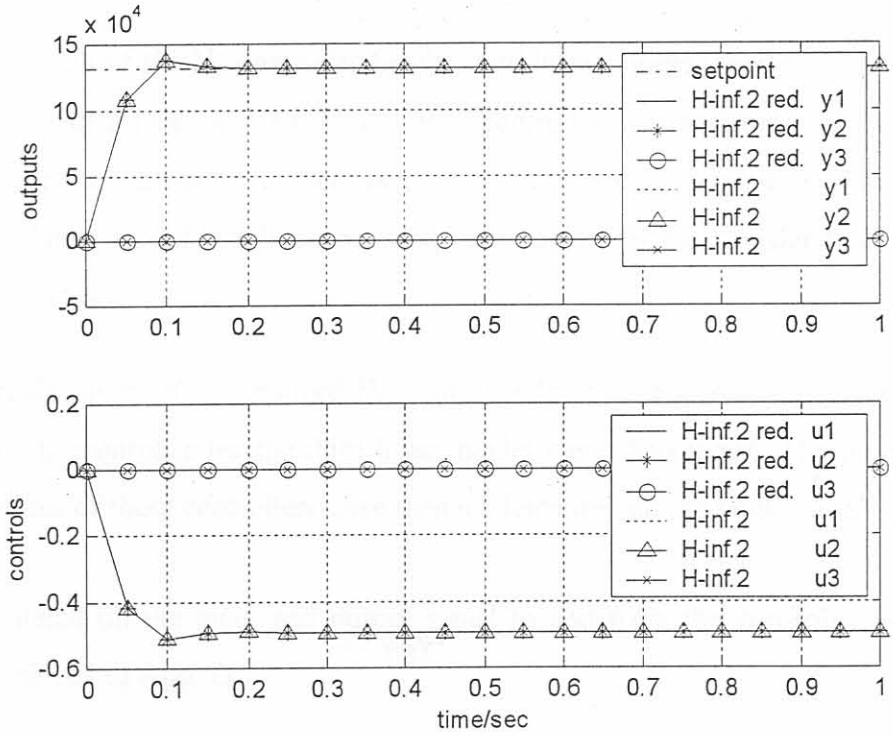

Figure 6.6: Closed-loop simulation results of an H_∞ controller with the second linear model and model-reduced H_∞ controller with the second linear model for the set point r = [0 1.32e5 0] – (SI units apply).

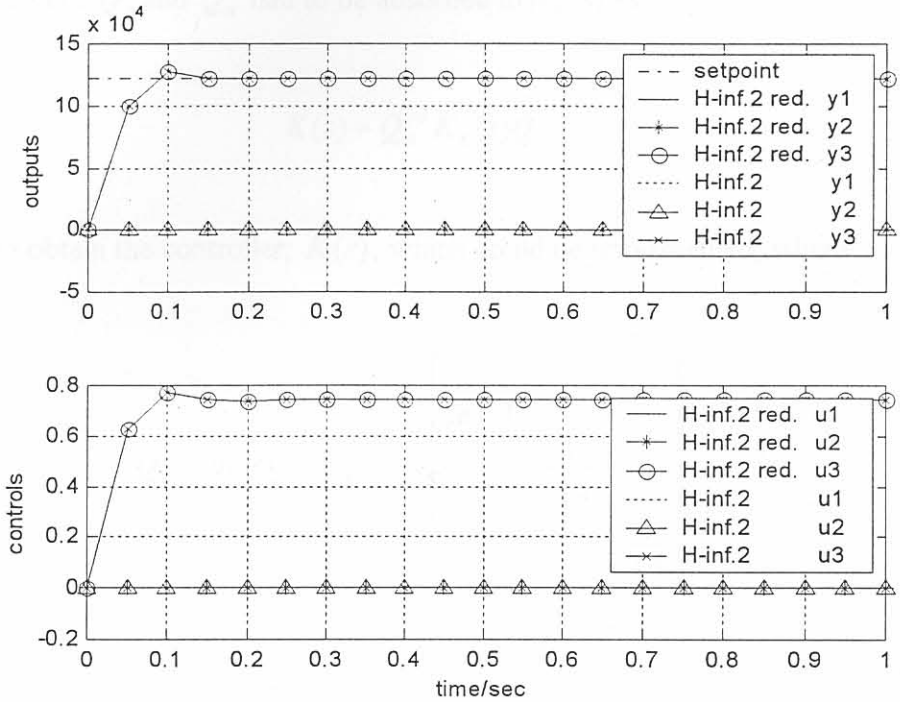

Figure 6.7: Closed-loop simulation results of an H_∞ controller with the second linear model and the model-reduced H_∞ controller with the second linear model for the set point r = [0 0 1.22e5] – (SI units apply).

Model reduction of the H_∞ controller for the third linear model yielded an unstable closed-loop. It was therefore decided to use this controller in its unreduced form. The H_∞ controller for the third linear model has 19 states, which is more than the H_∞ controller for the second linear model has, because the third linear model has transfer function elements with higher orders.

Minimal realizations of the reduced H_∞ controller for the second linear model and of the unreduced H_∞ controller for the third linear model were discretized. The discretized state space matrices of these controllers were then implemented on the nonlinear simulator.

For more detail on the input and output signal to and from the controller and plant the reader is referred to App. D.

Because the H_∞ controllers, $K_s(s)$, were designed for a scaled plant,

$$G_s(s) = Q_y G(s) Q_u^{-1}, \tag{6.1}$$

scaling matrices Q_y and Q_u had to be absorbed in $K_s(s)$ as

$$K(s) = Q_u^{-1} K_s(s) Q_y \quad , \tag{6.2}$$

in order to obtain the controller, $K(s)$, which could be implemented, where

$$Q_u = diag[1/u_{j\max}] = \begin{bmatrix} \frac{1}{1e-3} & 0 & 0 \\ 0 & \frac{1}{0.4} & 0 \\ 0 & 0 & \frac{1}{0.4} \end{bmatrix} \tag{6.3}$$

and

$$Q_y = diag[1/y_{j\max}] = \begin{bmatrix} \frac{1}{3e-4} & 0 & 0 \\ 0 & \frac{1}{2e6} & 0 \\ 0 & 0 & \frac{1}{0.5e6} \end{bmatrix}. \tag{6.4}$$

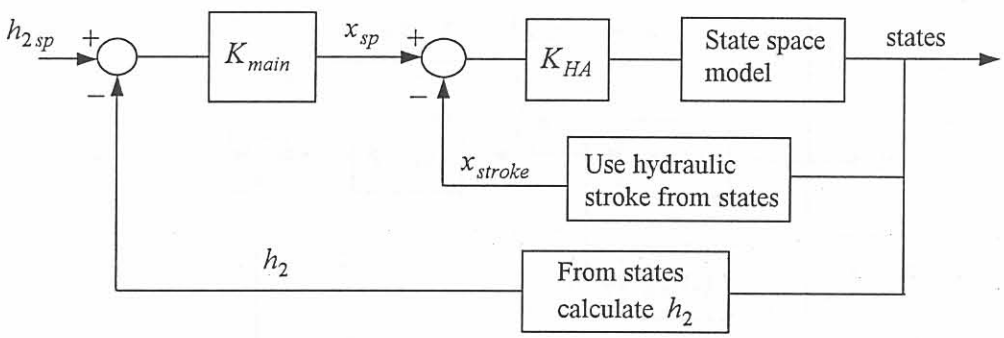

Figure 6.8: Control action of designed controller schemes applied to hydraulic actuator control loop.

Fig. 6.8 shows how the controller action, $u_1 = x_{sp}$ (hydraulic stroke set point) of the diagonal or H_∞ controllers, indicated by K_{main}, are applied to the simulator. Seen in isolation from the exit gauge /tension interactions the block diagram in this figure shows

that the feedback loop of the output, y_1, which is exit gauge, h_2, yields a cascade structure, when controlled by the diagonal or H_∞ control action, u_1. In this figure K_{HA} represents the hydraulic actuator PI controller.

For the controller implementation on a plant with inner loop tension control, such as for the second and third linear model, the scheduling of the inner loop tension control and H_∞ controller action is illustrated in Fig. 6.9 for back tension control. This scheduling is implemented such that the tensions are controlled by PI controllers of the inner loop tension control after every time step of length Δt_{main} where $\Delta t_{tension} < \Delta t_{main}$. This means that inner loop tension control actions are applied at a higher frequency than the H_∞ control actions. The summation of the H_∞ control action and the previous PI control action of the inner loop tension control is done in order to bring the control action of the H_∞ controller close to the control action of the PI controllers, which do most of the manipulating work on the plant tension outputs.

The same configuration, as in Fig. 6.9, applies to front tension control.

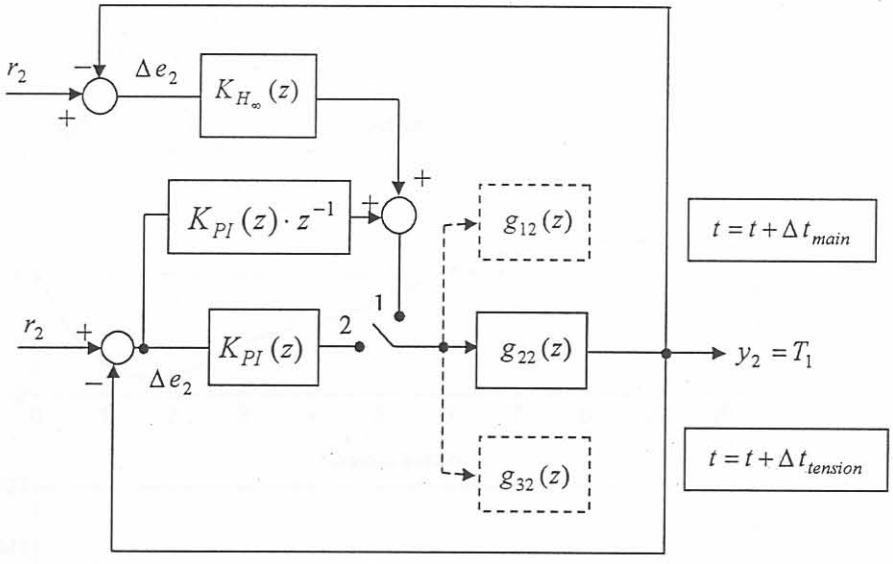

If Δt_{main} multiple of t : switch position 1
else : switch position 2

with $\Delta t_{tension} < \Delta t_{main}$

Figure 6.9: Control action scheduling of H_∞ and inner loop tension controller.

The results that are presented in this chapter's sections to follow were all simulated with a step set point change of the front tension from 10 N to its set up value. This kind of set point change occurs at the beginning of a pass when the tensions are established [41]. In particular section 6.2 contains the results when a diagonal controller scheme was applied to the nonlinear plant without inner loop tension control and gauge meter compensation. Sections 6.3 and 6.4 show results from simulations with H_∞ controllers implemented on a plant which did incorporate inner loop tension control and gauge meter compensation, where the difference between the latter two H_∞ controllers lies in the linear models on which their designs were based, i.e. the second and third linear model. In a discussion of the results in section 6.5 the three controllers are compared. The chapter is concluded with some words about the context of the controller design.

6.2 Results of Diagonal Controller Implementation on Nonlinear Simulator

The results presented in this section are from a simulation of the nonlinear plant in closed loop with the diagonal PID controller of which the design was discussed in section 5.3.

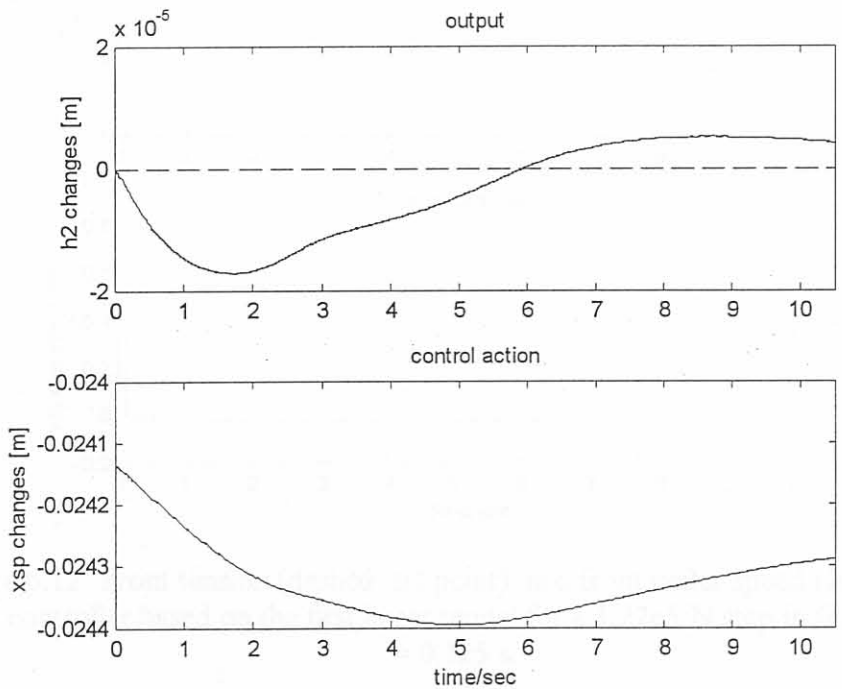

Figure 6.10: Exit gauge changes (dashed: set point) and hydraulic actuator stroke set point changes for a diagonal controller based on first linear model for a 1.22e5 N step in front tension at t = 0.125 s.

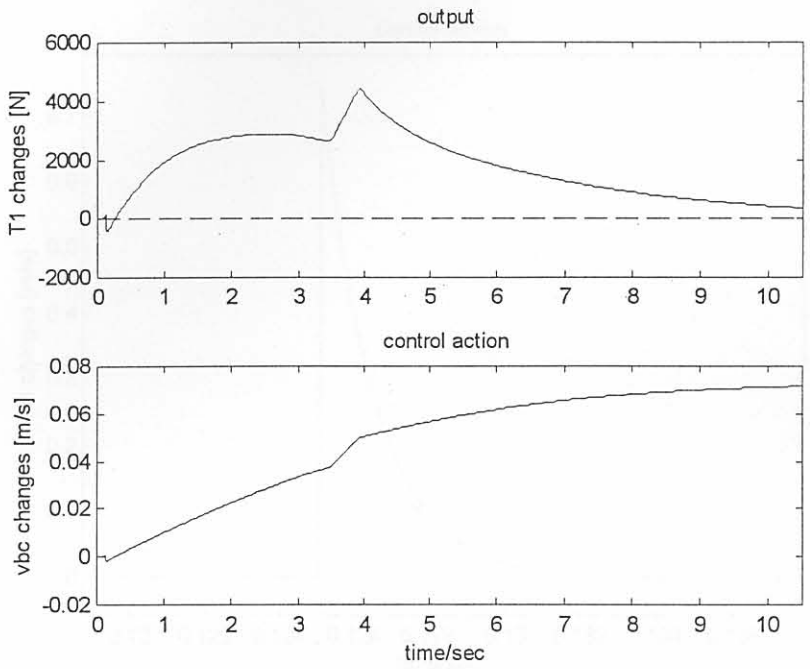

Figure 6.11: Back tension changes (dashed: set point) and back coiler speed changes for a diagonal controller based on the first linear model for a 1.22e5 N step in front tension at t = 0.125 s.

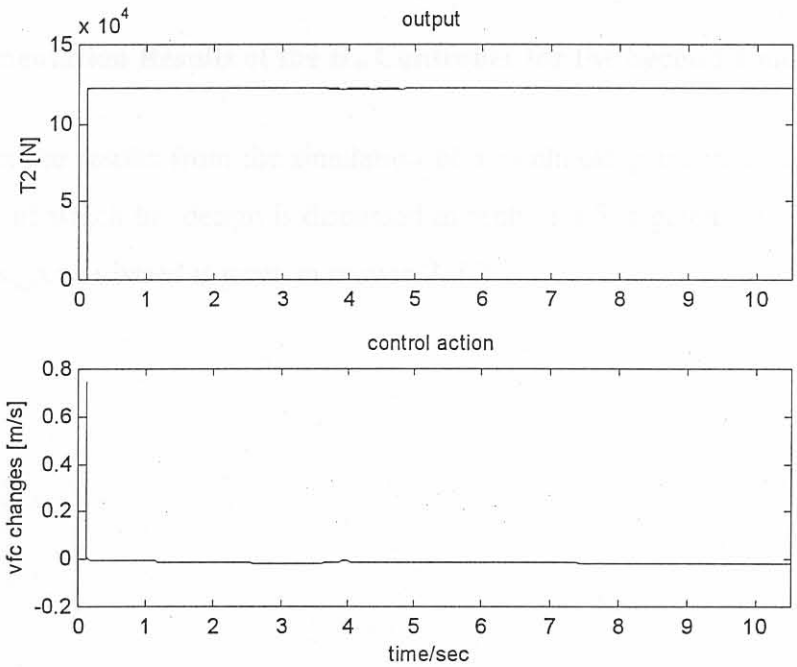

Figure 6.12: Front tension (dashed: set point) and front coiler speed changes for a diagonal controller based on the first linear model for a 1.22e5 N step in front tension at t = 0.125 s.

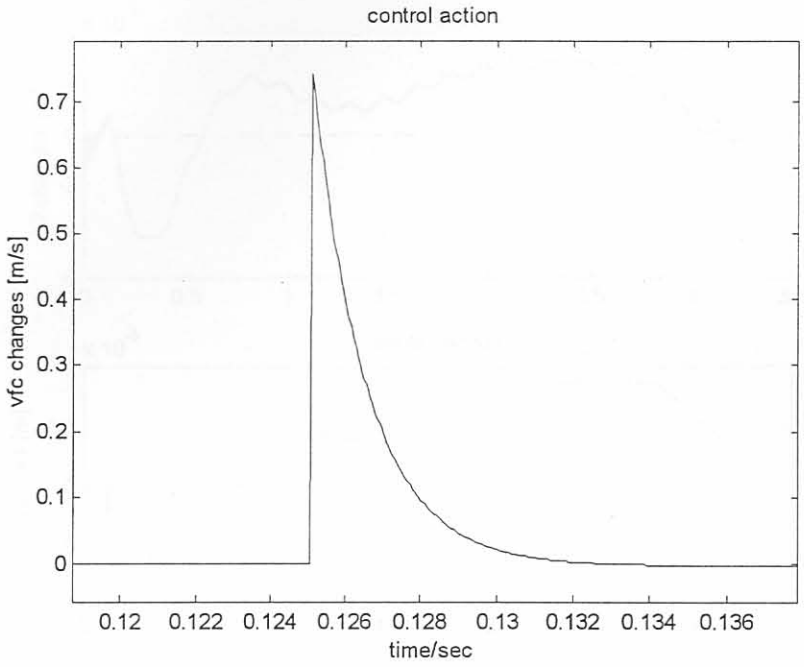

Figure 6.13: Control action (front coiler speed changes) of diagonal controller based on first linear model for a 1.22e5 N step in front tension at t = 0.125 s.

6.3 Implementation Results of the H_∞ Controller for the Second Linear Model

In this section the results from the simulation of a nonlinear plant in closed loop with an H_∞ controller of which the design is discussed in section 5.5 is given. The linear model on which this design was based is given in section 3.4.2.

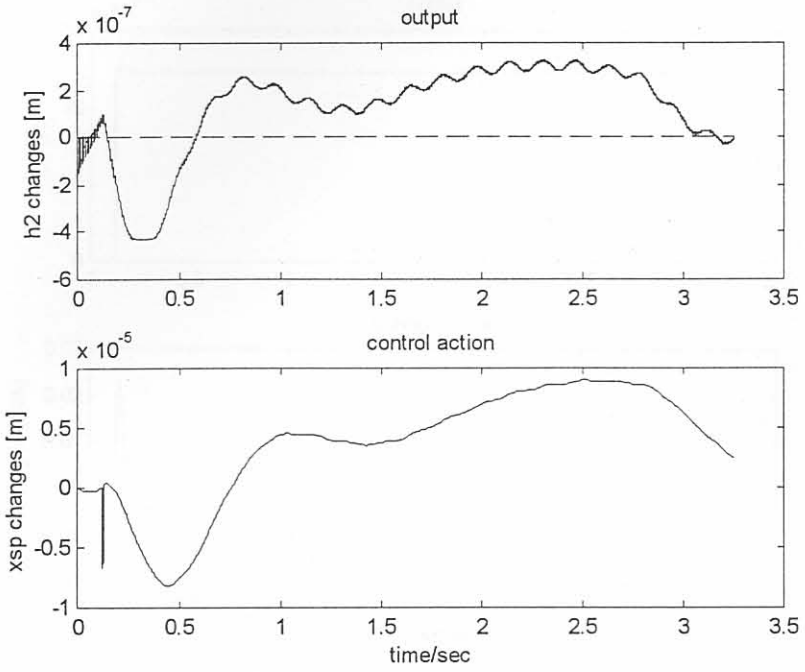

Figure 6.14: Exit gauge changes (dashed: set point) and hydraulic actuator stroke set point changes for the H_∞ controller based on the second linear model for a 1.22e5 N step in front tension at t = 0.125 s.

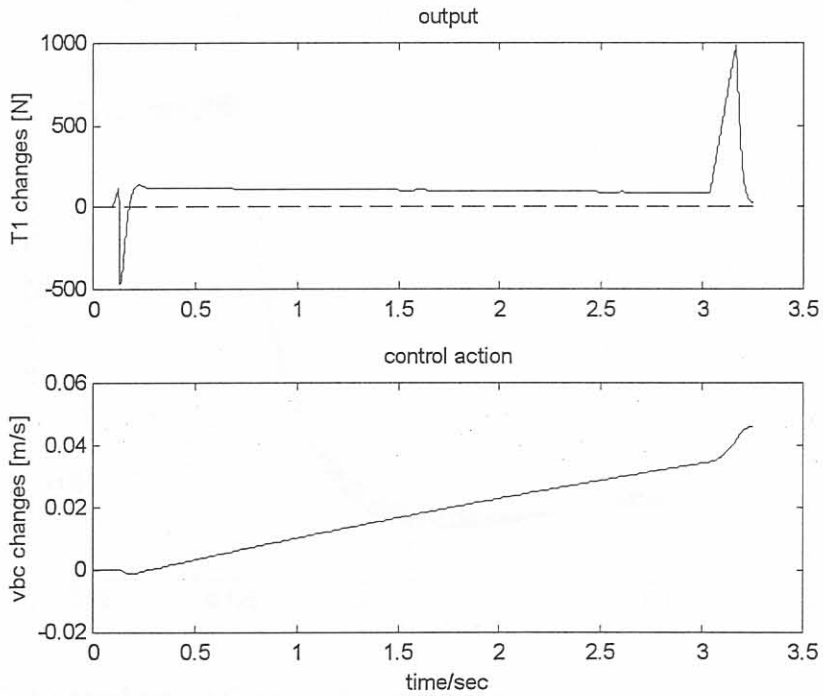

Figure 6.15: Back tension changes (dashed: set point) and back coiler speed changes for the H_∞ controller based on the second linear model for a 1.22e5 N step in front tension at t = 0.125 s.

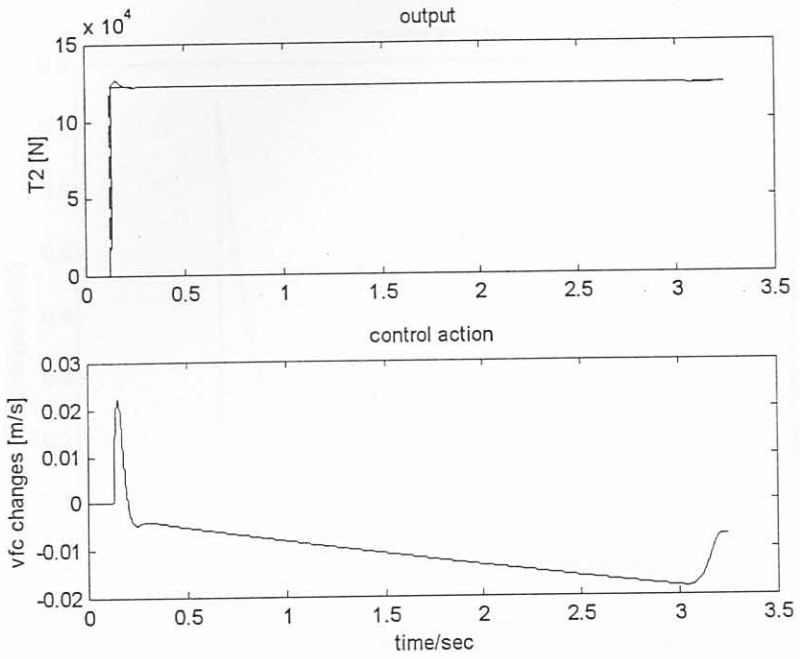

Figure 6.16: Front tension (dashed: set point) and front coiler speed changes for the H_∞ controller based on the second linear model for a 1.22e5 N step in front tension at t = 0.125 s.

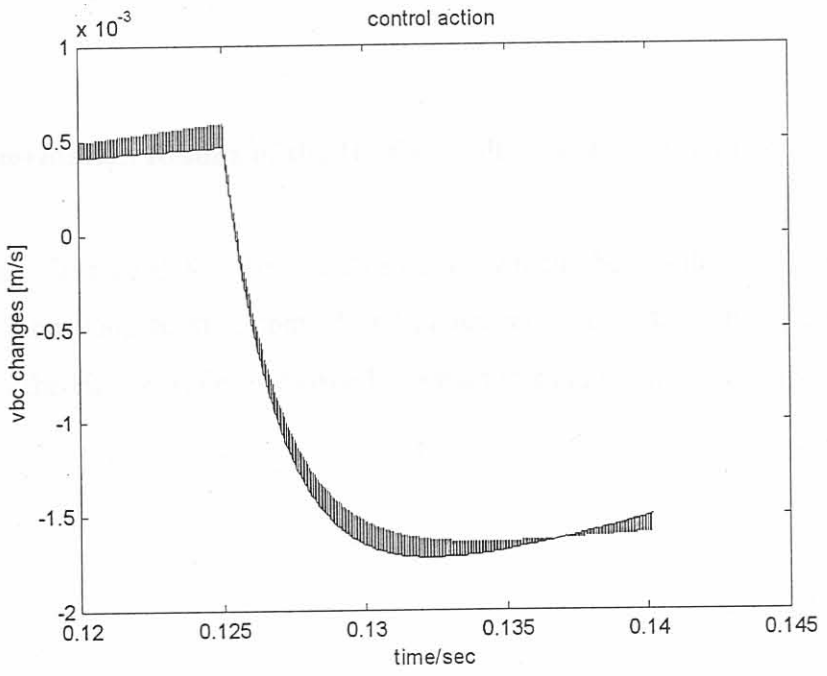

Figure 6.17: Control action (back coiler speed changes) of inner loop tension control for the H_∞ controller based on the second linear model for a 1.22e5 N step in front tension at t = 0.125 s.

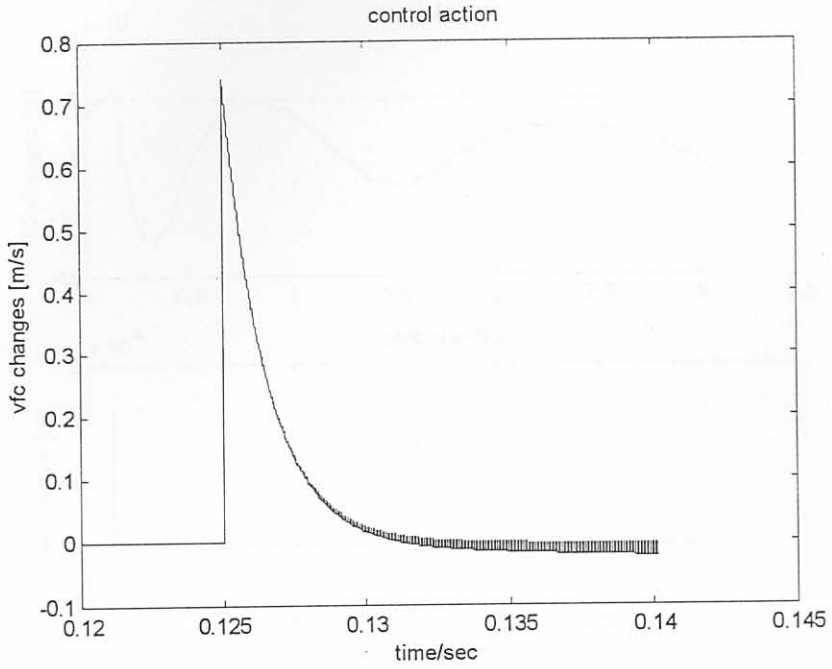

Figure 6.18: Control action (front coiler speed changes) of inner loop tension control for the H_∞ controller based on the second linear model for a 1.22e5 N step in front tension at t = 0.125 s.

6.4 Implementation Results of the H_∞ Controller for the Third Linear Model

The nonlinear plant used for the simulations of which the results are presented in this section, had inner loop tension control and gauge meter compensation incorporated in it. The design of the H_∞ controller in closed loop with this plant was given in section 5.6.

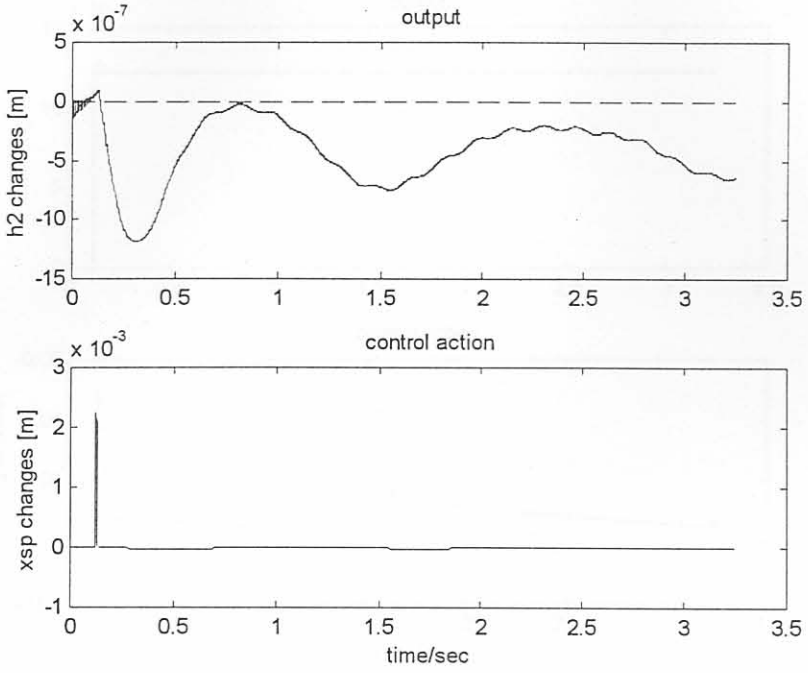

Figure 6.19: Exit gauge changes (dashed: set point) and hydraulic actuator stroke set point changes for the H_∞ controller based on the third linear model for a 1.22e5 N step in front tension at t = 0.125 s.

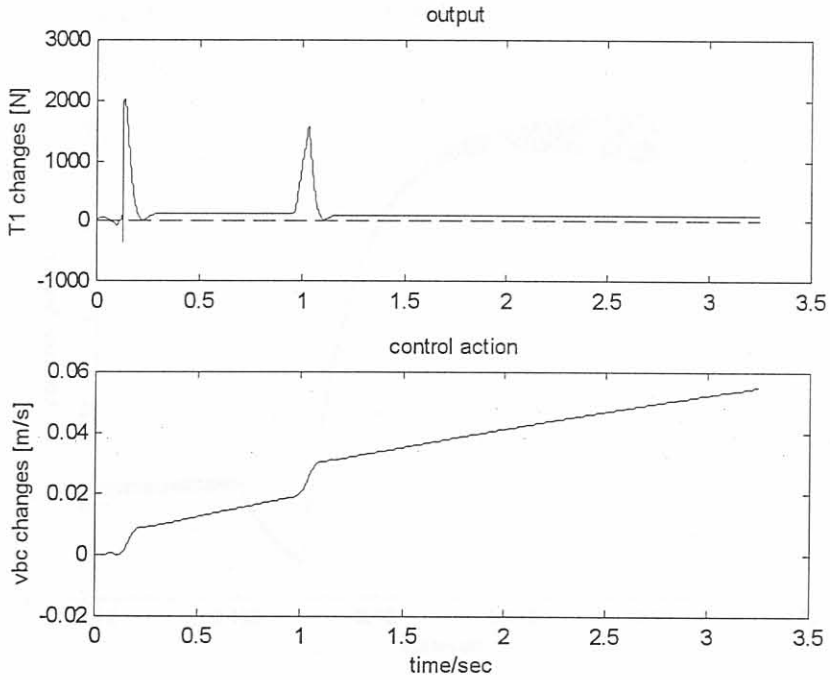

Figure 6.20: Back tension changes (dashed: set point) and back coiler speed changes for the H_∞ controller based on the third linear model for a 1.22e5 N step in front tension at t = 0.125 s.

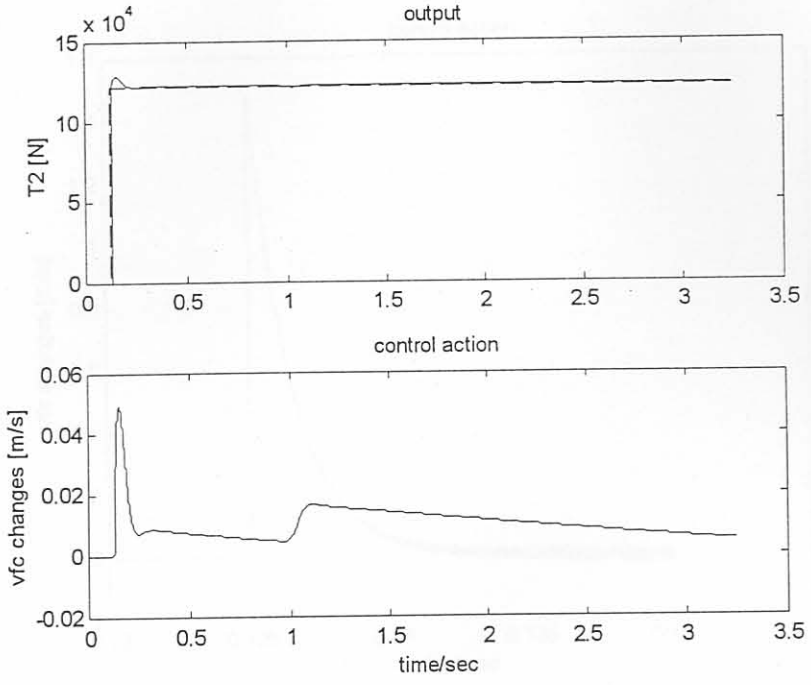

Figure 6.21: Front tension (dashed: set point) and front coiler speed changes for the H_∞ controller based on the third linear model for a 1.22e5 N step in front tension at t = 0.125 s.

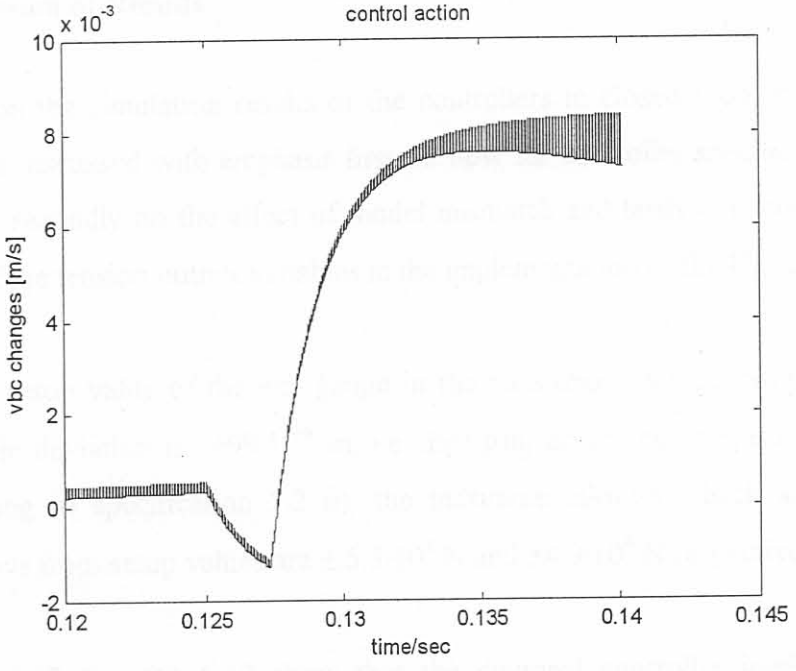

Figure 6.22: Control action (back coiler speed changes) of inner loop tension control for the H_∞ controller based on the third linear model for a 1.22e5 N step in front tension at t = 0.125 s.

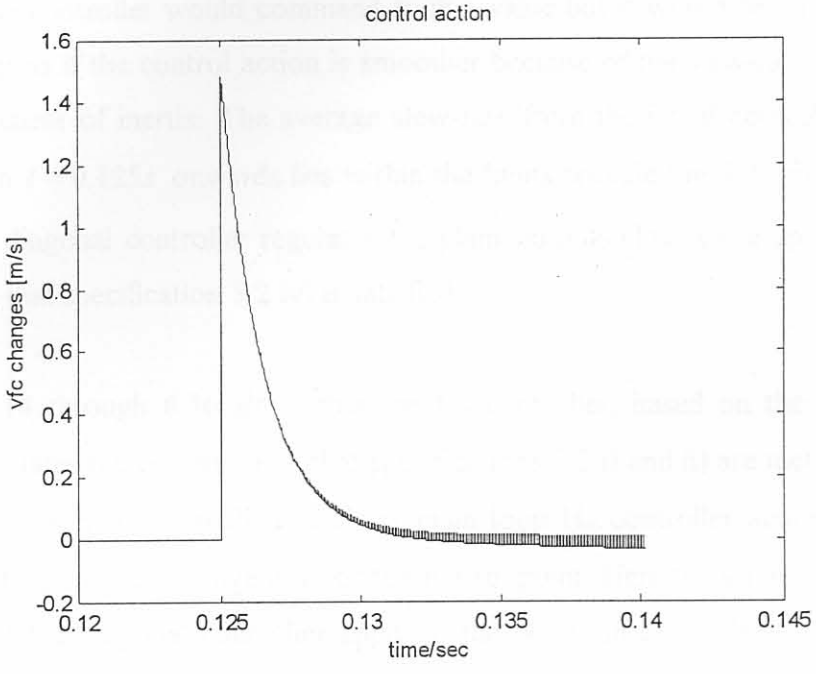

Figure 6.23: Control action (front coiler speed changes) of inner loop tension control for the H_∞ controller based on the third linear model for a 1.22e5 N step in front tension at t = 0.125 s.

6.5 Discussion of Results

In this section the simulation results of the controllers in closed loop with the nonlinear simulator are discussed with emphasis first on how far controller specifications in section 5.2 are met, secondly on the effect of model mismatch and lastly it is commented on the behaviour of the tension output variables in the implementation of the H_∞ controllers.

i) For the setup value of the exit gauge in the pass under consideration, the maximum allowable deviation is $\pm 99 \cdot 10^{-6}$ m, i.e. ±99 μm, according to specification i) in 5.2. According to specification 5.2 ii), the maximum allowable back and front tension deviations from setup values are $\pm 5.3 \cdot 10^4$ N and $\pm 4.9 \cdot 10^4$ N respectively.

Figures 6.10 through 6.12 show that the diagonal controller implemented on the nonlinear simulator meets specifications 5.2 i) and ii). The controller actions are shown on the same figures and also on Fig. 6.13. The curves representing the controller action, u_3, i.e. front coiler speed, in figures 6.12 and 6.13 have points in which derivatives are non-existent. These points can be attributed to the fact that the PI

controllers always have an initial value when implemented in the velocity form. In practice the controller would command such a value but it would result in a response of the plant as if the control action is smoother because of the slew-rate limited by the coilers moment of inertia. The average slew-rate from the initial control action value of u_3 from $t = 0.125s$ onwards lies within the limits specified in 5.2. iii). The way by which the diagonal controller regulates the plant outputs close to setup values, points to the fact that specification 5.2 iv) is satisfied.

Figures 6.14 through 6.16 show that the H_∞ controller, based on the second linear model, regulates the outputs such that specifications 5.2 i) and ii) are met. Figures 6.17 and 6.18 show inner loop PI as well as main loop H_∞ controller actions for tension control during the step change in front tension set point. Here the same arguments as in the case of the diagonal controller apply to the points in controller actions in which derivatives are non-existent. The average slew-rate for the control actions, $u_2 = v_{bc}$ and $u_3 = v_{fc}$ however lie within the limits specified. Again for this H_∞ controller scheme figures 6.14 through 6.16 show that 5.2 iv) is satisfied.

In figures 6.19 through 6.21 it can be seen that the H_∞ controller, which is based on the third linear model, regulates the plant outputs within the specified limits in 5.2 i) and ii). The slew-rate as shown in Fig. 6.22 can be obtained in practice however not the one shown in Fig.6.23. Here again points in control actions, u_2 and u_3, in which derivatives do not exist, are present. The same arguments, as mentioned in the case of the diagonal controller, apply to these points. The trends of the outputs in figures 6.19 through 6.21 show that specification 5.2 iv) is met for the duration of the simulation.

ii) The closed-loop simulation results with the nonlinear simulator show that model mismatch affects both, the diagonal controller and the H_∞ controller designed for the third linear model.

In the case of the diagonal controller, the PID controller, $k_{11}(s)$, was designed for a transfer function, $g_{11}(s)$, for which the tension model was excluded during SID, i.e. SID was performed on an incomplete model.

In the case of the H_∞ controller for the third linear model, the slew-rate of the controller action, u_3, is too high. This can be attributed to model mismatch. Model mismatch is weighing more for the controller based on the third linear model than for the controller based on the second linear model. This is so because from the transfer function $g_{31}(s)$ the controller for the third model is designed from the information that for a decrease in exit gauge, i.e. the input to $g_{31}(s)$, the front tension is lower than the average measured front tension (see Fig. 3.40). Therefore the tendency of this controller is to command a control action, u_3, which exceeds the limits specified in 5.2. iii), for a decrease in exit gauge.

iii) In the output data of transfer functions $g_{21}(s)$ and $g_{31}(s)$ nonlinear behaviour for hydraulic stroke step input in the case of the plant with inner loop tension control and gauge meter compensation (see figures 3.39 and 3.40) can be seen. It is the authors opinion that this nonlinear behaviour is reflected as spikes on the tension outputs when the plant is in closed loop with the H_∞ controllers designed for the second and third linear models. It could be that these spikes appear because this nonlinear behaviour has not been taken into account in the identification of the transfer functions, $g_{21}(s)$ and $g_{31}(s)$. This behaviour of $g_{21}(s)$ and $g_{31}(s)$ can be attributed to a disturbance due to exit gauge/tension interaction since the tensions are the controlled variables and the coiler speeds the manipulated variables when a plant with inner loop tension control is considered. A plant with inner loop tension control means that the integrator transfer functions, $g_{22}(s)$ and $g_{33}(s)$, from the first linear model are in closed loop with PI-controllers. Changes in exit gauge, such as during its steady state development, can therefore be seen as disturbances to the inner tension control loops.

6.6 Context and Evaluation of Controller Design

As point of linearization for the identification of a linear model an operating point was chosen on the speed up ramp of the rolling process. This model and consequently the controller design based on it are valid for only a small part for this phase of a rolling pass. The controller design investigations in this work were aimed at a controller, which would regulate the process for a time fraction of the speed up ramp at 3.5 ± 0.2 m/s main drive

peripheral speed. From Fig. 3.2 it can be seen that this gives a controller 0.5 seconds to control the output variables back to within their limits specified in section 5.2.

For a functional control system during the speed up phase of a pass a whole set of controllers would be needed each operating at a different main drive speed. A control system, which coordinates the operation of every controller within this set, could be placed in the category of switching control systems.

In [37] a criterion for the switching time, at which a switching controller comes into action, is presented. According to [37] the switching time is determined from a bounding function and a norm of a vector of which the components are the switching controller states as well as filtered errors.

Given the abovementioned requirements for a switching controller the H_∞ controller for the second linear model qualifies as an element in a set of suitable switching controllers. The diagonal controller scheme can also be said to qualify as a suitable switching controller because it keeps the plant output variables within specified limits during the time available. The H_∞ controller for the third linear model however does not meet specification 5.2 iii) and therefore cannot be used as a switching controller.

Real plant data shows a severe exit gauge decrease (approximately 50 micrometers) as a result of the severe increase in front tension during the first moments of the speed up phase of the rolling pass [38].

6.7 Conclusion

Closed-loop simulations of the plant outputs and control actions have been shown for all three the controller schemes implemented on the nonlinear simulator. From the simulation graphs it became clear that the diagonal controller and the H_∞ controller for the second linear model comply with the requirements specified in 5.2.

The adverse effect of model mismatch can be seen in the performance of the diagonal controller and also in the excessive control action of the H_∞ controller for the third linear model.

With respect to the requirements for a switching controller it was found that the H_∞ controller for the second linear model is an option more suited than the other two controllers.

CHAPTER 7

CONCLUSIONS AND RECOMMENDATIONS

7.1 Conclusions

The investigations done in this dissertation were aimed at the implementation of a controller scheme on a point during the acceleration phase of a simulated multivariable hot rolling mill process. For this purpose a nonlinear plant simulator, developed in [4], was used to identify linear models for controller design, and to serve as plant on which the controllers could be tested.

Three linear models were identified from simulations of the nonlinear plant simulator, i.e.:

i) A first linear model in which the tension model was part of the simulator except for generation of SID data for the transfer function, $g_{11}(s)$. Gauge meter compensation and inner loop tension control, i.e. control at a higher frequency than the control designed for the plant as a whole, were not part of the simulator used for the first linear model.

ii) A second linear model was identified from data of a simulator, in which gauge meter compensation and inner loop tension control was incorporated. However, only the transfer functions on the diagonal were identified for this model.

iii) The third linear model was the same as the second linear model except that in addition, the off-diagonal transfer functions have also been identified, i.e. they were nonzero.

It was found that gauge meter compensation counteracted the phenomenon that tension oscillations result in exit gauge variations. The inner loop tension control was applied to the simulator in addition to gauge meter compensation in order to prevent tensions from becoming negative. From the steady state gain of the transfer function, $g_{11}(s)$, of the three

linear models it was found, that a conversion of hydraulic stroke to exit gauge change is 87% when using gauge meter compensation. Without compensation this conversion is only 41%.

A diagonal PID/PI controller was designed for the first linear model while for the second and third LTI models a diagonal and an MIMO H_∞ controller were designed respectively. From the controller designs and from the closed-loop simulations of the three controller schemes and the simulator the following can be concluded.

i) With respect to the first aim in chapter 1 it can be concluded that the controller designs are only valid for the main drive peripheral speed range of $v_{main} = 3.5 \pm 0.2$ m/s.

ii) The first and second LTI models are suitable for controller design because in their case model mismatch does not affect their corresponding controller designs as adversely as in the case of the third linear model. This is so because from the transfer function $g_{31}(s)$ the controller for the third model is designed from the information that for a decrease in exit gauge, i.e. the input to $g_{31}(s)$, the front tension that differs a lot from the average measured front tension (see Fig. 3.40). For the diagonal PID/PI and diagonal H_∞ controller design however only the transfer functions on the diagonal were used.

iii) One of the aims of this work was an investigation of using gauge meter compensation and inner loop tension control. It was found that they make it possible that an LTI model, for which transfer functions were identified only on the diagonal, can be used for controller design, i.e. the process gets decoupled to an extent.

iv) Regarding the fourth aim of this work it can be concluded that a diagonal PID/PI controller, a diagonal H_∞ and an MIMO H_∞ controller could be designed based on the first, second and third linear models respectively. It needs to be emphasized here that the control of the H_∞ controllers is on a plant with gauge meter compensation and inner loop tension control being part of the plant.

v) With the realization of the fifth aim, it was found that when implementing the controllers in C++, the velocity form implementation of the inner loop tension controllers yields slew-rates of coiler speed control actions, which are high. This could be attributed to the nonzero initial control actions of these controllers (PI controllers).

vi) With respect to the sixth aim in chapter 1 it can be concluded from the closed loop simulations with the simulator and the three controller schemes, mentioned under point iv) above, that a diagonal model is sufficient for controller design. This could be seen from the diagonal PID/PI and diagonal H_∞ controller's fulfillment of the specifications in section 5.2 as well as the specification for a switching controller as mentioned in section 6.6. In particular the diagonal H_∞ controller was found to be the most suitable one for a switching control system.

This work shows that control on the speed-up ramp is possible and has the possible advantage of reducing off-specification strip produced during this phase of rolling. Such a benefit can become real when the suited controllers as designed in this work are used within a switching control system valid for the whole speed up ramp.

7.2 Recommendations

For further research on this project recommendations are given concerning identification of a linear model and control system design.

7.2.1 System Identification

Points of linearization that cover the speed range outside the speed range considered for this work should be chosen for system identification of linear models. The models can then be used for the development of various control systems, which control the process during the acceleration phase as mentioned in the next section. It is recommended to do such a system identification on a simulator, which has gauge meter compensation and inner loop tension control incorporated in it, in order to reap the benefit of a process which is decoupled to an extent.

7.2.2 Control System Design

i) H_∞ controllers can be designed for each operating point for which a linear model has been estimated. This should be done because the diagonal H_∞ controller,

designed in this work, is only valid for the range $v_{main} = 3.5 \pm 0.2$ m/s of the mill main drive peripheral speed. A switching control strategy can then be developed and employed to be able to run simulations on the whole speed up ramp. It is expected that control error changes such as a front tension set point change from 10 N up to its set up value could be counteracted with the implementation of a switching control strategy during the whole speed up ramp of a rolling pass.

ii) The inner loop tension controller can be implemented in state space with zero initial conditions instead of a velocity form in order to obtain zero initial control actions and thus smoother control action trends for the inner loop tension control.

BIBLIOGRAPHY

[1] A. Lederer, "State of development of Steckel mills," *Metallurgical Plant and Technology International*, vol.16, no.3, pp.56-69, 1993.

[2] S. Kramer, G. Kneppe and D. Rosenthal, "Technology and performance of modern Steckel mills," *Iron and Steel Engineer*, vol. 74, no.7, pp.17-26, 1997.

[3] T.S. Bilkhu, A.F. MacAlister and P.J. Reeve, "Automation in hot strip mill modernization," *Iron and Steel Engineer*, pp. 27-33, August 1995.

[4] E. Scholtz, "Modeling for control of a Steckel hot rolling mill," Master's thesis, Department of Electrical and Electronic Engineering, University of Pretoria, 1999.

[5] Broner Group, IAS, "11'th International Rolling Training Course," Barcelona, 1998.

[6] T.E. Marlin, J.D. Perkins, G.W. Barton and M.L. Brisk, *Advanced process control applications*, NC: Instrum. Society of America, Research Triangle Park, 1987.

[7] B. Avitzur, *Handbook of metal-forming processes*, ch. 13, John Wiley and Sons, Inc., 1983.

[8] G. Hearns and M.J. Grimble, "Robust hot strip mill thickness control," *Proceedings of the 9th IFAC MMM Conference*, Cologne, Germany, pp. 205-210, 1998.

[9] Y. Anbe, K. Sekiguchi and H. Imanari, "Tension control of a hot strip mill finisher," *13th IFAC Triennial World Congress*, San Francisco, USA, pp. 439-444, 1996.

[10] A.F. MacAlister, P.J. Reeve and P.Smith, "Predictive control of temperature and width for hot strip mills," *Proceedings of the 9th IFAC MMM Conference*, Cologne, Germany, pp. 233-239, 1998.

[11] A. Randall, P.J. Reeve and A.F. MacAlister, "Disturbance attenuation in a hot strip rolling mill via feedforward adaptive control," *13th IFAC Triennial World Congress*, San Francisco, USA, pp. 463-468, 1996.

[12] M.J. Grimble and M.R. Katebi, "Predictive optimal control of hot strip finishing mills," *IFAC Automation in the Steel Industry*, Kyongju, Korea, IFAC, Elsevier, 1997.

[13] F.R. Camisani-Calzolari, Z.M. Smit, I.K. Craig and R. Torr, "Scrap reduction in the rolling of aluminium sheet," *IEEE International Symposium on Industrial Electronics*, Pretoria, South Africa, 1998.

[14] M. Jelali, U. Müller, A. Wolff and W. Ungerer, " Advanced control strategies in rolling mills,"*Stahl und Eisen*, vol. 121, no.2, February 2001.

[15] M.J. Grimble, M.R. Katebi, G. Hearns and M.A. Johnson, "International training course in hot rolling mill control and technology," University of Strathclyde, Glasgow, Scotland, 14-18 September 1998.

[16] E. Scholtz, M. Lewis, H. Pretorius and J. Botha, " Control practice on a Steckel hot rolling mill process," Subject EBB 780, Department of Electrical and Electronic Engineering, University of Pretoria, 1999.

[17] W. Dobrucki and A. Bar, "Changes in roll-gap shape in the case of vibrations in a four high rolling mill stand," *Journal of Materials Processing Technology*, vol.61, pp.328-337, 1996.

[18] E. Orowan, "The calculation of roll pressure in hot and cold flat rolling," *Proceedings of the Institution of Mechanical Engineers*, vol. 150, pp. 140-167, 1943.

[19] J.V. Roey, H. Vergote and R. Mielke, "Accurate profile and flatness control on a modernized hot strip mill," *Iron and Steel Engineer*, pp.29-33, February 1996.

[20] G.E. Dieter, *Mechanical metallurgy*, ch.7. McGraw-Hill, 1986.

[21] L.M. Pedersen and B.Wittenmark, "Multivariable controller design for a hot rolling mill," *IEEE Transactions on Control Systems Technology*, vol. 6, no.2, pp. 304-312, March 1998.

[22] N. A. Fleck and K.L. Johnson, "Towards a new theory of cold rolling thin foil," *International Journal of Mechanical Science*, vol. 29, no.7, 1987.

[23] W.Y.D. Yuen, A. Dixon and D.N. Nguyen, "The modelling of the mechanics of deformation in flat rolling," *Journal of Materials Processing Technology*, vol. 60, pp. 87-94, 1996.

[24] E. Scholtz, I.K. Craig and P.C. Pistorius, "Modeling for control of a Steckel hot rolling mill," *ISIJ International*, vol. 40, no.10, pp. 1003-1012, October 2000.

[25] L. Ljung, *System identification toolbox*, The Math Works, Inc.,1997.

[26] W.L. Luyben, *Process modeling, simulation and control for chemical engineers*, 2nd edition, Mc Graw-Hill, 1990.

[27] G. Kneppe and W. Rohde, "Economical rolling of stainless steels on Steckel mills," *Metallurgical Plant and Technology International*, pp.58-70, 1/1993.

Bibliography

[28] K. Zhou, J.C. Doyle and K. Glover, *Robust and optimal control*, Prentice Hall Inc., New Jersey, 1996.

[29] A. Stoorvogel, *The H_∞ control problem*, Prentice Hall International (U.K.) Ltd., 1992 .

[30] I.K. Craig, "Sensitivity of H_∞ controller designs to structured uncertainty," Master's thesis, Massachusetts Institute of Technology, 1989.

[31] S. Skogestad and I. Postlethwaite, *Multivariable feedback control*, John Wiley & Sons Ltd., England, 1996.

[32] J.C. Doyle, K. Glover, P.P. Khargonekar and B.A. Francis, "State-space solutions to standard H_2 and H_∞ control problems," *IEEE Transactions on Automatic Control*, August 1989.

[33] M. Morari and E. Zafiriou, *Robust process control*, Prentice-Hall, Inc., New Jersey, 1989.

[34] G.C. Goodwin, S.F. Graebe and M.E. Salgado, *Control system design*, Prentice-Hall, Inc., New Jersey, 2001.

[35] M.J. Steeper and D.G. Park, "Development of steering control system reversing hot mills," *Iron and Steel Engineer*, pp. 21-24, November 1998.

[36] D.E. Seborg, T.F. Edgar and D.A. Mellichamp, *Process dynamics and control*, John Wiley and Sons, Inc., USA, 1989.

[37] M.H. Chang and E. J. Davison, "Adaptive switching control of LTI MIMO systems using a family of controllers approach," *Automatica*, 35, pp. 453-465, 1999.

[38] A. Jordaan, Columbus Stainless, Private Communication, 2002.

[39] I.K. Craig and R.G.D. Henning, "Evaluation of advanced industrial control projects: a framework for determining economic benefits," *Control Engineering Practice*, 8, pp. 769-780, 2000.

[40] Website: www.steel-technology.com/projects/ipsco, 18.9.2002.

[41] A. Ferreira, Columbus Stainless, Private Communication, 2002.

Appendix A

H_∞ - Controller Design Methodology

A.1 Introduction to the Design Method

The H_∞ controller design method discussed in the following sections of this chapter includes steps that can be summarized as follows [30].

i) Start with a plant model and envisaged specifications for the controlled plant.
ii) Accommodate specifications in weighting functions.
iii) Augment the plant with these weights.
iv) Carry out the H_∞ synthesis on the augmented plant.
v) Measure performance of the design against specifications.
vi) Repeat the procedure from step ii) if design requirements have not been satisfied.

A.2 The H_∞ -Methodology

A.2.1 The Plant Model

The plant model must be FDLTI. The method tolerates non-square , non-minimum phase, and unstable plants given that an augmented plant fulfills certain conditions. It will be discussed later in this chapter what the augmented plant and the conditions are. An upper bound for unstructured uncertainties (generic errors which are associated with all design models[28]) should be known as it serves as a basis for robustness specifications.

A.2.2 Specifications

The control system requirement for nominal stability can be met by H_∞ controllers. Other typical singular value specifications are the following.

i) Robustness specification: 20 dB/decade roll-off and at least –20 dB at e.g. 100 rad/sec, which then ensures a certain bandwidth.

ii) Performance specification: Minimize the sensitivity function as much as possible.

The robustness specification for multivariable systems can also be given more classically as multivariable gain and phase margins. For each loop in a multivariable system these margins exist independently at the same time and can be calculated as,

downward gain margin $$GM \downarrow \leq \frac{k}{k+1},$$

upward gain margin $$GM \uparrow \geq \frac{k}{k-1}, \qquad \text{(A.1)}$$

phase margin $$|PM| \geq 2\sin^{-1}(1/2k)$$

where $$k = \|S(s)\|_\infty$$

and $$S(s) = [I + G(s)K(s)]^{-1}.$$

$S(s)$ is the sensitivity function for the control system in Fig.A.1 with $K(s)$ and $G(s)$ representing the controller and the plant respectively. The robustness specification expressed in terms of gain and phase margins give an indication of the extent to which gain and phase may change in each loop before the system becomes unstable. A small k, i.e. a minimized sensitivity, gives more advantageous gain and phase margins according to Eq.A.1.

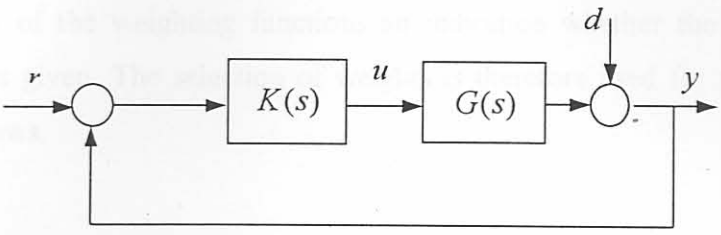

Figure A.1: Standard feedback configuration.

A well known relationship to be considered together with sensitivity is the complementary sensitivity,

$$C(s) = [I + G(s)K(s)]^{-1} G(s)K(s) \quad \text{in}$$
$$S(s) + C(s) = I . \tag{A.2}$$

Eq.A.2 says that either output disturbance or measurement noise rejection is possible in the same frequency range but not both. A small $S(s)$ expresses output disturbance rejection and good tracking whereas a small $T(s)$ means measurement noise rejection.

Regarding performance specifications one can build integrator characteristics into weighting functions in order to achieve zero steady state errors on the controlled output variables. The weighting functions contain parameters that can be tuned until the closed-loop system adheres to specifications. The structure of weights will be discussed in the next section.

A.2.3 The Structure of Weights

Weights are typically connected to the standard feedback configuration as shown in Fig.A.2. Their role is to serve as tuning parameters for the controller $K(s)$. $K(s)$ is designed for the plant $G(s)$ augmented by weights, i.e. for $P(s)$. This means that because $K(s)$ is designed for $P(s)$ instead of only $G(s)$, information about the weights is accommodated in $K(s)$.

The structure of weights $W_i(s) = c_i(s)I_{n\times n}$ $(i = 1,2,3)$ is normally used. The purpose of this diagonal form is to enforce decoupled responses for the closed loop. By computing singular values of the weighting functions an indication whether the closed-loop meets specifications is given. The selection of weights is therefore used for singular value loop shaping as follows.

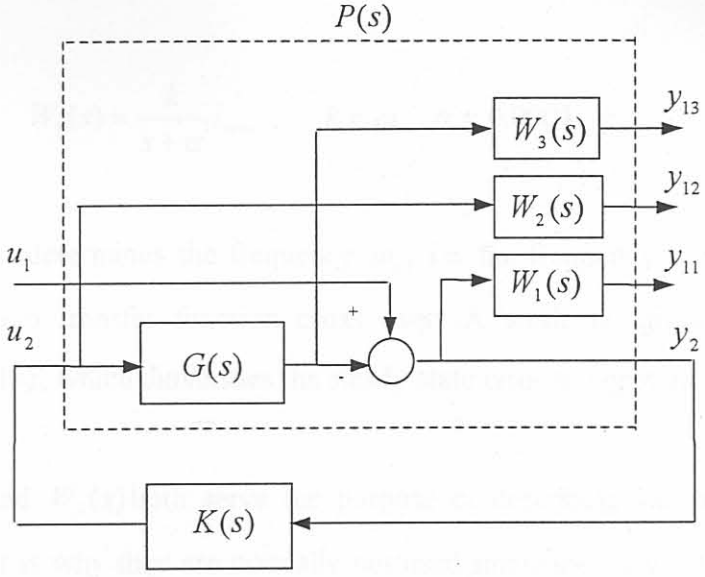

Figure A.2: Standard feedback configuration with weights.

Because $S(s)$ is the closed loop transfer function from disturbance d to output y (see Fig.A.1) singular values of $S(s)$ determine the disturbance attenuation. Therefore the disturbance attenuation performance specification is given as,

$$\lim_{\gamma\to\gamma_{\min}} \bar{\sigma}[S(j\omega)] \approx \bar{\sigma}[W_1^{-1}(j\omega)] \qquad \omega < \omega_c$$

$$\lim_{\gamma\to\gamma_{\min}} \underline{\sigma}[S(j\omega)] \approx \underline{\sigma}[W_1^{-1}(j\omega)] \qquad \omega < \omega_c \tag{A.3}$$

where $\gamma_{\min}$ is the smallest γ still leading to a stabilizing controller for the plant in the γ-iteration. More about the γ-iteration is in section A.2.5 $\bar{\sigma}$ and $\underline{\sigma}$ denote the maximum and minimum singular values respectively.

The specification in Eq.A.3 may be used in the form of a bound as,

$$\bar{\sigma}(S(j\omega) \le \bar{\sigma}(W_1^{-1}(j\omega)) \ , \qquad \omega < \omega_c \tag{A.4}$$

also known as the performance bound with ω_c the crossover frequency. A guideline for a good $W_1(s)$ is to set $\bar{\sigma}(W_1^{-1}(j\omega))$ equal to $\bar{\sigma}(S(j\omega))$ at frequencies below ω_c. A typical structure for $W_1(j\omega)$ [29][30] is,

$$W_1(s) = \frac{k}{s+\alpha} I_{n\times n} \ ; \quad k = \omega_c, \ \alpha = 0.0001 \tag{A.5}$$

The parameter k determines the frequency ω_c, i.e. the frequency at which the singular values of the loop transfer function cross over. A small α gives an approximated integrator for $W_1(s)$, which diminishes the steady state error to constant controller outputs.

Weights $W_2(s)$ and $W_3(s)$ both serve the purpose of describing stability margins of the closed loop. That is why they are normally not used simultaneously. Stability margins are an indication of the robustness of a closed-loop system. A multiplicative stability margin is defined as the size of the smallest stable $\Delta_M(s)$ that can destabilize the system in Fig.A.3 with $\Delta_A(s) = 0$.

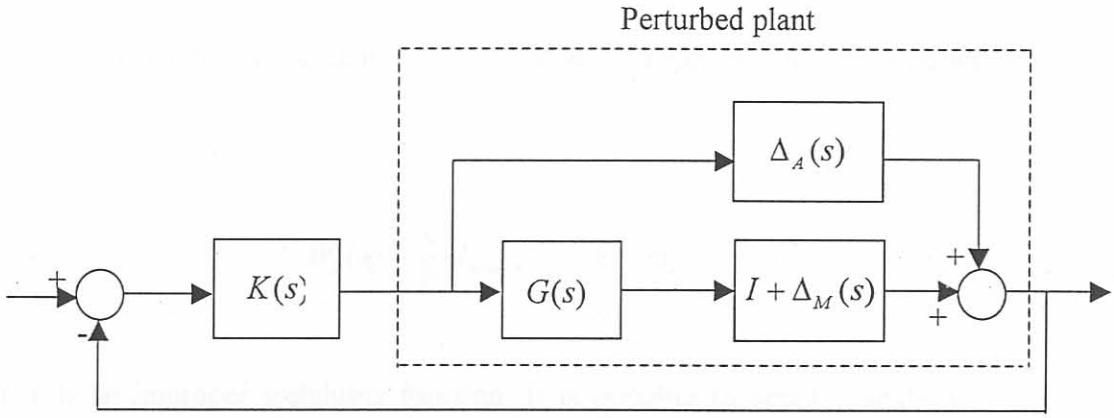

Figure A.3: System uncertainty.

An additive stability margin is defined as the size of the smallest stable $\Delta_A(s)$, which destabilizes the system with $\Delta_M(s) = 0$. These stability margins can be expressed in terms of $C(s)$ and $R(s)$ where $R(s) = K(s)[I + G(s)K(s)]^{-1}$ and because the controller $K(s)$ is

related to the weights the stability margins can be specified via the following singular value inequalities.

$$\begin{aligned} \bar{\sigma}[R(j\omega)] &\le \bar{\sigma}[W_2^{-1}(j\omega)] \qquad \omega > \omega_c \\ \underline{\sigma}[R(j\omega)] &\le \underline{\sigma}[W_2^{-1}(j\omega)] \qquad \omega > \omega_c \end{aligned} \tag{A.6}$$

$$\begin{aligned} \bar{\sigma}[C(j\omega)] &\le \bar{\sigma}[W_3^{-1}(j\omega)] \qquad \omega > \omega_c \\ \underline{\sigma}[C(j\omega)] &\le \underline{\sigma}[W_3^{-1}(j\omega)] \qquad \omega > \omega_c \end{aligned} \tag{A.7}$$

Eq.'s A.6 and A.7 are also known as robustness bounds. It is however common practice to take all plant uncertainty as represented by multiplicative perturbations such that the specifications for controller design become

$$\begin{aligned} \bar{\sigma}[S(j\omega)] &\le \bar{\sigma}[W_1^{-1}(j\omega)] \qquad \omega < \omega_c \\ \bar{\sigma}[C(j\omega)] &\le \bar{\sigma}[W_3^{-1}(j\omega)] \qquad \omega > \omega_c \end{aligned} \tag{A.9}$$

For the weight which is present in the robustness bound, W_3, a typical structure is given by,

$$W_3(s) = \frac{s}{k} \cdot I_{n\times n} \; ; \qquad k = \omega_c \tag{A.10}$$

$W_3(s)$ is an improper weighting function. It is possible to accommodate W_3 within the proper plant, which becomes recognizable in the D and C matrices of the plant augmented by the weights in a state space description. The plant augmentation is described in the next section.

A.2.4 Plant Augmentation

The design of the controller in the H_∞ synthesis problem is based on a plant that is augmented with weights as shown in Fig.A.2. The following is an illustration of the relationships between the signals in Fig.A.2 and of the way in which the weights are incorporated to form the state space description of the augmented plant $P(s)$. For the following descriptions the plant $P(s)$ can be partitioned as a block transfer function matrix,

$$P(s) := \begin{bmatrix} P_{11}(s) & P_{12}(s) \\ P_{21}(s) & P_{22}(s) \end{bmatrix}. \tag{A.11}$$

The signals in Fig.A.2 are related to each other as,

$$\begin{aligned} y_1 &= P_{11}u_1 + P_{12}u_2 \\ y_2 &= P_{21}u_1 + P_{22}u_2 \end{aligned},$$

or

$$\begin{aligned} y_1 = \begin{bmatrix} y_{11} \\ y_{12} \\ y_{13} \end{bmatrix} &= \begin{bmatrix} W_1 \\ 0 \\ 0 \end{bmatrix} u_1 + \begin{bmatrix} -W_1 G \\ W_2 \\ W_3 G \end{bmatrix} u_2 , \\ y_2 &= Iu_1 - Gu_2 , \end{aligned} \tag{A.12}$$

while a detectable and stabilizable state space description of $P(s)$ is,

$$P(s) := \left[\begin{array}{c|cc} A & B_1 & B_2 \\ \hline C_1 & D_{11} & D_{12} \\ C_2 & D_{21} & D_{22} \end{array}\right] \tag{A.13}$$

For the purpose of the synthesis in the next section let the state space form of the plant and weights be described as,

$$G(s)=\begin{bmatrix} A_p & B_p \\ C_p & D_p \end{bmatrix}$$

and

(A.14)

$$W_i=\begin{bmatrix} A_{wi} & B_{wi} \\ C_{wi} & D_{wi} \end{bmatrix}$$

with $i=1,2,3$.

Let the states of the augmented plant $P(s)$ be described by the state vector x_{ap} as,

$$x_{ap}=\begin{bmatrix} x_p & x_{w1} & x_{w2} & x_{w3} \end{bmatrix}^T$$

where the state vectors of the plant $G(s)$ and the weights $W_i(s)$ are represented by x_p and x_{wi} respectively. The matrices of the augmented plant can be written in terms of the state space matrices of the plant and the weights as follows.

$$A=\begin{bmatrix} A_p & 0 & 0 & 0 \\ -B_{w1}C_p & A_{w1} & 0 & 0 \\ 0 & 0 & A_{w2} & 0 \\ B_{w3}C_p & 0 & 0 & A_{w3} \end{bmatrix}$$

$$[B_1 \mid B_2]=\left[\begin{array}{c|c} 0 & B_p \\ B_{w1} & -B_{w1}D_p \\ 0 & B_{w2} \\ 0 & B_{w3}D_p \end{array}\right]$$

(A.15)

$$\begin{bmatrix} C_1 \\ \hline C_2 \end{bmatrix}=\left[\begin{array}{cccc} -D_{w1}C_p & C_{w1} & 0 & 0 \\ 0 & 0 & C_{w2} & 0 \\ D_{w3}C_p & 0 & 0 & C_{w3} \\ \hline -C_p & 0 & 0 & 0 \end{array}\right]$$

$$\left[\begin{array}{c|c} D_{11} & D_{12} \\ \hline D_{21} & D_{22} \end{array}\right]=\left[\begin{array}{c|c} D_{w1} & -D_{w1}D_p \\ 0 & D_{w2} \\ 0 & D_{w3}D_p \\ \hline I & -D_p \end{array}\right]$$

It is possible to write the augmented plant for configurations of plants and weights other than shown in Fig.A.2 in a similar way as shown above because Eq.A.12 is a general description for all plants that can be solved as H_∞ problems.

A.2.5 H_∞ Synthesis and γ-Iteration

Fig.4.6 is the diagram on which the H_∞ feedback problem is based. The control objective is to find a controller $K(s)$ for the FDLTI augmented plant such that the closed loop is nominally stable and the H_∞ norm of the closed loop transfer function from $u_1(t)$ to $y_1(t)$, $H_{y_1u_1}(s)$, is minimized.

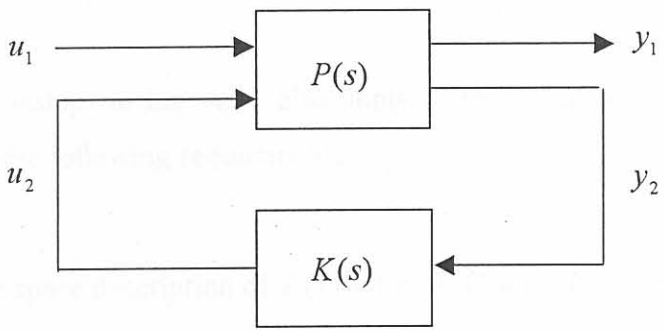

Figure A.4: Synthesis block diagram

In terms of the signals in Fig.A.4 the control problem is to find a controller $K(s)$ which uses the information in the measured output, y_2, to generate a control signal, u_2, which counteracts the influence of the exogenous inputs (weighted), u_1, on the exogenous outputs (weighted), y_1, thereby minimizing the closed loop ∞- norm from u_1 to y_1 [31]. When using weights $W_1(s)$ and $W_3(s)$ to find the H_∞-norm of $H_{y_1u_1}(s)$, the applicable relationship is,

$$\left\| H_{y_1u_1}(j\omega) \right\|_\infty = \max_\omega \bar{\sigma} \begin{bmatrix} W_1(j\omega)S(j\omega) \\ W_3(j\omega)C(j\omega) \end{bmatrix}$$

The controller is designed by way of the γ - iteration. The result of such an iteration would be a sub-optimal controller.

γ - Iteration:

The γ-iteration is a procedure that originates from Doyle et al [32] with the objective to solve the H_∞ output feedback problem. Part of this procedure is solving two modified Riccati equations in order to find a stabilizing controller $K(s)$ such that,

$$\left\| H_{y_1 u_1} \right\|_\infty \leq \gamma \tag{A.16}$$

with

$$\min_{K(s)} \left\| H_{y_1 u_1} \right\|_\infty = \gamma_{optimal}$$

$$\gamma_{optimal} < \gamma$$

The signal relationships in Eq. A.11 also apply to the signals in Fig.A.4. The augmented plant must meet the following requirements:

i) The state space description of $P(s)$ in Eq. A.13 must be stabilizable and detectable.

ii) The transfer functions $P_{11}(s)$ and $P_{22}(s)$ must be strictly proper.

iii) The transfer functions $P_{12}(s)$ and $P_{21}(s)$ must be proper but not strictly proper.

The second condition is satisfied if D_{11} and D_{22} are zero. By adding fast filters to the appropriate weights this condition can be met. Otherwise for D_{11} to be zero weight $W_1(s)$ needs to be strictly proper. D_{22} will also be zero if the plant $G(s)$ is strictly proper.

A standard feedback configuration such as shown in Fig. A.2 guarantees $P_{21}(s)$ to be proper. $P_{12}(s)$ is proper if $G(s)$ and either $W_2(s)$ or $W_3(s)$ or both are used. If the plant is strictly proper ($D_p = 0$), and only one of $W_2(s)$ and $W_3(s)$ is used, the weight, $W_2(s)$, will have to be present. If the use of an improper weight, $W_3(s)$, is preferred to the use of weight, $W_2(s)$, $W_3(s)$ can be used by accommodating it into a strictly proper plant.

Further requirements of the γ-iteration are on D_{12} and D_{21}. D_{12} must have full column rank while D_{21} must have full row rank.

The steps of the γ-iteration are given as follows [30]:

i) Guess γ which indicates the achievable performance.

ii) u_1 and y_1 have to be scaled such that γ in Eq. A.16 is unity, i.e. $\left\|\tilde{H}_{y_1u_1}\right\|_\infty \le 1$, with $\tilde{H}_{y_1u_1}$ being scaled appropriately. Fig. A.5 shows what the scaling in this step entails.

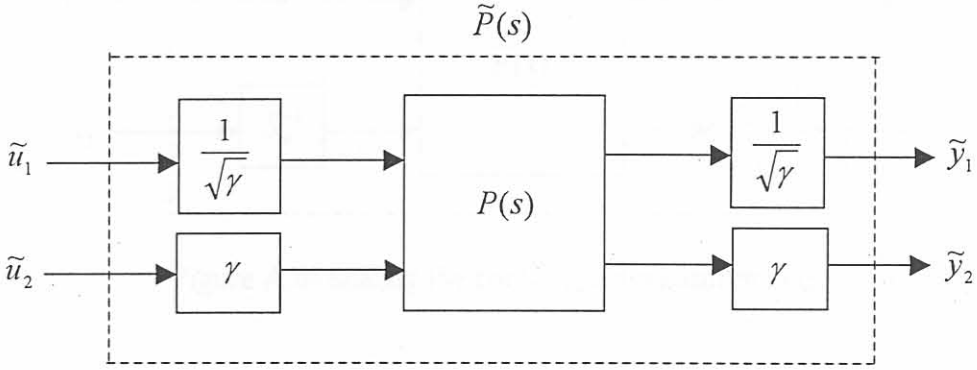

Figure A.5: Scaling the augmented plant.

The signal relationship for the scaled augmented plant $\tilde{P}(s)$ is then as follows:

$$\begin{bmatrix}\tilde{y}_1\\ \tilde{y}_2\end{bmatrix} = \begin{bmatrix}\frac{1}{\sqrt{\gamma}}P_{11}(s) & P_{12}(s)\\ P_{21}(s) & \gamma P_{22}(s)\end{bmatrix}\begin{bmatrix}\tilde{u}_1\\ \tilde{u}_2\end{bmatrix} = \tilde{P}(s)\begin{bmatrix}\tilde{u}_1\\ \tilde{u}_2\end{bmatrix}$$

After scaling, the state space description for $\tilde{P}(s)$ becomes,

$$\tilde{P}(s) = \left[\begin{array}{c|cc} A & \frac{1}{\sqrt{\gamma}}B_1 & \sqrt{\gamma}B_2 \\ \hline \frac{1}{\sqrt{\gamma}}C_1 & \frac{1}{\gamma}D_{11} & D_{12} \\ \sqrt{\gamma}C_2 & D_{21} & \gamma D_{22} \end{array}\right].$$

iii) Scaling of controls u_2 and measurements y_2 is done with matrices S_u and S_y such that,

$$S_u^T S_u = D_{12}^T D_{12} = I$$
$$S_y^{-1}(S_y^{-1})^T = D_{21} D_{21}^T = I \quad ,$$

where S_u and S_y are two square, nonsingular matrices. They can be obtained by a Cholesky decomposition of the identity matrix.

Scaling of u_2 and y_2 is done as shown in Fig. A.6.

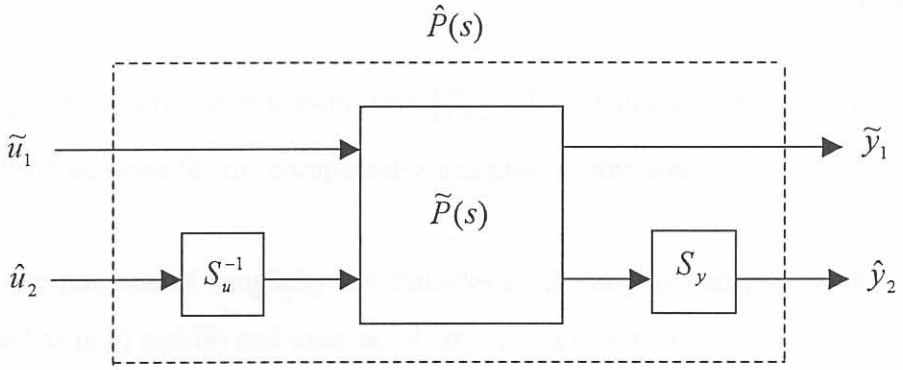

Figure A.6: Scaling the controls and measurements.

S_u and S_y is also used to scale the state space matrices of the plant as follows:

$$\hat{B}_2 = \tilde{B}_2 S_u^{-1}$$
$$\hat{C}_2 = S_y \tilde{C}_2$$
$$\hat{D}_{12} = \tilde{D}_{12} S_u^{-1}$$
$$\hat{D}_{21} = S_y \tilde{D}_{21}$$
$$\hat{D}_{22} = S_y \tilde{D}_{22} S_u^{-1}$$

iv) Fig. A.7 shows the H_∞ controller structure.

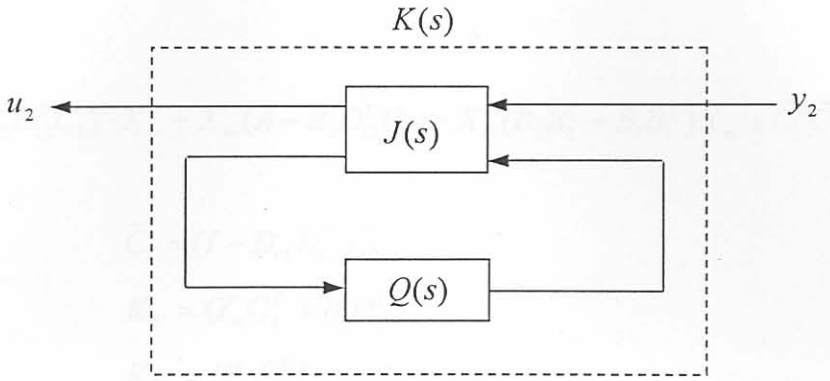

Figure A.7: H_∞ controller structure.

$Q(s)$ can be any stable system with $\|Q\|_\infty \leq 1$. It can also be chosen as, $Q(s) = 0$, as it will be done for the compensator designed in this work.

For the purpose of simplicity the matrices of the augmented plant will be assumed scaled as in ii) and iii) and used as, A, B_j, C_i, D_{ij} with $i, j = 1,2$.

For the controller $K(s)$ in Fig. A.4 the state space description is given as,

$$J(s) = \left[\begin{array}{c|c} A_J & B_J \\ \hline C_J & D_J \end{array}\right]$$

where

$$A_J = A - K_F C_2 - B_2 K_C + Y_\infty C_1^T (C_1 - D_{12} K_C),$$

$$B_J = \begin{bmatrix} K_F & K_{F1} \end{bmatrix},$$

$$C_J = \begin{bmatrix} -K_C \\ K_{C1} \end{bmatrix},$$

$$D_J = \begin{bmatrix} 0 & -I \\ I & 0 \end{bmatrix},$$

$$K_C = (B_2^T X_\infty + D_{12}^T C_1)(I - Y_\infty X_\infty)^{-1},$$

$$K_{C1} = (D_{12} B_1^T - C_2)(I - Y_\infty X_\infty)^{-1},$$

with X_∞ the unique, real, symmetric solution of the Algebraic Riccati equation (ARE),

$$(A - B_2 D_{12}^T C_1)^T X_\infty + X_\infty (A - B_2 D_{12}^T C_1) - X_\infty (B_2 B_2^T - B_1 B_1^T) X_\infty + \widetilde{C}_1^T \widetilde{C}_1 = 0$$

with

$$\widetilde{C}_1 = (I - D_{12} D_{12}^T) C_1 ,$$
$$K_F = (Y_\infty C_2^T + B_1 D_{12}^T),$$
$$K_{F1} = (Y_\infty C_1^T D_{12} + B_2) ,$$

and Y_∞ is the unique, real, symmetric solution of the ARE,

$$(A - B_1 D_{21}^T C_2) Y_\infty + Y_\infty (A - B_1 D_{21}^T C_2)^T - Y_\infty (C_2 C_2^T - C_1 C_1^T) Y_\infty + \widetilde{B}_1^T \widetilde{B}_1 = 0 ,$$

with

$$\widetilde{B}_1 = B_1 (I - D_{21}^T D_{21}) .$$

If the following three conditions hold, then a solution can be obtained and γ in i) does not have to be increased any further.

$$X_\infty \geq 0$$
$$Y_\infty \geq 0$$
$$\overline{\lambda}(Y_\infty X_\infty) \leq 1$$

The iteration has to be repeated from step ii) with an increased γ if the conditions above are not satisfied.

v) u_2 and y_2 on the designed compensator $\hat{K}(s)$ (see Fig. A.8) have to be scaled to,

vi)

$$B_K = \sqrt{\gamma} \hat{B}_K S_y ,$$
$$C_K = \sqrt{\gamma} S_u^{-1} \hat{C}_K ,$$
$$D_K = \gamma S_u^{-1} \hat{D}_K S_y$$

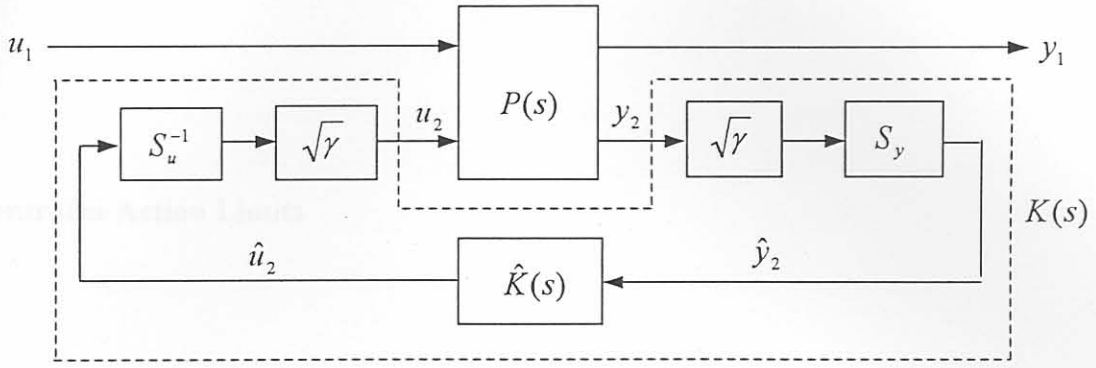

Figure A.8: The designed controller scaled.

The state space matrices of the compensator $\hat{K}(s)$ with $Q(s)=0$ give the state space description as,

$$\hat{K}(s)=\left[\begin{array}{c|c} A-K_F C_2-B_2 K_C+Y_\infty C_1^T (C_1-D_{12}K_C) & K_F \\ \hline K_C & 0 \end{array}\right].$$

Appendix B

Controller Action Limits

B.1 Hydraulic Actuator Limits

Hydraulic actuator stroke, x_s, mill stretch, $y_{stretch}$, and displacement of the upper roll pack, y_1, are in [4] related by

$$x_s = y_{stretch} - y_1 \quad . \tag{B.1}$$

At the maximum rolling force $P_{\max} = 40\,\text{MN}$, the mill stretch limit is

$$y_{stretch\max} = 6.5 \cdot 10^{-3}\,\text{m} \quad [4].$$

The worst case for the mill is that a rolling force is exerted by the hydraulic actuators while the strip in the roll gap does not compress, i.e. $y_1(t,z) = 0$. Then the maximum actuator stroke is determined by the limit to which the mill can stretch:

$$x_{s\max} = y_{stretch\,\max} = 6.5 \cdot 10^{-3}\ \text{m}. \tag{B.2}$$

B.2 Coiler Motor Speed Change Limits

The most severe control action of the coiler motors will be demanded when a fully loaded coiler has to change its speed such that tensions increase from almost zero to their set up values . Therefore this case is considered here in order to determine coiler motor speed change limits.

Based on the graphs in chapter 5 in which the control actions of the back and front coilers can be seen, it is assumed that the back and front coiler speeds change linearly by

$$v_{bc} = a_{bc} t \tag{B.3}$$

$$v_{fc} = a_{fc} t \tag{B.4}$$

such as the peripheral speed of the work rolls which changes as

$$v_{main} = a_{main} \cdot t \approx 0.79 \cdot t \ , \tag{B.5}$$

which is obtained from the speed up ramp of the main drive shown in Fig. 3.2. In the relationships given above the accelerations represent the following.

a_{bc} : peripheral acceleration of back coiler,

a_{fc} : peripheral acceleration of front coiler and

a_{main} : acceleration of mill main drive.

From relationship 2.5 it can be shown that a difference in a_{bc} and a_1, the acceleration of strip material at the roll gap entrance, for T_1 to increase up to its setup value. This difference is denoted by

$$\Delta a_1 = a_1 - a_{bc} \ . \tag{B.6}$$

Equivalently on the mill delivery side the difference between a_{fc} and a_2, the acceleration of strip material at the roll gap exit, for T_2 to increase up to its set up value, is denoted by

$$\Delta a_2 = a_{fc} - a_2 \ . \tag{B.7}$$

a_1 and a_2 can be computed from a_{main} as follows. First it is assumed that the neutral point is at $\phi = \phi_h$ between the roll gap entrance and exit before the tensions are established where

ϕ has the meaning as in Fig. 3.17. ϕ_h indicates the position halfway along the horizontal distance, L_x, between the roll gap entrance and exit. The throughput of material through the roll gap can be expressed as

$$h(\phi_h)v(\phi_h) = h_1 v_1 = h_2 v_2 . \tag{B.8}$$

From this throughput the entrance and exit acceleration of the strip material can then be computed as

$$a_1 = \frac{h(\phi_h)}{h_1} \cdot a_{main} , \tag{B.9}$$

$$a_2 = \frac{h(\phi_h)}{h_2} \cdot a_{main} . \tag{B.10}$$

With ϕ_m being the bite angle it can be determined from

$$\phi_m \approx \cos^{-1}\left(\frac{R - \delta/2}{R}\right) = 5.45° . \tag{B.11}$$

ϕ_h and $h(\phi_h)$ are then computed from

$$\phi_h \approx \sin^{-1}\left(\frac{L_x}{2R}\right) = 2.72° \tag{B.12}$$

where

$$L_x \approx R \sin\phi_m = 36\,\text{mm} \tag{B.13}$$

then

$$h(\phi_h) = h_2 + 2\left(R - R\cos\phi_h\right) = 10.7\ \text{mm} . \tag{B.14}$$

Since the operating point of the controllers will be at $v_{main} = 3.5\,\text{m/s}$ the peripheral speeds of the coilers will be

$$v_{bc} = \frac{h(\phi_h)}{h_1} \cdot v_{main} = 2.8\,\text{m/s} \tag{B.15}$$

and

$$v_{fc} = \frac{h(\phi_h)}{h_2} \cdot v_{main} = 3.78\,\text{m/s} . \tag{B.16}$$

For the radius of a fully loaded coiler, $r_{c\,full} = 1.25\,\text{m}$, and of a coiler mandrel, $r_{c\,mandrel} = 0.675\,\text{m}$, the rotating speeds of the coilers will be $\omega_{bc} = 2.24\,\text{rad/s}$ and $\omega_{fc} = 5.6\,\text{rad/s}$. With a gear box ratio of 1/4.875 these rotating speeds lie in the speed range of 0 to 720 rpm for typical coiler motors [38].

The computation of the torques, $T_{m\,bc}$ and $T_{m\,fc}$, available on the back and front coiler mandrels respectively is based on coiler motor power, $P_c = 1500\,\text{kW}$ [1] and on the coiler rotating speeds:

$$T_{m\,bc} = \frac{P_c}{\omega_{bc}} = 0.67\,\text{MNm} \tag{B.17}$$

$$T_{m\,fc} = \frac{P_c}{\omega_{fc}} = 0.268\,\text{MNm} \ . \tag{B.18}$$

For a step change of $T_{i\,setup}$, $i \in (1,2)$, the possible angular acceleration of a fully loaded coiler, α_{full}, and the coiler mandrel, $\alpha_{mandrel}$, can be determined as

$$\alpha_{full} = T_{m\,bc} / I_{c\,full} \tag{B.19}$$

$$\alpha_{mandrel} = T_{m\,fc} / I_{c\,mandrel} \ , \tag{B.20}$$

where $I_{c\,full} \approx 40310\,\text{kgm}^2$ and $I_{c\,mandrel} \approx 1502\ \text{kgm}^2$ is obtained from dimensions of a typical Steckel mill [38] as the axial moments of inertia of a fully loaded coiler and a coiler mandrel respectively.

The back and front coiler accelerations that are then possible are

$$a_{bc} = \alpha_{full} \cdot r_{c\,full} = 20.8\,\text{m/s}^2 \tag{B.21}$$

$$a_{fc} = \alpha_{mandrel} \cdot r_{c\,mandrel} = 120.4\,\text{m/s}^2 \ . \tag{B.22}$$

The possible acceleration changes Δa_1 and Δa_2 can then be determined from Eq. B.6 and B.7 as $\Delta a_1 = -21\,\text{m/s}^2$ and $\Delta a_2 = 120\,\text{m/s}^2$.

Appendix C

H_∞ Controller State Space Matrices

The continuous state space matrices of the controllers are given in the following. In their state space form the controllers are given by

$$\dot{z}(t) = Fz(t) + Ge(t) \tag{C.1}$$
$$u(t) = Hz(t) + Ne(t) \tag{C.2}$$

where

$e(t)$	: the control error vector,
$z(t)$	: the controller state vector,
$u(t)$	: the controller action vector,
F	: the controller state matrix,
G	: the controller input matrix,
H	: the controller output matrix and
N	: the controller feed-through matrix.

Appendix C

C.1 H_∞ Controller for the Second Linear Model

Matrix F:

Columns 1 through 6

-1.3492e+005	-3.4164e+005	4.4832e+006	1.6519e+006	-2.8014e+006	5.5820e+005
3.8654e-011	-6.5782e+001	-6.1100e-005	8.3823e+001	-1.2418e+003	-3.9187e+003
1.6591e-012	-3.0468e-011	-6.5781e+001	8.5290e+000	8.5183e+001	-3.5105e+002
-7.5346e-012	1.1937e-011	-1.0402e-010	-5.2462e+000	-1.6127e-001	7.2129e-003
2.4570e-011	3.2620e-010	-1.2354e-009	1.0392e-009	-9.9389e-007	1.3478e-008
3.5988e-011	9.2143e-011	-1.3832e-009	-1.1961e-009	8.7299e-010	-1.0015e-006
-3.6507e-013	-1.0703e-012	1.5298e-011	1.6314e-011	-1.1590e-011	1.9835e-011

Column 7

1.4051e+004
1.5770e+002
1.1620e+001
-4.0151e+000
7.0147e-010
-6.3876e-010
-9.9999e-007

Matrix G:

8.2441e+004	-2.0559e+007	-2.2805e+006
-1.4344e+001	-2.0401e+003	-7.8316e+002
-1.4631e+000	-1.4419e+002	-2.2255e+002
-1.0345e+001	1.0493e-003	4.9010e-002
-2.1480e-008	-1.9791e-007	1.0175e-006
-9.5162e-008	-4.5064e-007	-5.2139e-007
-2.4050e-006	1.9722e-008	6.7007e-00

Matrix H:

Columns 1 through 6

$$\begin{bmatrix} 1.6305e\text{-}003 & 4.2899e\text{-}003 & -5.7355e\text{-}002 & 4.1393e{+}000 & 7.6829e{+}003 & 1.0539e{+}004 \\ 4.9458e\text{-}005 & -3.5084e\text{-}001 & 1.2342e{+}000 & 3.0441e\text{-}001 & 5.5834e{+}008 & 1.0870e{+}009 \\ 4.7142e\text{-}006 & -9.4548e\text{-}002 & 1.3482e{+}000 & 2.0210e\text{-}002 & 1.9912e{+}008 & -9.1235e{+}007 \end{bmatrix}$$

Column 7

$$\begin{bmatrix} 3.2787e{+}005 \\ -4.7954e{+}007 \\ 1.4909e{+}006 \end{bmatrix}$$

Matrix N:

$$\begin{bmatrix} 0 & 0 & 0 \\ 0 & 0 & 0 \\ 0 & 0 & 0 \end{bmatrix}$$

C.2 H_∞ Controller for the Third Linear Model

Matrix F:

Columns 1 through 6

-7.5938e+001	8.5808e+001	4.6065e+003	1.0655e+004	5.1611e+003	1.1942e+004
4.0000e+000	0	0	0	0	0
5.1963e-001	1.0964e+001	2.3278e+002	1.3073e+003	6.4514e+002	1.4927e+003
0	0	1.6000e+001	0	0	0
5.1963e-001	1.0964e+001	5.7581e+002	1.3319e+003	3.0208e+002	1.4676e+003
0	0	0	0	1.6000e+001	0
-4.4761e-004	-9.4442e-003	-5.0560e-001	-1.1715e+000	-1.2745e-002	-2.9498e-002
-5.7295e-002	-1.2089e+000	-6.4716e+001	-1.4995e+002	-1.6313e+000	-3.7757e+000
0	0	0	0	0	0
-5.5952e-005	-1.1805e-003	-6.3200e-002	-1.4643e-001	-1.5931e-003	-3.6872e-003
1.3918e-003	2.9365e-002	-2.9568e-002	-6.8236e-002	1.6413e+000	3.8040e+000
0	0	0	0	0	0
1.7398e-004	3.6706e-003	-3.6960e-003	-8.5296e-003	2.0517e-001	4.7550e-001
0	0	0	0	0	0
2.2269e-002	4.6984e-001	-4.7309e-001	-1.0918e+000	2.6261e+001	6.0864e+001
0	0	0	0	0	0
0	0	0	0	0	0
0	0	0	0	0	0
0	0	0	0	0	0

Columns 7 through 12

-4.6036e+000	1.3753e+007	4.4164e+005	-5.6263e+002	-5.9274e+001	4.6276e+001
0	0	0	0	0	0
-5.7545e-001	1.7191e+006	5.5206e+004	-7.0329e+001	-7.4092e+000	5.7845e+000
0	0	0	0	0	0
-5.7545e-001	1.7191e+006	5.5206e+004	-7.0329e+001	-7.4092e+000	5.7845e+000
0	0	0	0	0	0
-9.5043e-003	-1.4413e+003	-2.9218e+001	1.3898e-003	6.3830e-003	-4.9829e-003
6.3450e-002	-1.9359e+005	-6.2160e+003	1.7789e-001	8.1702e-001	-6.3781e-001
0	2.0480e+003	0	0	0	0
6.1963e-005	-1.8017e+002	-3.6522e+000	-9.8263e-003	7.9787e-004	-6.2286e-004
-1.5413e-003	-8.8333e+001	-2.8422e+000	-1.7923e-001	-5.6025e+002	-1.3851e+000
0	0	0	0	4.0000e+000	0
-1.9266e-004	-1.1042e+001	-3.5527e-001	-2.2404e-002	-2.4809e-003	1.9367e-003
0	0	0	0	0	0
-2.4661e-002	-1.4133e+003	-4.5474e+001	-2.8677e+000	-3.1755e-001	2.4789e-001
0	0	0	0	0	0
0	0	0	0	0	0
0	0	0	0	0	0
0	0	0	0	0	0

Columns 13 through 18

6.1582e+002	1.0788e+004	-3.9644e+007	-1.2732e+006	1.7142e+004	1.7494e+006
0	0	0	0	0	0
7.6978e+001	1.3485e+003	-4.9555e+006	-1.5914e+005	2.1427e+003	2.1868e+005
0	0	0	0	0	0
7.6978e+001	1.3485e+003	-4.9555e+006	-1.5914e+005	2.1427e+003	2.1868e+005
0	0	0	0	0	0
-6.7515e-002	-1.1862e+000	9.7890e+001	3.1429e+000	-1.8458e+000	-1.9232e+002
-8.6420e+000	-1.5183e+002	1.2530e+004	4.0229e+002	-2.3626e+002	-2.4617e+004
0	0	0	0	0	0
-8.4394e-003	-1.4827e-001	1.2236e+001	3.9286e-001	-2.3072e-001	-2.4040e+001
-3.9537e-003	-6.9081e-002	-1.2120e+004	-2.3740e+002	5.7392e+000	-1.1212e+001
0	0	0	0	0	0
-5.6023e+002	-2.8098e+000	-1.5150e+003	-2.9675e+001	7.1740e-001	-1.4015e+000
2.0000e+000	0	0	0	0	0
-6.3260e-002	-1.1053e+000	-2.0210e+005	-6.4892e+003	9.1827e+001	-1.7940e+002
0	0	2.0480e+003	0	0	0
0	0	0	0	-1.0000e-006	0
0	0	0	0	0	-1.0000e-006
0	0	0	0	0	0

Column 19

$$\begin{pmatrix} 1.8910e+006 \\ 0 \\ 2.3638e+005 \\ 0 \\ 2.3638e+005 \\ 0 \\ -4.6706e+000 \\ -5.9783e+002 \\ 0 \\ -5.8382e-001 \\ 6.0231e+002 \\ 0 \\ 7.5288e+001 \\ 0 \\ 9.6369e+003 \\ 0 \\ 0 \\ 0 \\ -1.0000e-006 \end{pmatrix}$$

Matrix G:

0	0	0
0	0	0
0	0	0
0	0	0
0	0	0
0	0	0
0	0	0
0	0	0
0	0	0
0	0	0
0	0	0
0	0	0
0	0	0
0	0	0
0	0	0
3.9063e-003	0	0
0	1.0000e+000	0
0	0	1.0000e+000

Matrix H:

Columns 1 through 6

2.0785e+000	4.3854e+001	2.3032e+003	5.3275e+003	2.5805e+003	5.9709e+003
-3.5809e-003	-7.5553e-002	-4.0448e+000	-9.3718e+000	-1.0196e-001	-2.3598e-001
1.3918e-003	2.9365e-002	-2.9568e-002	-6.8236e-002	1.6413e+000	3.8040e+000

Columns 7 through 12

-2.3018e+000	6.8763e+006	2.2082e+005	-2.8131e+002	-2.9637e+001	2.3138e+001
3.9656e-003	-1.1531e+004	-2.3374e+002	1.1118e-002	5.1064e-002	-3.9863e-002
-1.5413e-003	-8.8333e+001	-2.8422e+000	-1.7923e-001	-1.9847e-002	1.5493e-002

Columns 13 through 18

3.0791e+002	5.3940e+003	-1.9822e+007	-6.3658e+005	8.5710e+003	8.7470e+005
-5.4012e-001	-9.4893e+000	7.8312e+002	2.5143e+001	-1.4766e+001	-1.5386e+003
-3.9537e-003	-6.9081e-002	-1.2120e+004	-2.3740e+002	5.7392e+000	-1.1212e+001

Column 19

9.4551e+005
-3.7364e+001
6.0231e+002

Matrix N:

$$\begin{bmatrix} 0 & 0 & 0 \\ 0 & 0 & 0 \\ 0 & 0 & 0 \end{bmatrix}$$

Appendix D

Signals for Controller Design and Implementation

The controllers as discussed in chapter 5 were designed for models with deviational inputs and outputs such that the signals at the inputs and outputs of both the controller and plant in Fig. D.1 had the values as in Tab. D.1.

For controller implementation on the nonlinear plant simulator the signals in Fig. D.1 had the values as in Tab. D.2.

Fig. D.1 and Tab.'s D.1 and D.2 show that the inputs and outputs of controller and plant in the design stage are deviational variables, i.e.

$$e_i = \Delta e_i = \Delta r_i - \Delta y_i \tag{D.1}$$

$$u_i = \Delta u_i \tag{D.2}$$

$$y_i = \Delta y_i \tag{D.3}$$

and during the implementation stage the plant demand and output become respectively,

$$u_i = \Delta u_i + u_{ir} \tag{D.4}$$

and

$$y_i = \Delta y_i + y_{iss}(t) \ . \tag{D.5}$$

Since the controller was designed for deviational variables as input to compute a deviational variable as controller output, it's input has to be a deviational variable during implementation, i.e.

Table D.1: Signal values for controller design

Signal	Value
u_1	Δu_1
u_2	Δu_2
u_3	Δu_3
u_{1r}	0
u_{2r}	0
u_{3r}	0
y_{11}	Δy_{11}
y_{12}	Δy_{12}
y_{13}	Δy_{13}
y_{21}	Δy_{21}
y_{22}	Δy_{22}
y_{23}	Δy_{23}
y_{31}	Δy_{31}
y_{32}	Δy_{32}
y_{33}	Δy_{33}
y_1	Δy_1
y_2	Δy_2
y_3	Δy_3
r_1	Δr_1
r_2	Δr_2
r_3	Δr_3

$$\Delta e_i = \Delta r_i - \Delta y_i = \left(\Delta r_i + y_{iss}(t)\right) - \left(\Delta y_i + y_{iss}(t)\right) = r_i - y_i \tag{D.6}$$

Therefore the reference, r_i, has to be,

$$r_i = \Delta r_i + y_{iss}(t) \ , \tag{D.7}$$

Table D.2: Signal values for controller implementation

Signal	Value
u_1	$\Delta u_1 + u_{1ss}$
u_2	$\Delta u_2 + 0$
u_3	$\Delta u_3 + 0$
u_{1r}	u_{1ss}
u_{2r}	0
u_{3r}	0
y_{11}	-
y_{12}	-
y_{13}	-
y_{21}	-
y_{22}	-
y_{23}	-
y_{31}	-
y_{32}	-
y_{33}	-
y_1	$\Delta y_1 + y_{1ss}(t)$
y_2	$\Delta y_2 + y_{2ss}(t)$
y_3	$\Delta y_3 + y_{3ss}(t)$
r_1	$\Delta r_1 + y_{1ss}(t)$
r_2	$\Delta r_2 + y_{2ss}(t)$
r_3	$\Delta r_3 + y_{3ss}(t)$

i.e. a steady state value, y_{iss}, has to be added to the deviational reference Δr_i. Because of the steady state evolution for all three of the nonlinear plant simulator outputs this steady state value is time dependent for all three outputs y_i.

Appendix D

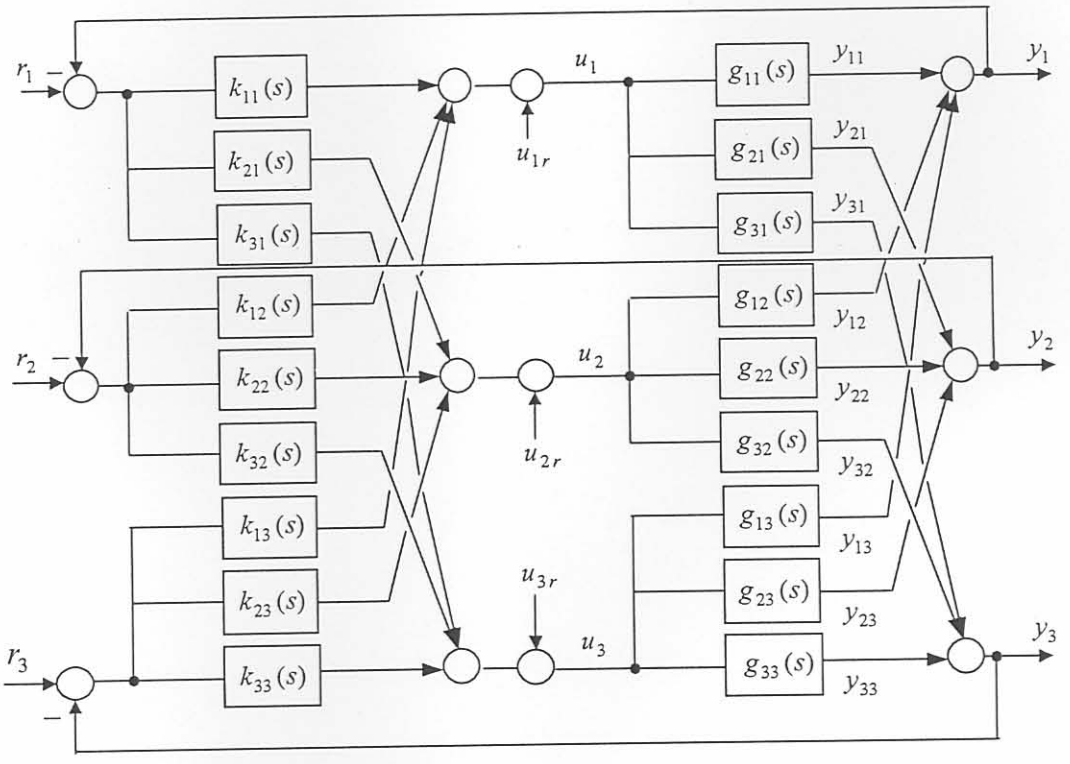

Figure D.1: Blockdiagram of MIMO control system (signs of signals at summation points are positive except where indicated else).